12-1-2018

Kinetics of Higher Lying Potassium States after Excitation of the D2 Transition in the Presence of Helium

Austin J. Wallerstein

Follow this and additional works at: https://scholar.afit.edu/etd

Part of the Plasma and Beam Physics Commons

KINETICS OF HIGHER LYING POTASSIUM STATES AFTER EXCITATION OF THE D_2 TRANSITION IN THE PRESENCE OF HELIUM

DISSERTATION

Austin Jonathan Wallerstein, Captain, USAF

AFIT-ENP-DS-18-D-009

DEPARTMENT OF THE AIR FORCE
AIR UNIVERSITY

AIR FORCE INSTITUTE OF TECHNOLOGY

Wright-Patterson Air Force Base, Ohio

The views expressed in this document are those of the author and do not reflect the official policy or position of the United States Air Force, the United States Department of Defense or the United States Government. This material is declared a work of the U.S. Government and is not subject to copyright protection in the United States.

AFIT-ENP-DS-18-D-009

KINETICS OF HIGHER LYING POTASSIUM STATES AFTER

EXCITATION OF THE D_2 TRANSITION

IN THE PRESENCE OF HELIUM

DISSERTATION

Presented to the Faculty

Graduate School of Engineering and Management

Air Force Institute of Technology

Air University

Air Education and Training Command

in Partial Fulfillment of the Requirements for the

Degree of Doctorate of Philosophy in Applied Physics

Austin Jonathan Wallerstein, B.S., M.S

Captain, USAF

December 2018

KINETICS OF HIGHER LYING POTASSIUM STATES AFTER

EXCITATION OF THE D_2 TRANSITION

IN THE PRESENCE OF HELIUM

DISSERTATION

Austin Jonathan Wallerstein, B.S., M.S
Captain, USAF

Committee Membership:

Glen Perram, PhD
Chair

William W. Baker, PhD
Member

Major Charlton D. Lewis, PhD
Member

Christopher A. Rice, PhD
Member

Abstract

A kinetic model for the performance of a potassium Diode Pumped Alkali Laser (DPAL), including the role of higher lying states is developed to assess the impact on device efficiency and performance. A rate package for a nine level kinetic model including recommended rate parameters is solved under steady-state conditions. Energy pooling and far wing absorption populates higher lying states, with single photon and Penning ionization leading to modest potassium (K) dimer ion concentrations. The fraction of the population removed from the basic three levels associated with the standard model is less than 10% for all reasonable laser conditions, including pump intensities up to $100\ kW/cm^2$ and K densities as high as $10^{16}\ cm^{-3}$. To benchmark this new model, fluorescence emitted by a high power, transverse flow potassium DPAL was collected to characterize the highly excited state population at total alkali densities of $N = 0.15 - 1.87 \times 10^{14}\ cm^{-3}$, buffer gas pressures of $P = 250 - 1200$ Torr, and pump intensities of $I_p = 20 - 60\ kW/cm^2$, with and without methane. The population in these states was found to be less than 5% for all cases. The effects of these higher energy levels are demonstrated on a potasssium-helium system with pump intensities larger than $I_p > 5\ kW/cm^2$ with moderate number densities $N = 0.1 - 10 \times 10^{13}\ cm^{-3}$. The additional heat loading due to the quenching of the higher states is minimal, $< 1\%$ of the spin-orbit mixing heat load. This extra heat has a small effect on both Strehl and efficiency in the static system, but these can be recovered with flow velocities commensurate with transit times across the pump volume $< 0.1\ s$.

Acknowledgements

I would like to express total gratitude to my academic advisor Dr. Glen Perram, for everything he has done for me during this very trying time. He has spent countless hours with me in his office allowing me to figure out this process. Without his experience and knowledge I would have nothing to show for all of my effort.

Next, I would like to thank Dr. Christopher Rice. He has been there for me every step of the way, both in and out of the lab. Many times I would insist I did not need his help, only to find halfway that his assistance was essential to complete the task.

The group of researchers out at Kirtland AFB–Dr. Greg Pitz, Eric Guild, and Don Stahlnaker–also deserve a thank you. Their mentoring, support, and access to their world class facilities was terrific. They spent their time with me helping me get the best data I could, and I would have nothing to show without you guys.

Lastly, I probably should thank my wonderful wife for the support and distraction she has given me the last few years. If I didn't have you, maybe I would have been done a bit earlier, but would not be nearly as happy.

Austin Jonathan Wallerstein

Table of Contents

List of Figures

x

xi

List of Tables

KINETICS OF HIGHER LYING POTASSIUM STATES AFTER EXCITATION OF THE D_2 TRANSITION IN THE PRESENCE OF HELIUM

I. Introduction and Background

1.1 Alkali Lasers

The first Diode Pumped Alkali Laser (DPAL) was demonstrated in 2003 by Krupke et. al using rubidium as the gain media (1), pumping along the D_2 line and lasing on the D_1. Other demonstrations of this laser system quickly followed in different alkali vapors and different pump sources. The alkali metals are of great interest to the laser community, due to the small quantum defect between the pump and laser levels, shown in Table 1, and their large optical cross sections. Additionally, high powered and efficient laser diode arrays were already commercially available for the D_2 transitions in cesium (Cs), rubidium (Rb), and potassium (K)(2).

Table 1. Alkali D_2, D_1 lines, and associated splitting (3)

Alkali	D_2 Line (nm)	D_1 Line (nm)	ΔE (cm^{-1})	Quantum Efficiency, η_{qe}
Li	670.96	670.98	0.444	0.9998
Na	589.16	589.76	17.2	0.9990
K	766.70	770.11	57.7	0.9956
Rb	780.23	794.98	237	0.9814
Cs	852.35	894.59	554	0.9531

1

The alkali is pumped from the ground $^2S_{\frac{1}{2}}$ state to the the $^2P_{\frac{3}{2}}$, along the D_2 line. In the presence of a buffer gas, the alkali is then collisionally relaxed via spin-orbit mixing to the $^2P_{\frac{1}{2}}$ state. When an inversion is realized, lasing then occurs along the $^2P_{\frac{1}{2}} \rightarrow {}^2S_{\frac{1}{2}}$, or D_1 transition. This process is shown in Figure 1 for rubidium.
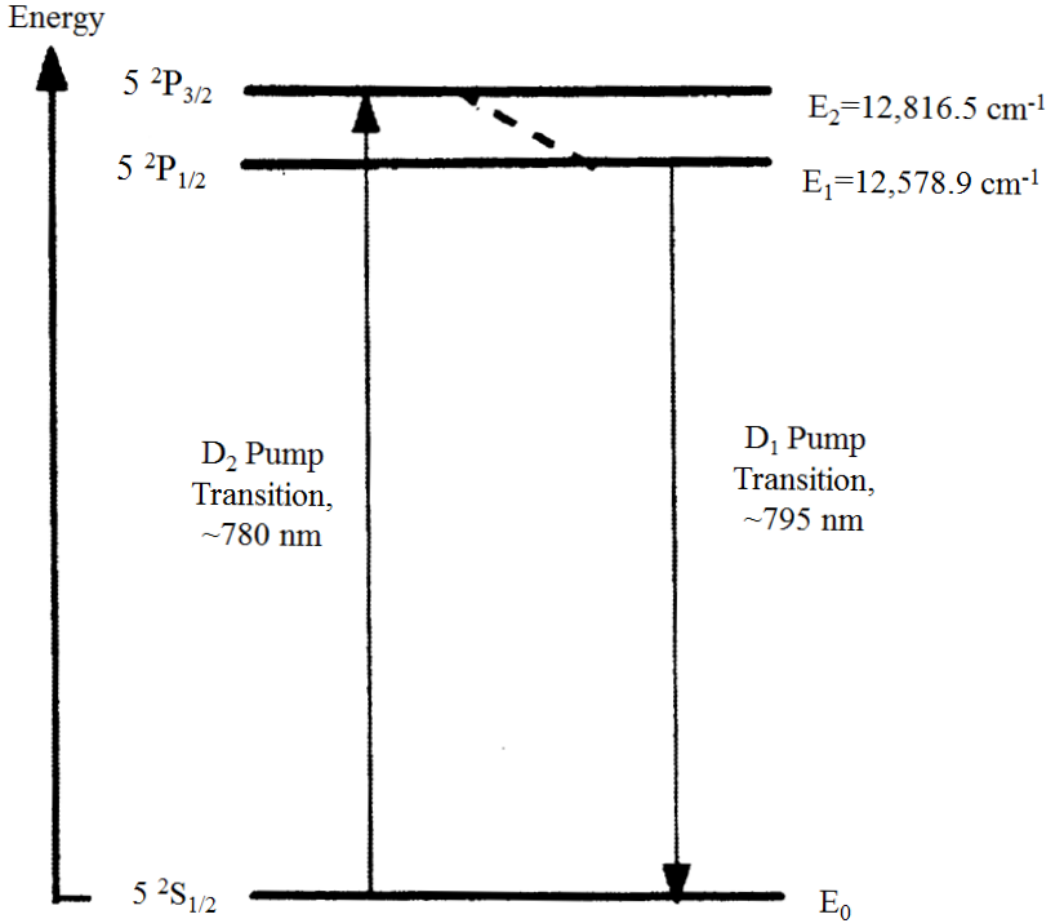
Figure 1. Energy Levels associated with a rubidium DPAL

High pressure buffer gas in needed to efficiently mix the two spin-orbit split excited states. The spin orbit mixing rate needs to be significantly faster than the radiative rate, $3.8 \times 10^7\ s^{-1}$ for $^2P_{\frac{3}{2}}$ in potassium, for optimal laser performance. If the spin orbit mixing is slower than the stimulated rates, bottlenecking occurs and laser performance is degraded.

2

In addition to aiding in spin-orbit mixing, the buffer gas is needed to pressure broaden the absorption profile of the D_2 transition to better match the wide line width of diode pump sources. The current technology is only able to narrow the line shape of diode bar emission to a FWHM of ~ 10 GHz, while typical broadening rates of the D_2 transition are around 19 MHz/Torr (4). Over an atmosphere of buffer gas is required to efficiently overlap the two line shapes, even with diode narrowing to 10 GHz.

Because of the thermal management advantages of alkali vapor, the DPAL has been identified as a possible weapon system for the Air Force. Scaling to weapons grade power would enable air-to-air engagement for strategic military operations. The first 1 kW/cm^2 alkali laser device was demonstrated in 2012 (5) and the current CW scaling limit is 30 kW/cm^2 (6).

The role of multi level kinetics is unclear and in one attempt at CW power scaling in 2008, an apparent roll off of output intensity occurred as pump power increased, shown in Figure 2 (7). A controversy has sprouted as many explanations have been offered to resolve this decrease in laser power. Thermal effects generated through the spin-orbit mixing of the alkali elevate the temperature in the pump laser and drive alkali out of the gain path and drive down power. There is evidence that alkali heating is occurring (8), but it may not be severe enough to cause this trend of decreased ouput power. At the same time, excess pump energy is exciting alkali out of the lasing process and producing higher lying atomic states and both atomic and dimer ions. As mentioned above, it has been since demonstrated that CW output powers above 60 W are possible. Additionally, pulsed experiments have linear increase with pump power up to 7 MW/cm^2 (9). Multi-level kinetics still remains a point of discussion in the DPAL community.

Multiple attempts at modeling the higher lying levels have been accomplished.
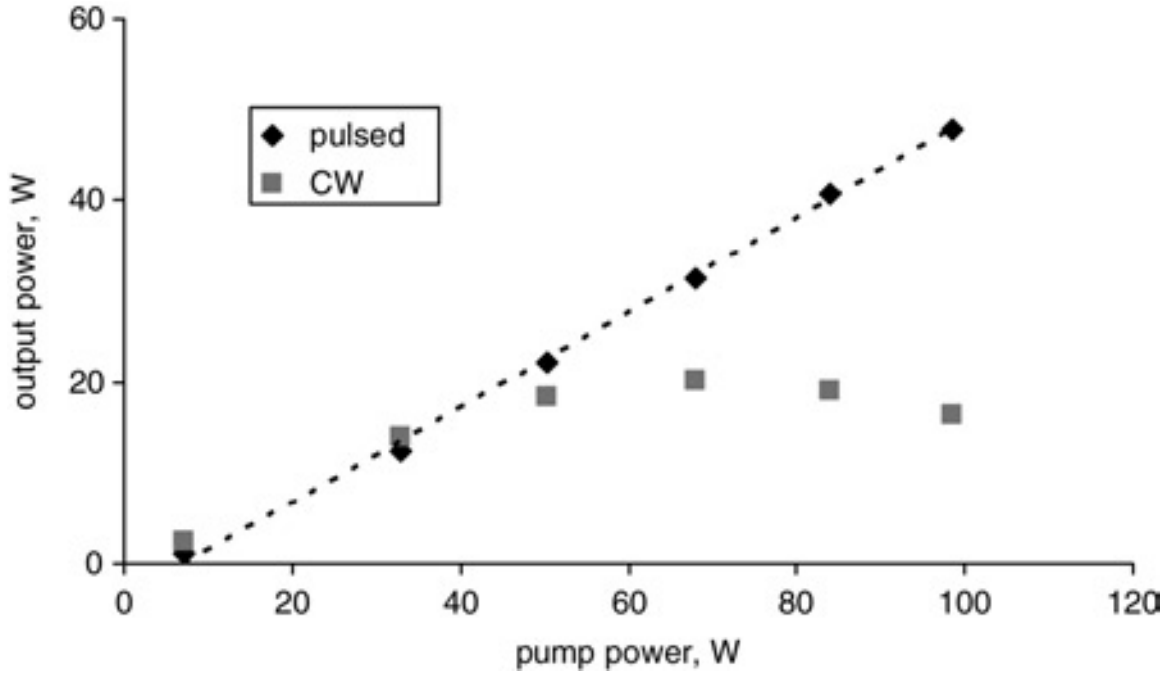
Figure 2. Output laser power is shown as a function of pump power in both a CW ($\square$) and pulsed ($\diamond$) experiment (7).

One such effort claims the ionization rate may be catastrophically high, however the model is enacted without all restorative processes, such as recombination (10). A static model for a cesium DPAL that incorporates kinetic and fluid dynamics was also developed, but the findings were inconclusive (11). A kinetic mechanism and fluid dynamics model to investigate static and flowing cesium DPAL was created that focused on the role of hydrocarbons in the lasing process (12). Direct measurements of the ionization in a DPAL using optogalvanic techniques indicate that at low power and low pressures, the degree of ionization is low $< 10^{-5}$ of the total alkali density, but it increases with pressure and pump power. The degree of ionization may become problematic as the laser scales to higher powers (13).

This research effort is focused on the creation of a mechanism to describe the adverse effects of multi-level kinetics on high powered DPAL devices. This includes characterization of the population in higher excited states as a function of alkali density, buffer gas pressure, and laser pump intensity. A kinetic model is developed

4

and benchmarked with observations of fluorescence from the higher lying states in a high power, transverse flow, potassium DPAL. The effects of extra heat loading on beam quality and efficiency due to these highly excited states is also examined.

1.2   Nine level kinetic model

The first portion of this work focuses on the formulation of the nine level kinetics model, including a thorough literature review of the excitation and de-excitation mechanisms in alkali vapors. This model expands on the well documented three level model presented by Hager et. al (14; 15). Theoretical laser efficiency of the three level model is compared with that of the nine level expansion. These calculations in rubidium were presented at SPIE Photonics West in 2018, and are further developed for potassium in Chapter II.

1.3   Fluorescence in a flowing DPAL

The new model is benchmarked with fluorescence measurements from a high powered, flowing, potassium DPAL at Air Force Research Labratory, Directed Energy Directorate, Kirtland Air Force Base. Fluorescence from over 35 atomic lines in potassium were observed at pump intensities over $20\, kW/cm^2$. This technique was used only once previously in the literature, and no attempt was taken to characterize the spectral output with alkali density, helium pressure, or pump intensity (16). This effort attempts to demonstrate the relative importance of energy pooling and wing absorption to the production of intermediate states and will comment on the effect that multi-level kinetics has on a flowing DPAL system. Data was collected in two different collections, and the observations are reconciled with the model in Chapters III and IV. An updated set of kinetic rates are suggested to accurately predict the data.

1.4 Heat loading due to higher level quenching

Lastly, this work aims to describe the degradation to beam quality due to heat loading added by the higher lying states. Recently developed code used to describe the temperature profile of a transverse flowing DPAL is updated to include the nine level kinetics conceived here. Beam quality aberrations due to the additional heating are also indicated. The restorative effects of flow velocity are shown, and optimal beam quality is also described. These results are described in Chapter V.

II. Excitation of higher lying states in a potassium Diode Pumped Alkali Laser

A kinetic model for the performance of a potassium DPAL, including the role of higher lying states is developed to assess the impact on device efficiency and performance. A rate package for a nine-level kinetic model including recommended rate parameters is solved under steady-state conditions. Energy pooling and far wing absorption populates higher lying states, with single photon and Penning ionization leading to modest potassium dimer ion concentrations. The fraction of the population removed from the basic three levels associated with the standard model is less than 10% for all reasonable laser conditions, including pump intensities up to $100\,kW/cm^2$ and K densities as high as $10^{16}\,cm^{-3}$. The influence of these effects can largely be mitigated by proper control of the inlet alkali density.

2.1 Introduction

The Diode Pumped Alkali Laser (DPAL) is a quasi-two level laser system using the lowest three energy states of the alkali vapor (14). The gas is optically pumped at the D_2 transition, $n^2S_{\frac{1}{2}} \to n^2P_{\frac{3}{2}}$, then, in the presence of the buffer gas, is collisionally relaxed to the fine structure split $n^2P_{\frac{1}{2}}$ state. When the population is inverted, the atom lases from there to the ground state in the near infrared (2). The DPAL is a relatively new gas laser system for high power applications (2; 17). The DPAL system has been scaled to $> 1\,kW$, with optical efficiency $> 80\%$, and promises excellent beam quality (18). Ideal, quasi-two level performance is achieved when the cycle rate is limited only by diode pump intensity. A pulsed potassium laser has been demonstrated with the time scale for fine structure mixing of 70 ps (9).

There are mechanisms that may populate higher lying levels, particularly for highly scaled systems. If a significant alkali density is removed from the lower three

7

levels, pump absorbance will be reduced, decreasing power efficiency. This effect may be largely mitigated by proper control of inlet or initial alkali density. Spatial variations in alkali density could lead to higher order uncorrectable effects. Furthermore, heat released from collisional deactivation of these higher lying states could adversely effect beam quality. There has been some controversy regarding the role of ionization in degrading efficiency at high pump intensity (10; 19; 20). Experiments have shown that above 70 W of CW pump power, the output power falls off, dropping from 20 W with 70 W pump to 15 W at 100 W pump intensity (7). Several theories have been posited to explain this phenomenon, including heating, alkali diffusion, and ionization.

Several previous models to describe ionization in DPALs have been developed (10; 11; 12). For example a kinetic mechanism and fluid dynamics model to investigate static and flowing cesium DPAL, focused on the role of hydrocarbons in the lasing process (12). Oliker et. al also produced a static model for a cesium DPAL that incorporates kinetic and fluid dynamics (11). This three dimensional model included a look at thermal aberrations but neglects dissociative recombination. Knize suggests ionization rates may be catastrophically high in all alkalies but does not fully evaluate restorative processes like recombination (10). Full plasma models have also been produced. An analysis of a cesium DPAL suggested that laser power will experience major degradation, but less when a stronger quencher, nitrogen, is added as the buffer gas, as plasma formation is decreased (19). A second plasma model for a cesium excimer pumped alkali laser (XPAL) concluded that with appropriate seed electrons the degree of ionization would be 28.5% (21). This model accounted for 53 species of cesium, argon, and nitrogen in the cell. Despite these analyses, high power devices have been developed with excellent efficiency (18; 19)

Processes that collisionally deactivate the higher lying levels may contribute to

8

the total heat load and degrade device beam quality. The quantum defect in the potassium DPAL is particularly small (0.005), and the heat load for the ideal three level system is modest. Quenching of the diode pumped and upper laser levels by rare gases is sufficiency low to be difficult to measure. The larger energies associated with states near ionization might lead to substantially more heating, if the population of high lying states is significant.

In this paper, a nine level model is developed to describe the degree of ionization in a scaled potassium DPAL. The primary kinetic processes and their associated rate coefficients are reviewed and developed. Analytic steady-state solutions for the state populations are developed and used to assess the impact on laser efficiency. This work extends the prior analytic three level model (14; 15) and forms the basis for analyzing new high power, flowing potassium DPAL experiments.

2.2 Kinetic processes and rates

2.2.1 Energy Levels.

The energy level diagram for atomic potassium is provided in Figure 3 and a summary of the key energy levels is provided in Table 2 (3). The basic DPAL operates by diode pumping on the D_2 transition, $4\,^2S_{\frac{1}{2}} - 4\,^2P_{\frac{3}{2}}$, collision induced transfer to the fine structure split $4\,^2P_{\frac{1}{2}}$, followed by lasing back to the ground state. The fine structure splitting in K is modest, $57.71\ cm^{-1}$, so that a statistical distribution at a temperature of 400 K yields a ratio for the population of the pumped and upper laser level of $\frac{n_3}{n_2} = \frac{g_3}{g_2}exp(-(E_3-E_2)/kT) = 1.624$. The ionizational potential for potassium is 4.359 eV (35009.814 cm^{-1}), or 2.68 times the energy of the diode pumped, $4\,^2P_{\frac{3}{2}}$ state, requiring 3 photons to ionize. The intermediate $6\,^2S_{\frac{1}{2}}$, $5\,^2P_{\frac{3}{2},\frac{1}{2}}$, and $4\,^2D_{\frac{5}{2},\frac{3}{2}}$ states lie near the energy associated with two pump photons, shown as a solid line in Figure 3. The dashed line in Figure 3 illustrates the lowest energy accessible

9

to ionization via a single pump photon indicating that the $5\,^2S_{\frac{1}{2}}$ and $3\,^2D_{\frac{5}{2},\frac{3}{2}}$ are not involved in single step photo-ionization, and are thus excluded from our designation as intermediate states. Levels lying above the intermediate states we group and designate the Rydberg states. We intend to track both atomic and dimer ions. The dissociation energy of $K_2^+(X) = 0.76\,eV = 6130\,cm^{-1}$ (22). The DPAL alkali density is sufficiently low, $\sim 10^{14}$ atoms/cm^3 with melt pool temperatures of < 450 K, where the neutral dimer concentration in the absence of optical excitation is low $< 1.5\%$ (23). We neglect states with an orbital angular momentum quantum number $L > 2\,(^2F,^2G)$. We note that the fine structure splitting of the higher lying states is small, $< 19\,cm^{-1}$, and assume a statistical distribution between the J states, except for the pump and laser $4\,^2P_{\frac{3}{2},\frac{1}{2}}$ states. The kinetic model will be reduced to predicting the population in nine levels of Table 2.

Table 2. Relevant potassium energy levels and term symbols

State	Term Symbol	Level, i	Energy, E_i (cm^{-1})	g_i
Ground State	$4^2S_{\frac{1}{2}}$	1	0	2
Upper Laser State	$4^2P_{\frac{3}{2}}$	2	12,985.186	2
Pumped State	$4^2P_{\frac{1}{2}}$	3	13,042.896	4
Intermediates	$4^2D_{\frac{3}{2},\frac{5}{2}}$	4	27,398.147	4
			27,397.077	6
	$5^2P_{\frac{1}{2},\frac{3}{2}}$	5	24,701.382	2
			24,720.139	4
	$6^2S_{\frac{1}{2}}$	6	27,450.710	2
Rydberg States	higher n	7	28,000-35,009	
Atomic Ion	$^1S_0$	8	35,009.814	1
Ionic Dimer	$X^2\Sigma_g$	9	28,880	2

2.2.2 Three Level DPAL.

The power peformance of various DPAL systems is usually well characterized by three-level kinetic models (24; 25). The original model developed by Beach et al (26)
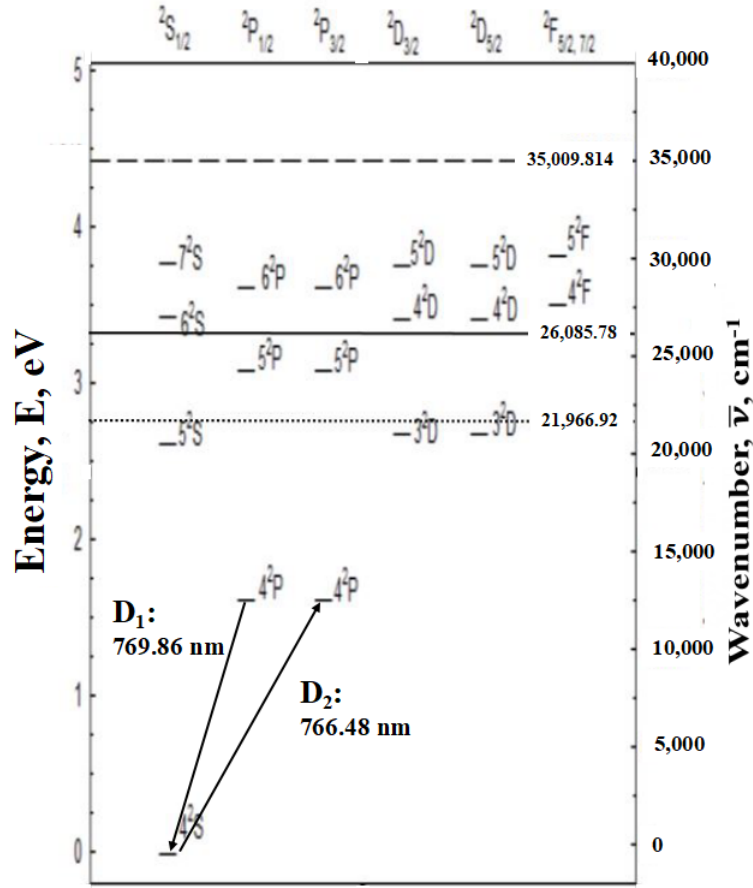
Figure 3. A energy diagram of potassium. The lowest three states form the standard DPAL system. The solid line at $21,996\,cm^{-1}$ represents the energy of one pump photon above the $4P$ states. States above the dashed line can be ionized by a D_1 or D_2 photon.

was extended to include longitudinal averaging (14) and broadband diodes (15). More recent variants and extensions of this approach have been reported (9; 27; 28; 29). The current study of multi-level kinetics begins with the baseline performance of this ideal three-level system.

Diode excitation from the ground $4\,^2S_{\frac{1}{2}}$ state, with a population n_1, to the pumped $4\,^2P_{\frac{3}{2}}$ state, with population n_3, proceeds via optical absorption on the D_2 transition:

$$n_1 + h\nu_p \rightarrow n_3 \tag{1}$$

11

where h is Plank's constant and the absorption cross-section at line center, σ_{13}, is:

$$\sigma_{13} = \frac{g_3}{g_1}\sigma_{31} = 2\frac{\lambda_p^2}{8\pi}A_{31}g_{31}(\nu_0) \tag{2}$$

where g_i is the degeneracy of the i-th state, λ_p is the pump wavelength, A_{31} is the spontaneous emission rate for the D_2 transition, and $g_{31}(\nu)$ is the spectral line shape. The core line shape is nearly Lorenztian at the DPAL elevated pressures and at line center,

$$g_{31}(\nu_0) = \frac{2}{\pi\Delta\nu_L} \tag{3}$$

The Lorentzian width increases with pressure, $\Delta\nu_L = \sigma_b^{D2}uM$ where the broadening cross-section is weakly temperature dependent (30), u is the relative collision speed for the alkali-rare gas partner, and M is the rare gas concentration. At $T = 460\,K$ and helium pressure P= 760 Torr the D_2 line width is 40.3 GHz.

Fine structure mixing is induced by a buffer gas, typically helium, with concentration M:

$$n_3 + M \rightarrow n_2 + M \tag{4}$$

and is rapid, $k_{32}(400K) = 2.72 \times 10^{-10}\,cm^3/atom - s$ (31). We use the most recently derived value for the spin-orbit cross section, assuming independence of temperature, however a temperature dependence may be derived from the many calculated values of this measurement (31; 32; 33; 34; 35). The inverse rate for fine structure mixing:

$$n_2 + M \rightarrow n_3 + M \tag{5}$$

is favored for potassium, with the bi-molecular rate coefficient constrained by detail balance:

$$k_{23} = k_{32}\frac{g_3}{g_2}exp[-(E_3 - E_2)/kT] = k_{32}2e^{-\theta} \tag{6}$$

12

where $\theta = \frac{E_3 - E_2}{kT}$ is associated with the spin-orbit splitting.

For a helium buffer gas pressure of 10 atmosphere at $T = 400$ K, the first order mixing rate is $\gamma_{32} = k_{32}M = 4.99 \times 10^{10}\,s^{-1}$, or $\kappa = \gamma_{32}/A_{31} = 1,309$ cycles per radiative lifetime. At higher pressures the fine structure mixing rate can be enhanced by three body collisions . For a Rb-He mixture, three body collisions double the spin orbit rate at 3,000 Torr (36). However, the much faster two body rate in potassium will dominate the three body rate for realistic pressures, so it will be excluded from the mixing rate.

Relaxation back to the ground state can proceed via spontaneous emission at the pump or lasing frequency, $\nu_{p,l}$:

$$n_3 \rightarrow n_1 + h\nu_p \tag{7}$$

$$n_2 \rightarrow n_1 + h\nu_l \tag{8}$$

with rates $A_{31} = 3.80 \times 10^7\,s^{-1}$ and $A_{21} = 3.75 \times 10^7\,s^{-1}$, or via quenching:

$$n_3 + M \rightarrow n_1 + M \tag{9}$$

$$n_2 + M \rightarrow n_1 + M \tag{10}$$

The quenching rates, k_{31} and k_{21}, for collisions with pure helium are sufficiently low to usually be neglected (37). We define the total decay rate from the two excited states as $\gamma_3 = A_{31} + k_{31}M$ and $\gamma_2 = A_{21} + k_{21}M$. Finally, the new lasing process terminates on the ground state:

$$n_2 + h\nu_l \rightarrow n_1 + 2h\nu_l \tag{11}$$

where the stimulated emission cross-section at line center is:

$$\sigma_{21} = \sigma_{12} = \frac{\lambda_l^2}{8\pi} A_{21} g_{21}(\nu_0) \tag{12}$$

The K-He D_1 line collision induced spectral broadening cross section is $\sigma_b^{D1} = 3.21 \times 10^{-16}\,cm^2$ (13.1 MHz/Torr) at 328 K, 66% of the D_2 rate of $\sigma_b^{D2} = 48.7 \times 10^{-16}\,cm^2$ (19.8 MHz/Torr) (4; 38). We suggest scaling the broadening rates with temperature assuming no temperature dependence for the collisional cross section (39):

$$\Delta\nu_L = \gamma(T_1)P(\frac{T}{T_1})^{\frac{1}{2}} \tag{13}$$

where T_1 is the temperature at which the cross section is measured.

AFIT-ENP-DS-18-D-009A comparison of the performance for the K, Rb, and Cs DPAL variants is provided in Table 3. The quantum efficiency is high $\eta_{qe} = 0.95 - 0.99$, with fine structure splitting relative to the kinetic energy, $\theta = (E_3 - E_2)/kT$, ranging from 0.181-1.739 at 460 K. The He mixing rate is rapid in potassium $k_{32}(460\,K) = 2.91 \times 10^{-10}\,cm^3/(atom - s)$ (32), moderate for rubidium $k_{32}(460\,K) = 2.52 \times 10^{-12}\,cm^3/(atom - s)$ (40), and too slow for cesium, $k_{32}(460\,K) = 9.49 \times 10^{-15}\,cm^3/(atom - s)$ (40). The Cs system requires the addition of a hydrocarbon to induce sufficient mixing. The temperature dependence of the spin-orbit cross section is missing in potassium, however it may be added using a recent scaling law from Eshel et. al (41). The buffer gas pressure necessary to achieve a mixing rate 20 times larger than the radiative rate, $\kappa = k_{32}M/A_{31}$ increases for the heavier alkali vapors. Each atom cycles in the lasing process κ times per spontaneous event, a remarkable feature of the DPAL system. The helium pressure required to achieve this cycle rate increases from 125 Torr for potassium to 17,550 Torr for rubidium. Buffer gas pressures of 760 Torr require very aggressive diode bar spectral narrowing

14

for efficient DPAL performance; 125 Torr would require narrowing not yet feasible at high pump powers. A helium pressure of 5.08×10^6 Torr would be required to achieve a $\kappa = 20$ for cesium. Therefore, in Table 3 760 Torr of helium is assumed for both potassium and cesium; whereas $\kappa = 20$ for cesium is achieved by introducing a modest amount of hydrocarbons. The melt temperature, T_m, decreases for the heavier metal atoms and correspondingly the alkali density, N, at $T = 460$ K increases. The fractional population inversions, Δ/N, have been evaluated using the longitudinally averaged pump intensity formalism by Hager et al (14). For the quasi-two level (Q2L) limit, where the fine structure mixing rate is infinite and the pump transition is nearly transparent, the steady state small signal (no lasing) inversion Δ_0^{Q2L}, is a larger fraction of the total alkali density for the heavier atoms, where the fine structure splitting is larger. Indeed, for sodium and lithium, the system approaches two levels, the fractional inversion is low, and lasing has not been achieved. The fractional small signal inversion for the finite mixing rate associated with $\kappa = 20$ and a longitudinally averaged intracavity pump intensity, $\Omega = 10\,kW/cm^2$, is most similar to the Q2L limit for for the lighter alkali. The diode pump intensity required to achieve $\Omega = 10\,kW/cm^2$, with a high absorbance $A = \sigma_{21}nl = 100$, increases from 14.0 kW/cm^2 for K to 20.9 kW/cm^2 for cesium. The relation between diode pump intensity, I_p, and longitudinally averaged pump intensity, Ω, is given, for lasing cavity of length $l_g = 10$ cm with nearly no loss ($t = 0.97$) and complete reflection of the pump diode at cell windows, and an output coupler reflectance of $r = 0.2$, corresponding to a gain threshold of $g_{th} = 0.086\,cm^{-1}$, by (14):

$$\Omega = (\frac{I_p}{\sigma_{31}(n_3 - 2n_1)l_g})(exp[2\sigma_{31}(n_3 - 2n_1)l_g] - 1) \tag{14}$$

Methods for calculation of the average intracavity lasing intensity, Ψ, and the output lasing intensity, I_l, from the parameters described above is demonstrated by Hager

15

et. al (14). The optical-optical efficiency is generally high, $\eta_{oo} = \frac{I_l}{I_p} = 0.70 - 0.80$.

Table 3. Three level DPAL performance characteristics at $T = 460$ K

Property	Potassium, K	Rubidium, Rb	Cesium, Cs
n (ground state)	4	5	6
λ_p, D_2 (nm)	766.48	780.03	852.11
λ_l, D_1 (nm)	769.89	794.76	894.35
$\eta_{qe} = \lambda_p/\lambda_l$	0.995	0.982	0.953
$\theta = (E_3 - E_2)/kT$	0.181	0.746	1.739
$A_{31}(sec^{-1})$	3.80×10^7	3.81×10^7	3.28×10^7
A_{21}/A_{31}	0.984	0.947	0.873
P_{He} (atm)	1	20	1
Ionization (eV)	4.340	4.177	3.984
Saturation Intensity (W/cm^2)	22.28	350.17	16.80
T_m (K)	336.4	312.3	301.4
$N(460$ K$)$ $(10^{14}\, cm^{-3})$	0.84	5.40	11.0
$N(A = 100)$ $(10^{14}\, cm^{-3})$	0.11	1.80	0.11
Δ_0^{Q2L}/n	0.048	0.222	0.551
$\Delta_0/n\,(\kappa = 20)$	0.039	0.183	0.513
I_p (kW/cm^2)	13.6	141.4	20.8
I_l (kW/cm^2)	10.4	98.9	16.6
η_{oo}	0.76	0.70	0.80

The output power of a DPAL system can be scaled by increasing diode pump intensity, or increasing the pumped area. Figure 4 provides the intensity scaling for the potassium system, assuming population is constrained to the three primary levels, using the longitudinally averaged approach (14; 15). Threshold pump intensity is controlled by the requirement to bleach the full volume and scales linearly with alkali density. Scaling is linear with pump intensity until the system begins to bottleneck and is limited by the fine structure mixing rate. Increasing the cycle rate with a higher buffer gas pressure can increase this rate. The transition from the linear response to the bleached limit is rather abrupt for narrow band diodes, but somewhat shallower for broader spectral bandwidth.

The heat load for the three level system, in a volume V, is dominated by energy

16
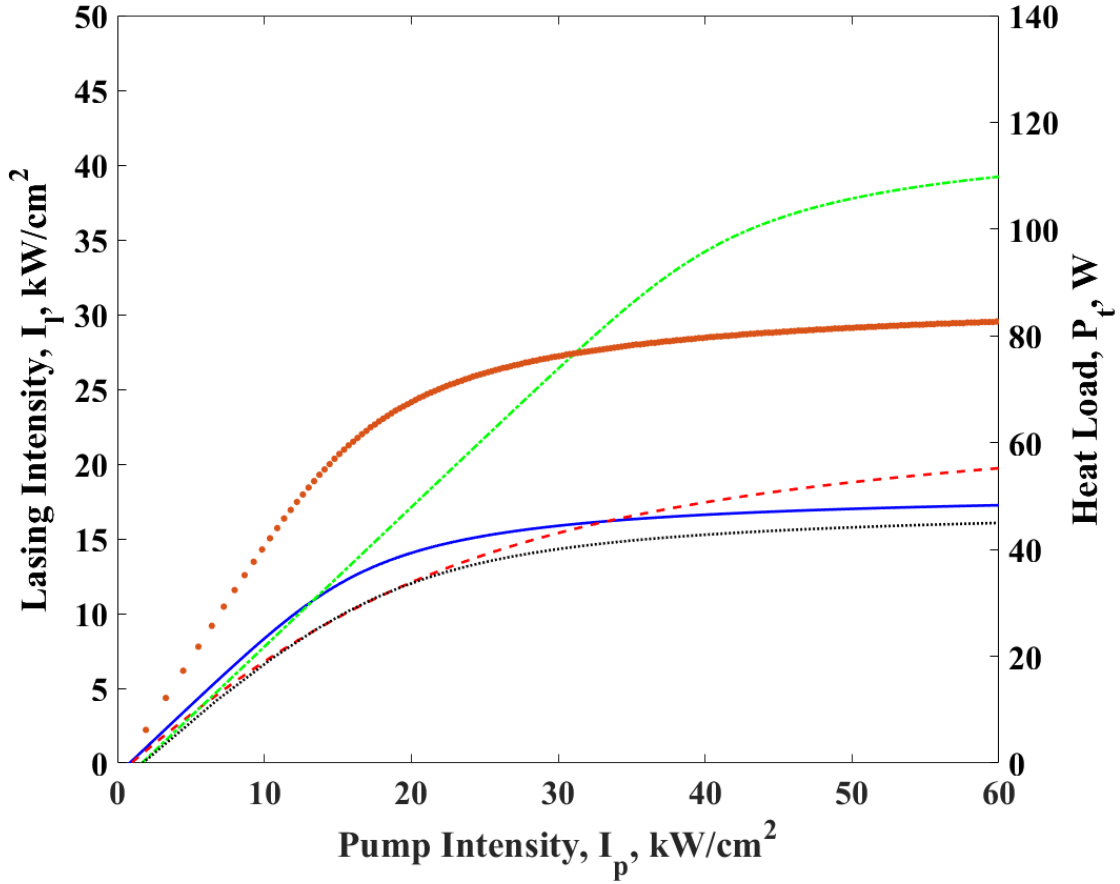
Figure 4. Scaling of laser intensity with diode pump intensity in different regimes of Hager's model (14; 15). The solid blue line corresponds to the parameters in Table 3, the helium pressure is raised to 2 atm for the red dashed line ($-$), and the potassium density is doubled for the green dash-dot line ($-\cdot$). The small, black dotted line corresponds to a broadening of the pump source to 30 GHz and a pressure broadened Lorenztian absorption feature of the D_2 transition. The red dots ($\bullet$) represent the heat loading of the original parameters in Table 3 with narrowband optical pumping.

release in the fine mixing rate, as the quenching of the $n^2P_{\frac{3}{2},\frac{1}{2}}$ states is quite low (14):

$$P_t = k_{32}M(n_3 - 2e^{-\theta}n_2)(E_3 - E_2)V \tag{15}$$

For the conditions of Table 3, the potassium thermal power loading is, $P_t = 65.8\,W$. This corresponds to a heating rate of $dT/dt = 7,731\,K/s$, assuming no heat transfer. To keep the temperature rise modest, about 5 K, a longitudinal flow velocity of 146

17

m/s, or a transverse flow speed of 14.6 m/s is required. Excitation of higher lying states will certainly increase the thermal effects and degrade beam quality or require higher gas flow rates. With the three level baseline performance established, we now turn to assess the influence of the multi-level kinetics.

2.2.3 Intermediate States.

The production of higher lying states will depopulate the three-level laser system, reducing the number of alkali atoms available to cycle, n_a, by an amount δ, and thus reducing output power. Increasing the initial alkali density to compensate for this loss can largely mitigate this effect. The spatial distribution of alkali density due to localized heating could prevent a complete compensation. Furthermore, the heat load from quenching of these higher lying states may also degrade beam quality. To address these issues, we develop a multi-level kinetics model.

First consider the intermediate K $6\,^2S_{\frac{1}{2}}$, $5\,^2P_{\frac{3}{2},\frac{1}{2}}$ and $4\,^2D_{\frac{5}{2},\frac{3}{2}}$ states near the energy associated with two pump photons, as shown in Figure 3. The $5\,^2S_{\frac{1}{2}}$ and $3\,^2D_{\frac{5}{2},\frac{3}{2}}$ states lie below the energy required for single step photo-ionization, and are thus excluded from the intermediate states. Several slow processes might contribute to the production of the intermediate states, including: (1) energy pooling, (2) far wing absorption of pump or laser radiation, and (3) two-photon absorption.

Energy pooling involves two excited atoms from the pumped or upper laser level states, n_i and $n_j = 2$ or 3 colliding to produce an intermediate $n_f = 4-6$ and ground state atom:

$$n_i + n_j \rightarrow n_f + n_1 \tag{16}$$

The final states, f, include both fine structure split levels. The pooling rates for excitation into each doubly excited (intermediate) state have been experimentally derived for most of the alkalies (42; 43; 44; 45), and for many hetero-nuclear reactions

18

(46). The energy pooling cross section for this reaction in Rb-K and Rb-Na has been modeled as a function of the energy difference for the pooled state and the sum of the energies of the two parent states (47). We extend this scaling to the full set of observed alkali pooling reactions as shown in Figure 5. The observed rates have been re-interpreted when needed to include both fine structure split product states in the cross-section. The experimental results were observed at temperatures ranging from $350 - 597$ K (42; 44; 45; 47). The cross section, σ^p, is related to the rate coefficient, k^p, via the average relative collision speed, u:

$$k^p_{i,j:f} = u\sigma^p_{i,j:f} \tag{17}$$

While there is some scatter in the results, an exponential dependence on the absolute energy difference is well supported. Angular momentum considerations appear to be less significant. The scaling is asymmetric comparing results for excess and insufficient energy collisions, so two fits will be given. An un-weighted fit of the observations to the form:

$$\sigma^p_{i,j:f} = \sigma^p_{o\pm}e^{a_{pm}\Delta E/kT} \tag{18}$$

where $\Delta E = E_f - E_i - E_j$, yields $a_+ = -0.71 \pm 0.28$ $\sigma^p_{o+} = 3.58 \pm 1.8 \times 10^{-14} cm^2$ and $a_- = 0.84 \pm 0.04$ $\sigma^p_{o+} = 1.60 \pm 0.58 \times 10^{-14} cm^2$. The fit values with the subscript $+$ are used when $\Delta E > 0$, and $-$ when $\Delta E < 0$. The rate coefficients for the most resonant cases are near gas kinetic, $k^p \sim 10^{-10} \, cm^3/(atom-s)$, but the alkali density is low, $N \sim 10^{14} \, atoms/cm^2$, so the characteristic time scale is long $\tau_p = 1/k^p N \sim 0.1 \, ms$. That rate corresponds to $\sim 10^{-5}$ of the fine structure mixing rate and a minor influence on upper laser level population. However, the relaxation rates will be required to assess the steady state concentrations.

The experimental results presented in Figure 5 validates the need for a predictive

19

tool, demonstrating significant scatter in individual results, an asymmetry about the origin and a lack of consistency in J dependence. The values plotted here are not J-state specific with regard to the final state, however, they are split for the two exciting states. Additionally, some rates, like $4\,^2P \to 4\,^2D$ in potassium and $5\,^2P \to 6\,^2P$ in rubidium, are missing from the literature. Thus we use the scaled rates rather than specific experimental observations. The factor of 5 difference in the scaled and various experimental rates introduces less uncertainty than both the far wing absorption and quenching rates in the final prediction. Their rates were found to be between $4.00 - 7.07 \times 10^{-11}\,cm^3/(atom - s)$ at $T = 460$, and can be found as summarized in Table 6.
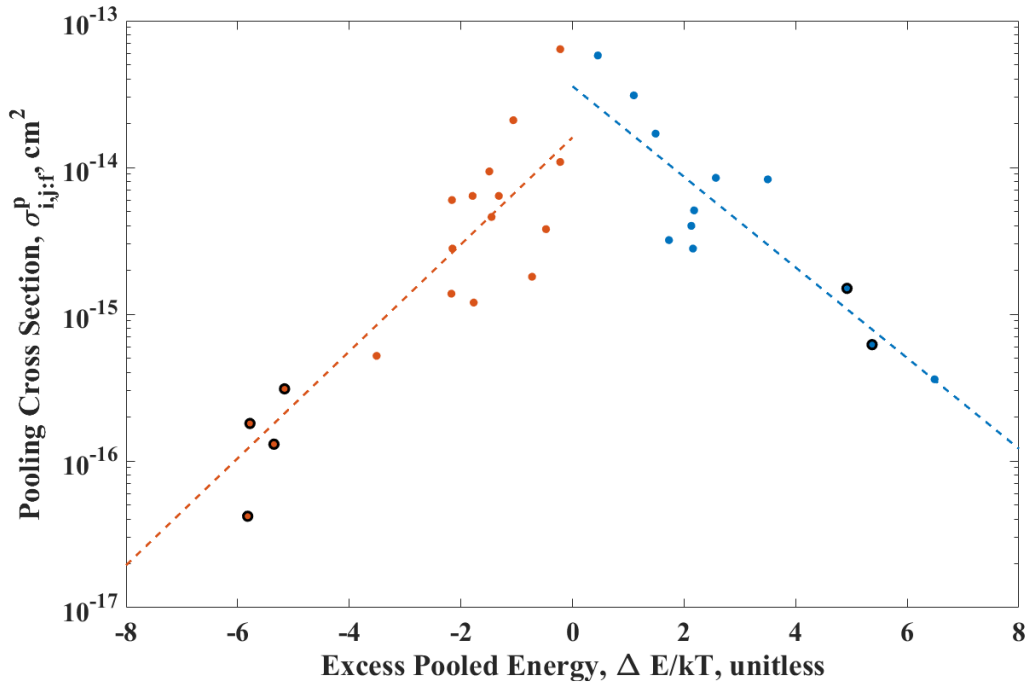
Figure 5. Pooling cross section as a function of excess energy. The circled points represent the rates in potassium. A positive ΔE corresponds to an energy level below the pooled energy. The dashed line is fit similar to Gabbanini _et. al_ (47), where it is suggested that the fit is better where $\Delta E > 0$.

Single photon absorption from the pumped or upper laser level may also populate the intermediate states, but would be far from resonance (10). For potassium the

D_2 pump radiation would lie 1,131 cm^{-1} to the red of the nearest $4\,^2P_{\frac{3}{2}} - 4\,^2D_{\frac{3}{2}}$ resonance. At 760 Torr of helium, this would correspond to 446 Lorentzian widths from line center, assuming a broadening rate of 100 MHz/Torr. Experimental values for the excited line shapes are not available. However, a better estimate for the broadening rates for the $4\,^2P_{\frac{3}{2},\frac{1}{2}} \rightarrow 4\,^2D_{\frac{5}{2},\frac{3}{2}}$ and $6\,^2S_{\frac{1}{2}}$ transitions might be provided by the quantum defect radii (41). We use a helium radii of $r_{He} = 8.89 \times 10^{-9}$ cm and the radii of the intermediate states from quantum defect theory:

$$n^* = \sqrt{\frac{E_{Ryd}}{E_I - E}} \qquad (19)$$

$$< r > = a_0 n^{*2}[1 + \frac{1}{2}(1 - \frac{l(l+1)}{n^{*2}})] \qquad (20)$$

E_{Ryd} is the Rydberg constant, $E_I - E$ is the energy gap between the excited state, E, and the ionization potential, E_I. a_0 the Bohr radius, and l is the orbital angular momentum quantum number. The predicted broadening cross section using quantum defect theory are:

$$\sigma_{QD} = \pi(r_{He} + < r >)^2 \qquad (21)$$

The quantum defect broadening cross sections for the P-D and P-S transitions are $3.62 \times 10^{-14}\,cm^2$ and $4.84 \times 10^{-14}\,cm^2$, respectively. These cross sections corresponds to 134.4 and 179.7 MHz/Torr at $T = 460\,K$. We assume that the broadening is dominated by the upper (intermediate) state surface. Wing absorption to the $5\,^2P_{\frac{3}{2},\frac{1}{2}}$ states is excluded, as the transitions are not electric dipole allowed.

High pressure line shapes far from resonance are non-Lorentzian and can exhibit secondary maxima due to extrema in the interaction difference potentials. These far wing profiles are very sensitive to the interaction potentials (30; 48). Unfortunately, the potentials for the higher lying state are available only at modest fidelity, not including any spin orbit effects (49). The $^2\Pi$ and $^2\Sigma^+$ potentials are calculated for

21

the K-He complex for the $4P$ and $4D$ states, and the difference potentials of these are presented in Figure 6. The top plots represent the two difference potentials with the $^2\Sigma^+\,4P$ state, and the bottom use the $^2\Pi\,4P$. The attractive nature of the bottom difference potentials will lead to an enhancement on the red side of this transition, and the shallow minimum of the $^2\Sigma^+\,4D -^2\Pi^+\,4P$ curve may lead to a satellite on the blue side. Robust potentials are required to better assess these non-Lorentzian effects.
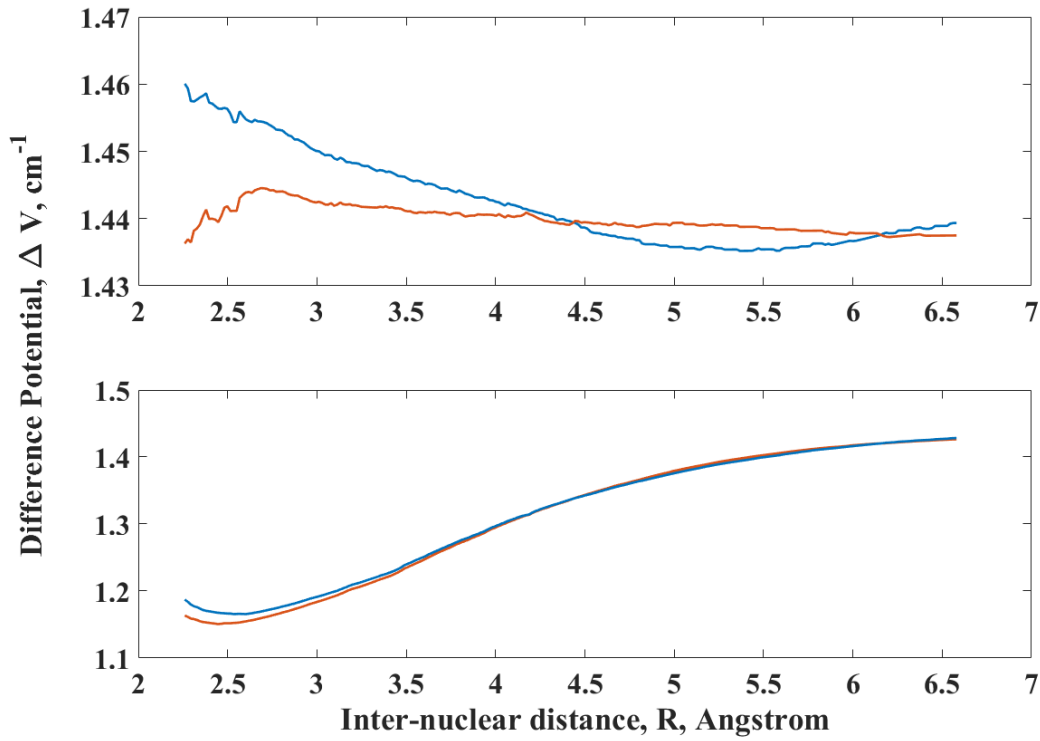
Figure 6. Top: Difference potentials between two upper states–$^2\Sigma^+\,4D$ (blue) , $^2\Pi\,4D$ (orange)–and the $^2\Sigma^+\,4P$ state. Bottom: Difference potentials between two upper states–$^2\Sigma^+\,4D$ (blue) , $^2\Pi\,4D$ (orange)–and the $^2\Pi\,4P$ state.

The quantum defect Lorentzian cross section serves as a basis for evaluating the absorption into the wings. In Table 4 each of the intermediate states is coupled to both the pumped and upper laser levels by both pump and laser fields. While the excess energy for each of these transition is nearly the same, the cross sections for

have a much larger range.

Table 4. Absorption cross section into the far wings for each transition at $T = 460\,K$ and $P = 760$ Torr.

Initial State	Final State	Broadening cross section (cm^2)	Pump Source	Energy Off Line Center (cm^{-1})	Cross-section (cm^2)
$4\,^2P_{\frac{3}{2}}$	$4\,^2D_{\frac{5}{2}}$	4.84×10^{-14}	D_1	-1,369.0	6.29×10^{-23}
			D_2	-1,426.3	5.77×10^{-23}
	$4\,^2D_{\frac{3}{2}}$		D_1	-1,370.0	1.03×10^{-23}
			D_2	-1,427.7	9.46×10^{-24}
	$6\,^2S_{\frac{1}{2}}$	3.62×10^{-14}	D_1	-1,422.6	9.76×10^{-21}
			D_2	-1,480.3	8.88×10^{-21}
$4\,^2P_{\frac{1}{2}}$	$4\,^2D_{\frac{3}{2}}$	4.84×10^{-14}	D_1	-1,312.3	4.78×10^{-23}
			D_2	-1370.0	4.40×10^{-23}
	$6\,^2S_{\frac{1}{2}}$	3.62×10^{-14}	D_1	-1,364.9	6.21×10^{-21}
			D_2	-1,422.6	5.67×10^{-21}

The uncertainty in cross sections and proximity of the D_1 and D_2 lines suggest simplification of the wing absorption rate from each state, R_i^w, to a single term:

$$R_i^w = \frac{\alpha \sigma_L^i}{h\nu}(\Omega + \Psi)n^* \tag{22}$$

where the total population in the pumped and upper laser level is defined as $n^* = n_2 + n_3$. Recall, the intracavity pump intensity, Ω is given in Eq. 14 and the intracavity lasing intensity, Ψ, is developed for the three level system in reference (14). The wing absorption is separated into the Lorenztian cross section, σ_L^i, and an adjustable parameter, α, that accounts for the enhancement or degradation of the value due to non-Lorentzian behavior. In general, weighting the pump and lasing fields equally is likely inaccurate, with the rate due to the lasing field likely lower due to increased detuning from line center. Numeric estimates for the absorption cross section $4P - 5S$ transition near $1.2\ \mu m$ in potassium have demonstrated cross sections in the far wings of the absorption profiles over two orders of magnitude larger than expected

for Lorenztian detuning of 750 cm^{-1} (50). Other simulations show that the far wings of the excitation cross section of the $4S - 4P$ can be increased over 1,000 times larger than a Lorenztian broadened line (51). The value of alpha is a function of helium pressure (52), however experimental results are required to determine this dependence. Further study of the far wing line shape for the excited-excited state transitions is clearly needed. We use $\alpha = 1$ for our baseline analysis.

Population of the intermediate states by pooling may dominate at higher alkali density, lower pump intensity and lower buffer gas density. Assuming a wing absorption cross section of $1.05 \times 10^{-19} \, cm^2$, commensurate to the $4\,^2P \rightarrow 6\,^2S$ rate at 760 Torr, the K pooling and wing absorption rates are equal at $n = 1.50 \times 10^{13} \, atoms/cm^3$ and $\Omega_p = 13.4 \, kW/cm^2$, or $n = 2.95 \times 10^{14} \, atoms/cm^3$ and $\Omega_p = 263 \, kW/cm^2$. Wing absorption may dominate in most high power DPAL systems.

Two-photon excitation from the ground state to the $6\,^2S$ or $4\,^2D$ states is significant when the pump radiation is tuned to the degenerate wavelength, 728.8 nm and 729.9 nm, respectively (53). Indeed, these transitions can be bleached with pulsed lasers, and lasing has been observed after two photon pumping with thresholds as low as $260 \, kW/cm^2$ (54). The two photon excitation cross section is a function of the single photon dipole moments and degree of detuning of the virtual states from the n^2P states (54):

$$\sigma_{if}^{(2)}(\nu) = \frac{\pi^2 \nu}{5h^3c^2\epsilon_0^2} \sum_n \frac{1}{g_i g_n} \frac{\mu_{fn}^2 \mu_{ni}^2}{(\nu_{ni} - \nu)^2} g_f(\nu_{fi} = 2\nu) \tag{23}$$

The sum introduced is over all atomic energy states, but only the states closest to the virtual state contribute substantially to the total. The subscript n denotes properties of these real intermediate states, μ_{ni} is the dipole moment between the initial and intermediate states, ν_{ni} is the frequency associated with that transition, and $g_f(\nu_{fi} = 2\nu)$ is the line shape for the single photon transition from the initial

24

to the final state. For example, the virtual state is detuned from the $4\,^2P_{\frac{3}{2}}$ by 682.5 cm^{-1} for the K $4\,^2S_{\frac{1}{2}} - 6\,^2S_{\frac{1}{2}}$ two photon transition and the peak cross section is predicted $\sim 1.2 10^{-25}\, cm^4/W$. For a diode pump at $10\, kW/cm^2$ the corresponding rate is $44.36\, sec^{-1}$. However, at the pump and lasing wavelengths, the two photon cross section is highly detuned from resonance and the rates are negligible. Thus, we neglect the two photon excitation.

Radiative decay from the intermediate and higher lying states occurs via cascading through several $\Delta L = \pm 1$ transitions. The spontaneous emission rates for K are summarized in Figure 7 and Table 5 (3). For example, the $5\,^2P_{\frac{3}{2}}$ intermediate state radiates most rapidly to the $5\,^2S_{\frac{1}{2}}$ state with a branching ratio of 0.63. Then the $5\,^2S_{\frac{1}{2}}$ state radiates to the $4\,^2P_{\frac{3}{2},\frac{1}{2}}$ states with a combined rate of $2.35 \times 10^7\, sec^{-1}$. The cascade fluorescence complicates the processes and increases the the number of states that need to be monitored. This table also introduces a statistical fraction that corresponds to the percent of the population in each spin orbit split state.

$$f_i = \frac{g_i \exp\left(E_i/kT\right)}{\Sigma_j g_j \exp\left(-\Delta E/kT\right)} \tag{24}$$

g_i is the degeneracy of the state and the sum is over all the split states. When calculating the total A-coefficient out of model state, each individual term is modulated by this fraction.

$$A = \Sigma_i f_i A_i \tag{25}$$

Quenching by buffer gas collisions also contributes to the relaxation, but these rates are less established. Quenching of higher lying S and D states in Na (55) and Rb (56; 57), moderate S and D states in Cs (58) ,and the $10\,^2P$ state in K (59) have been observed. While quenching in the lowest P states is so slow as to be difficult to measure (60), inter-multiplet transfer strongly augments the rates for higher levels,

with rates of $3.3 - 210 \times 10^{-11} \, cm^3/(atom - sec)$. Quantum defect theory has been used to predict these rates and has been experimentally verified in lithium (61).

We choose to neglect the details of this relaxation and employ a single radiative and quenching term for each intermediate state. The recommended values are provided below in Table 6. The $5\,^2P$ states require extra care as they can be populated by the other intermediate states, $4\,^2D$ and $6\,^2S$, via both spontaneous emission and quenching. The branching ratios of the emission rates from $4\,^2D$ and $6\,^2S$ to $5\,^2P$ is in Table 5, but the proportion of quenching that terminates on 5^2P is unclear. The products created by quenching of the intermediate states, in general, are important to the heat loading. The upper bound to the additional heat occurs if intermediates were quenched directly to the ground state. This, while unlikely, would lead to the least promising estimate of the beam quality. Quenching terminated on the nearest lower state is a more likely scenario. A third approach is to follow the branching ratios determined for the radiative rates as perturbation theory often leads to matrix elements that share the dipole moment. We chose this approach as an intermediate estimate between the other two extremes. Quenching from the Rydberg states will assumed to equally populate the three intermediates states, as the heat release is similar. The total quenching rate will be a model variable, and will require benchmarking. New experimental observations, and analysis of side fluorescence in a 1 kW flowing potassium DPAL system are in progress and will be particularly helpful in defining the quenching rates.

Production of the lowest three levels due to radiative and collisional relaxation from higher lying states is neglected, as the total population in the intermediate state is expected to be a small fraction of the total alkali density.

Cascade lasing among these higher lying states has been observed, but only after two photon excitation (54). The energy pooling and wing absorption production rates
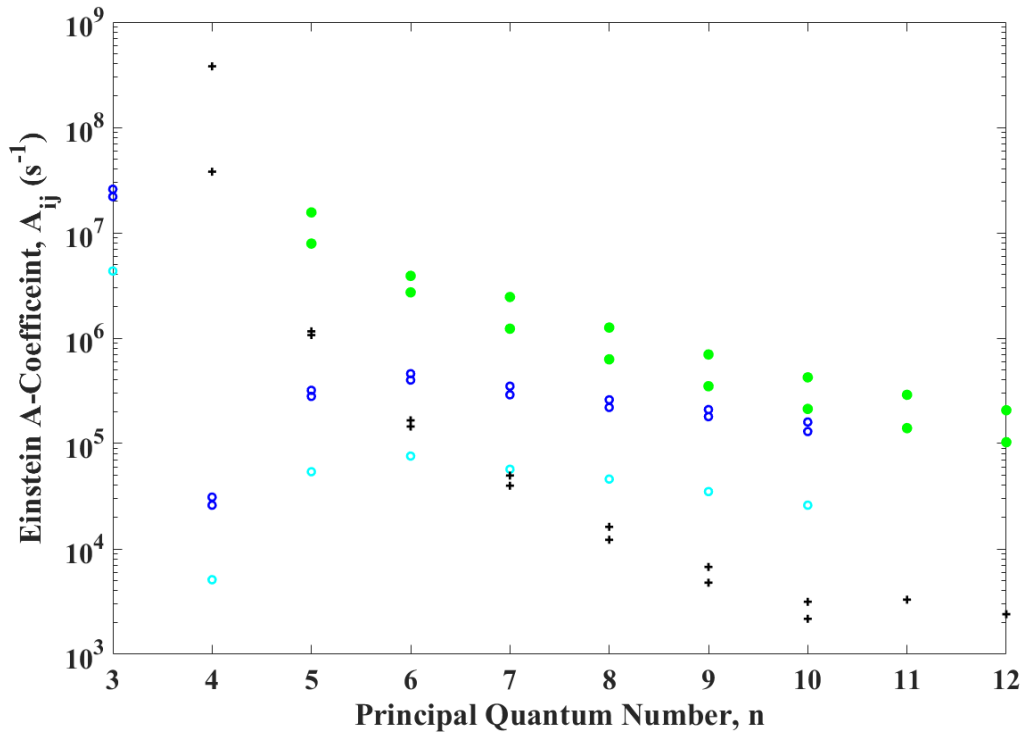
Figure 7. The Einstein A-coefficient for transitions in potassium as a function of the quantum number of the initiating state. Each trend is a different transition type; (green ●) $S_{\frac{1}{2}} \rightarrow P_{\frac{3}{2},\frac{1}{2}}$, $D \rightarrow P$ (dark blue ○: $D_{\frac{3}{2}} \rightarrow P_{\frac{3}{2},\frac{1}{2}}$ and light blue ○: $D_{\frac{5}{2}} \rightarrow P_{\frac{3}{2}}$), and (black +) $P_{\frac{3}{2},\frac{1}{2}} \rightarrow S_{\frac{1}{2}}$.

Table 5. A-coefficient and branching of the intermediate states (3)

	Initial Level	Statistical Fraction	Terminating Level	A-Coefficient (sec^{-1})	Branching Ratio	ΣA	Total A	Terminating Model Level	Model Branching Ratio
4	$4\,^2D_{\frac{3}{2}}$	0.4	$4\,^2P_{\frac{3}{2}}$	5.1×10^3	0.002	3.5×10^6	3.44×10^6	5	0.9904
			$4\,^2P_{\frac{1}{2}}$	2.6×10^4	0.007				
			$5\,^2P_{\frac{3}{2}}$	5.7×10^5	0.163			3	0.0088
			$5\,^2P_{\frac{1}{2}}$	2.9×10^6	0.828				
	$4\,^2D_{\frac{5}{2}}$	0.6	$4\,^2P_{\frac{3}{2}}$	3.1×10^4	0.01	3.4×10^6		2	0.0008
			$5\,^2P_{\frac{3}{2}}$	3.4×10^6	0.99			1	0
5	$5\,^2P_{\frac{3}{2}}$	0.65	$4\,^2S_{\frac{1}{2}}$	1.16×10^6	0.16	7.31×10^6	7.23×10^6	3	0
			$5\,^2S_{\frac{1}{2}}$	4.6×10^6	0.63				
			$3\,^2D_{\frac{3}{2}}$	1.5×10^5	0.02				
			$3\,^2S_{\frac{5}{2}}$	1.4×10^6	0.19			2	0
	$5\,^2P_{\frac{1}{2}}$	0.35	$4\,^2S_{\frac{1}{2}}$	1.07×10^6	0.15	7.07×10^6			
			$5\,^2S_{\frac{1}{2}}$	4.5×10^6	0.64			1	1
			$3\,^2D_{\frac{3}{2}}$	1.5×10^6	0.21				
6	$6\,^2S_{\frac{1}{2}}$	1	$4\,^2P_{\frac{3}{2}}$	3.9×10^6	0.34	11.42×10^6	11.42×10^6	5	0.42
			$4\,^2P_{\frac{1}{2}}$	2.72×10^6	0.24			3	0.34
			$5\,^2P_{\frac{3}{2}}$	1.6×10^6	0.14			2	0.24
			$5\,^2P_{\frac{1}{2}}$	3.2×10^6	0.28			1	0

appear too slow to invert these levels under cw excitation on the D_2 line.

2.2.4 Ionization.

All three intermediate states are within one pump photon from ionization; needing only 7,611, 10,289, and 7,558 cm^{-1} to ionize from n_4, n_5 and n_6, respectively, where a pump photon has 13,043 cm^{-1}. Excitation of the intermediates states to produce ions may occur via direct photo-ionization, Penning ionization and Hornbeck-Molnar ionization. Photo-ionization may dominate for high pump intensities and moderate alkali densities. The three intermediates states, $i = 4,5$, and 6, can be photo-ionized by either the pump or laser radiation:

$$n_i + h\nu \rightarrow n^+ + e^- \tag{26}$$

where n^+ represents the concentration of the atomic ion and e^- represents the electron density.

These photo-ionization cross sections, σ_i^{ph}, have been computed as a function of the excess energy of the free electron for many lower S and D states (62). For the potassium P states, only the pumped $4\,^2P$ states have been reported, so the same trend was assumed for the higher P states (62). The photoionization cross sections for various excited states of potassium are provide in Figure 8. The cross section for the D states are highest and that of the S states are significantly lower. The photoionization cross sections were also computed using quantum defect theory (63) and are included in the figure. As n increases, the photoionization cross section decreases, but quantum defect theory does not capture this trend. While the cross sections depend on wavelength, the rates for the pump D_2 and lasing D_1 fields are nearly identical.

Penning ionization involves the collision or two excited alkali atoms and pools the

28
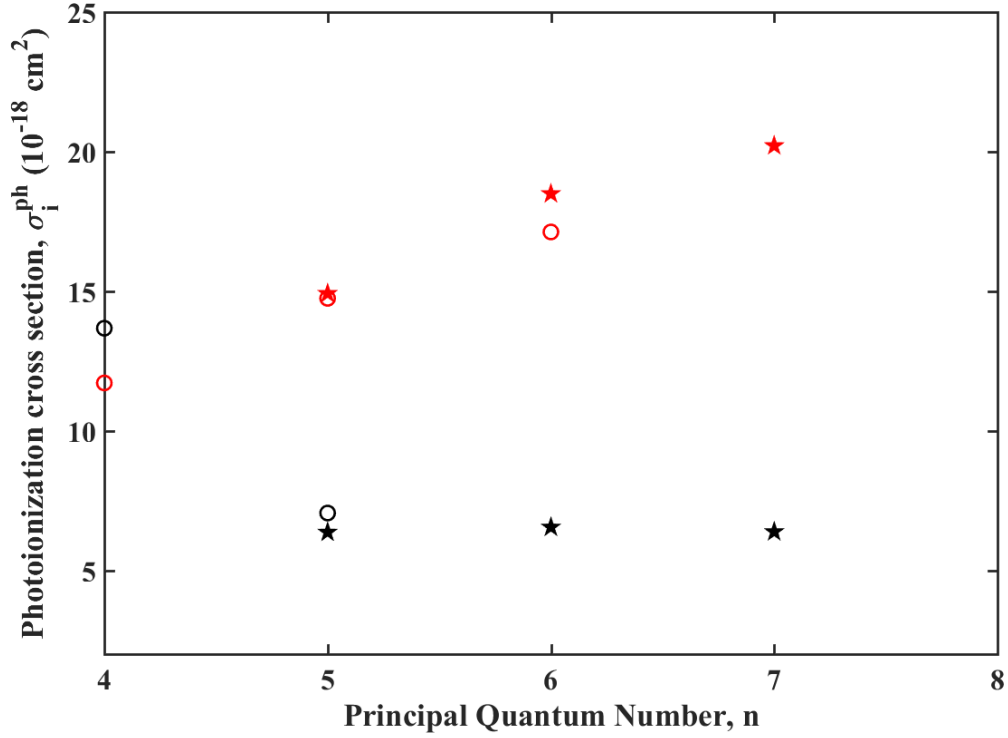
Figure 8. The photoionization cross sections for the $nP(\star)$ and $nD(\circ)$ in potassium are calculated from both the quantum defect theory (red) and numeric methods (black) (62).

energy to exceed the ionization potential:

$$n_i + n_j \rightarrow n^+ + e^- + n_1 \tag{27}$$

where $i = 4, 5$, or 6 and j can be any excited state. However, the concentration of the pumped $4\,^2P$ states is considerably larger than the intermediates, so the rate with the collision partner as n_2 or n_3 should dominate, and $j = 2$ or 3. The Penning ionization rates have not been measured in potassium. However, they were observed in rubidium for a wide range of energy levels, as shown in Figure 9 (64). The cross sections, σ^{Pen} are scaled here by the quantum defect cross section, σ_{QD}, to express a probability of Penning ionization. The effective quantum number is the most important factor in controlling this cross section, with only small variations due to angular momentum.

29

Even so, Penning cross sections are relatively independent of n, but as σ_{QD} grows with n^*, the probability decreases with more excess energy. This study did not distinguish between $^2P_{\frac{3}{2}}$ and $^2P_{\frac{3}{2}}$ collision partners, and only measured these rates out of S and D states (64). The values predicted for potassium have been added to Figure 9 along the exponential fit, $\sigma^{Pen}/\sigma_{QD} = (47.69 \pm 25.12) \exp((-0.67 \pm 0.23)n^*)$. The effective quantum number, n^* is very nearly equal for $4\,^2D$ and $6\,^2S$, so their points on the line are nearly overlapped. The predicted values in potassium are provided in Table 6.
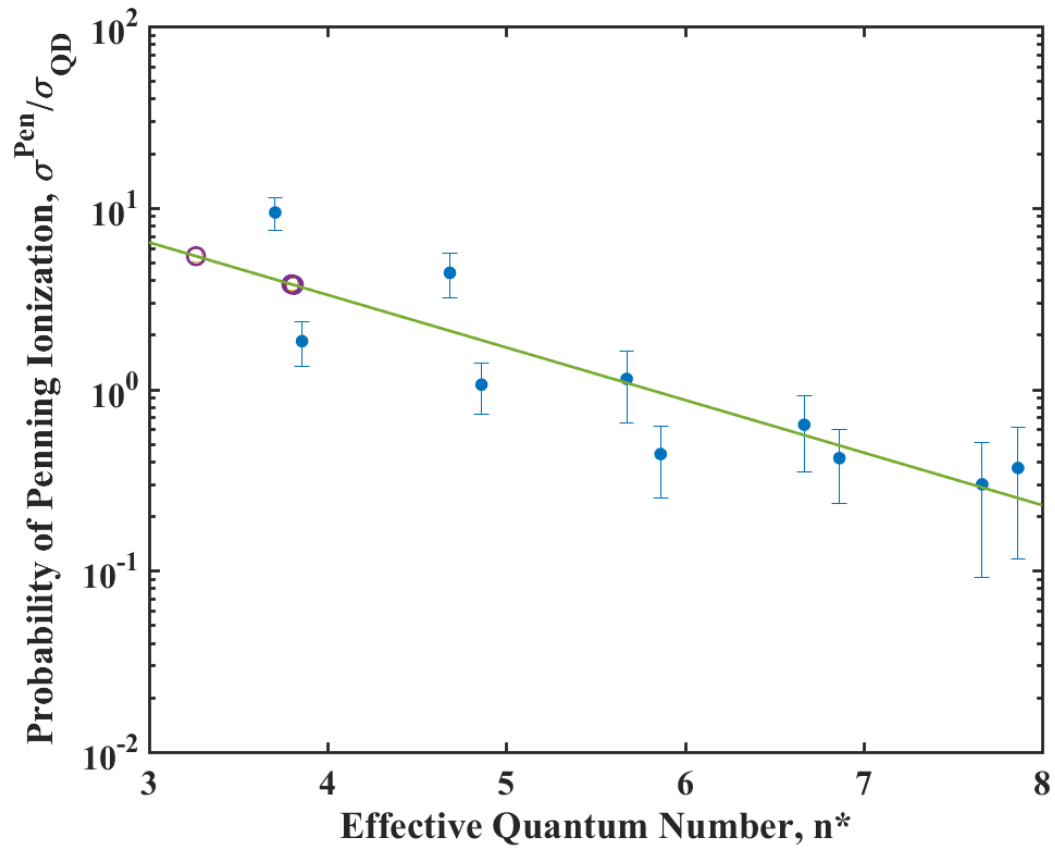
Figure 9. Cross-section for Penning ionization for: (•) Rb, (○) K, and (-) exponential fit to Rb calculations. (64).

A third mechanism to ionization occurs with the formation of the alkali dimer. This Hornbeck-Molnar ionization occurs when a collision between a ground state

atom and an excited atom can create an ionic diatom and a free electron. The rate coefficient for this is nearly 100 times smaller than the rate coefficient for Penning ionization for all excited states of rubidium (64) and is excluded in the current model.

2.2.5 Ion Recombination.

The balance of the photo and Penning ionization production with recombination processes controls the ion concentration. The rates for radiative recombination are portioned into various atomic neutral states j:

$$n^+ + e^- \rightarrow n_j + h\nu \tag{28}$$

and are slow, $k^{rr} < 10^{-13} \, cm^3/atom - sec$ (65), and excluded in the current model. The three-body recombination:

$$n^+ + e^- + M \rightarrow n_j + M \tag{29}$$

rate in Cs with helium as the collision partner is fast for such processes, $k_{3B} = 4 \times 10^{-29} \, cm^6/s$ (66). For a helium density of $M = 1.58 \times 10^{19} \, atoms/cm^3$, 760 Torr at $T = 460 \, K$, the effective bi-molecular rate coefficient is $k_{3B}M = 5.9 \times 10^{-10} \, cm^3/atom - s$, much faster than radiative recombination. We assume the dominant channel produces Rydberg states only, $j = 7$.

Dissociative recombination:

$$n_2^+ + e^- \rightarrow n_j + n_1 \tag{30}$$
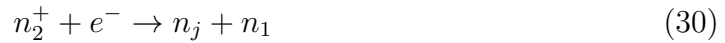
involves the diatomic ion with density, n_2^+, and likely yields high lying neutral atomic states with $j = 7$, the Rydberg states, as discussed below. In cesium, this rate

31

constant was calculated to be $k_{DR} = 5.26 \times 10^{-7} cm^3/atom - s$ for $T < 1,650\,K$ (67). This rate coefficient is much larger than the three-body recombination rate and will dominate if the dimer ion concentration is significant. This rate was calculated at temperatures much higher than that of a typical DPAL, and the dependence of this rate on temperature is not well established. In a less plasma-like environment, this rate may be dramatically lower. However, it is the only value for this rate in the literature, so it is cautiously used in this model. Molecular ions are created during a three-body collision between a neutral alkali atom, alkali ion, and the buffer gas:

$$n + n^+ + M \rightarrow n_2^+ + M \tag{31}$$

Experimental data suggests that the rate of reaction is 100 times larger when the third particle is another alkali. However, for DPAL conditions the rare gas density is much greater, $> 10^6$ times larger, than the alkali density. The rate of reaction for the formation of the cesium ionic dimer in argon is very fast, $k_a = 2.4 \times 10^{-23}\,cm^6/atom - s$ (68), and is the key pathway for recombination. The rate for Eq. 31 is much faster than Eq. 29, which supports the dimer being the dominant ion specie, and $n_e \sim n_2^+$.

The density of electrons is not included in this model. It is possible that the electron temperature is much higher than the gas temperature. Free electrons can be excited collisionally or optically, coupling with the pump or lasing fields. Excited free electrons can then give this energy back to the alkali or put it into the buffer gas through quenching. The former will increase the population in the excited states, while the latter will increase the thermal energy and heat loading. If ionization only reaches 1%, the electron density will be $\sim 1 \times 10^{11}\,cm^{-3}$, which may be enough to observe the omitted adverse effects.

32

2.2.6 Rydberg states.

The high lying levels above the intermediates states are likely produced primarily by the dissociative recombination of equation 30. Curve crossings between repulsive neutral dimer states and ground state ion dimer molecules lead to the formation of excited potassium atoms during a collision with an electron. The dissociation energy of the ground molecular state of the ionic dimer, $X^2\Sigma_g^+$, is $D_0^0 = 0.76\,eV$ (22). These states are probably quenched rapidly at higher buffer gas pressures and the radiative and collisional cascade to intermediate states follows the discussion associated with Figure 7. We include theses states in the nine level model to enable comparisons with visible and near infrared fluorescence spectra from flowing, high power DPAL operation.

2.3 Rate equations

The rate equations for the nine level model are now developed and form the basis for the performance model. We use the longitudinally averaged diode pump intensity, Ω, and the intracavity laser intensity, Ψ, to characterize the optical rates, as previously developed for the three-level system (14). The rate equations for the ground, n_1, diode pumped, n_3, and upper laser level, n_2, are:

$$\frac{dn_1}{dt} = -\sigma_{13}\frac{\Omega}{h\nu_p}\left(n_1 - \frac{g_1}{g_3}n_3\right) + \sigma_{12}\frac{\Psi}{h\nu_l}(n_2 - n_1) + \gamma_2 n_2 + \gamma_3 n_3 \tag{32}$$

$$\frac{dn_2}{dt} = -\sigma_{12}\frac{\Psi}{h\nu_l}(n_2 - n_1) - \gamma_2 n_2 + \gamma_{32}\left(n_3 - n_2\frac{g_3}{g_2}e^{-\theta}\right) \tag{33}$$

$$\frac{dn_3}{dt} = \sigma_{13}\frac{\Omega}{h\nu_p}\left(n_1 - \frac{g_1}{g_3}n_3\right) - \gamma_3 n_3 - \gamma_{32}\left(n_3 - n_2\frac{g_3}{g_2}e^{-\theta}\right) \tag{34}$$

where the degeneracy ratio, $\frac{g_3}{g_1} = 2$, the fine structure mixing rates are constrained by detailed balance as in Equation 6, and the total decay rates include spontaneous

emission and quenching, $\gamma_3 = A_{31} + k_{31}^q M$ and $\gamma_2 = A_{21} + k_{21}^q M$. Laser performance is affected only by the depletion of total alkali density in the three lowest levels. The three Equations 32,33, and 34 are not linearly independent, and Equation 32 can be eliminated in favor of the conservation statement:

$$n_1 + n_2 + n_3 = N_a = N - \delta \tag{35}$$

where the total alkali density, N, has been reduced to the concentration available to the three level system, N_a, by the concentration in the higher lying and ionized states

$$\delta = (n_4 + n_5 + n_6) + n_7 + n^+ + 2n_2^+ \tag{36}$$

Source terms from quenching and radiation of the intermediates states have been omitted from Equations 32,33, and 34 and the results are limited to the modest multi-level excitation expected for DPAL conditions. We have also neglected the removal of population from the pumped and upper laser levels due to Penning ionization, pooling and wing absorption. That is, we are considering the perturbation to the three level model to be small. Figure 10 demonstrates why we can make this assumption. In this, the rate of spontaneous emission from the $4^2 P_{\frac{3}{2}}$, $n_3 A_{31}$, shown in blue is nearly an order of magnitude larger than the energy pooling rate, discussed after Equation 45, shown in orange, and the spontaneous emission rate from the intermediate states, discussed after equation 42, shown in yellow. Recall, the spin orbit rate, and therefore the lasing cycle, needs to be at least 20 times faster than the spontaneous emission rate to create an efficient laser.

For very high pump intensities where the D_2 transition is highly saturated, $\Omega >>$

34
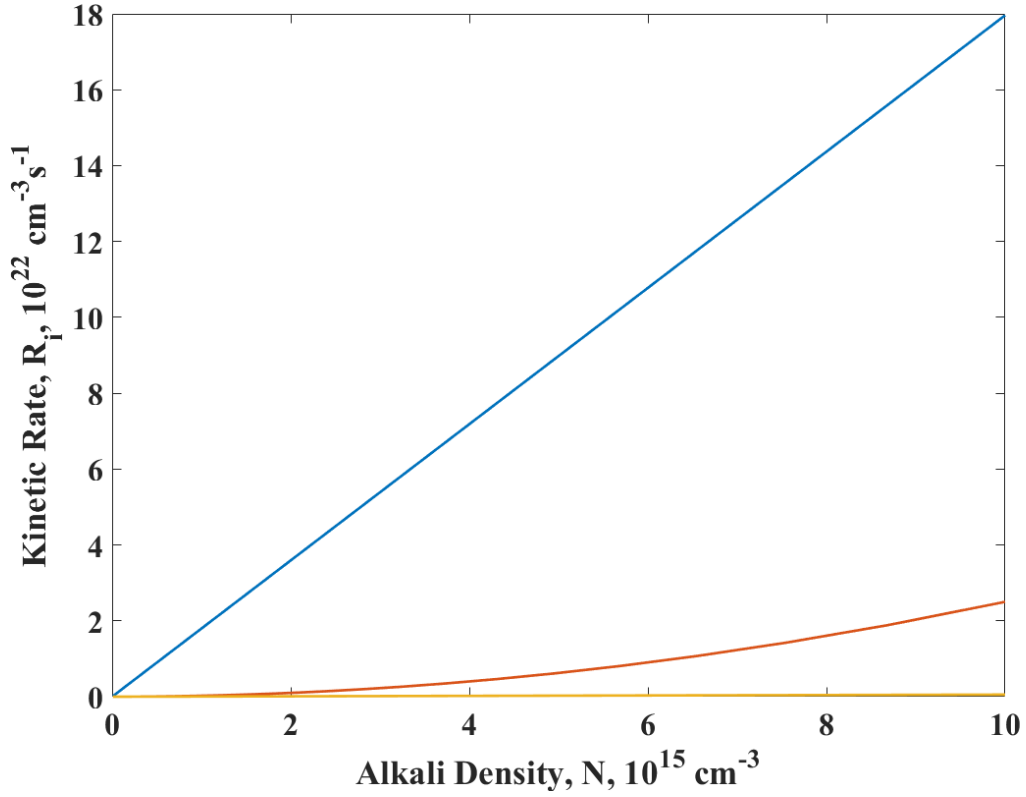
Figure 10. Kinetic rates, shown as a function of alkali density, at 1 atm buffer gas and pump intensity of $I_p = 25\,kW/cm^2$. The blue line represents spontaneous emission out of $4^2 P_{\frac{3}{2}}$, the orange is the pooling rate out of the same state, and the yellow is the total spontaneous emissions from all of the intermediate states.

$I_{sat} = \frac{A_{31}h\nu_p}{\sigma_{31}}$, the first term in equation 34 demands a bleached population difference:

$$(n_1 - n_3/2)_b = 0 \tag{37}$$

When this occurs, and in the absence of lasing $\Psi = 0$, the Q2L, the small signal solution of Table 3 is completed by requiring the equilibrium of the pumped and upper laser level:

$$\gamma_{32}(2e^{-\theta}n_2 - n_3) - \gamma_3 n_3 = 0 \tag{38}$$

When the fine structure mixing rate is very large, $\kappa = \gamma_{32}/A_{32} \rightarrow \infty$,

$$2e^{-\theta}n_2 = n_3 \tag{39}$$

and Equation 39 replaces the CW solution to Equation 33. The limiting cases of Equations 38 and 39 are not assumed when computing the lower three laser levels or the lasing intensity, but allows for a significantly easier computation of the population in the higher lying levels with and without lasing. This approximation is within 8% of the true population after only 1 atm of buffer gas is added, and is off by $< 1\%$ with 10 atm of helium.

The population in the intermediate states are defined by the rate equations:

$$\begin{aligned}
\frac{dn_4}{dt} =& (k_{2,2:4}^p n_2 n_2 + k_{2,3:4}^p n_2 n_3 + k_{3,3:4} n_3 n_3) + \frac{\sigma_L^4}{h\nu_p}(\Omega + \Psi)(n_2 + n_3) \\
& - n_4 \gamma_4 - n_4 k_4^{PI}(n_3 + n_2) - n_4 \frac{\sigma_4^{ph}}{h\nu_p}(\Omega + \Psi)
\end{aligned} \tag{40}$$

$$\begin{aligned}
\frac{dn_5}{dt} =& (k_{2,2:5}^p n_2 n_2 + k_{2,3:5}^p n_2 n_3 + k_{3,3:5} n_3 n_3) \\
& - n_5 \gamma_5 - n_5 k_5^{PI}(n_3 + n_2) - n_5 \frac{\sigma_5^{ph}}{h\nu_p}(\Omega + \Psi) + \gamma_{45}n_4 + \gamma_{65}n_6
\end{aligned} \tag{41}$$

$$\begin{aligned}
\frac{dn_6}{dt} =& (k_{2,2:6}^p n_2 n_2 + k_{2,3:6}^p n_2 n_3 + k_{3,3:6} n_3 n_3) + \frac{\sigma_L^6}{h\nu_p}(\Omega + \Psi)(n_2 + n_3) \\
& - n_6 \gamma_6 - n_6 k_6^{PI}(n_3 + n_2) - n_6 \frac{\sigma_6^{ph}}{h\nu_p}(\Omega + \Psi)
\end{aligned} \tag{42}$$

where $\gamma_i = A_i + k_i M$ and represents the depopulation methods our of the excited states; A_i is the total Einstein A-coeffcient and k_i is the total quenching rate out of excited state i. Each of these can be broken down further into final state specific rates: $A_i = \Sigma_j A_{ij}$ and $k_i = \Sigma_j k_{ij}$. The final two terms in Equation 41 represent the emission and quenching terms between the intermediate states, $\gamma_{45} = A_{45} + k_{45}^q M$ and $\gamma_{65} = A_{65} + k_{65}^q M$. This depopulation out of $4\,^2D$ and $6\,^2S$ are accounted already for

36

in γ_4 and γ_6.

Due to the small energy differences between the $4\,^2D$ and $6\,^2S$, $\Delta E \approx 50\,cm^{-1}$, we have assumed that the wing absorption rate to both states are equal. Additionally, we have assumed that the wing absorption rate due to the two fields are equal. Enhancement features in the far wings of the absorption line shape may be smaller than these splittings. However, these line shapes have not been experimentally derived or numerically calculated to the precision needed to assume a more precise value. For the sake of simplicity, we employ a common wing absorption cross-section. Future modification of the model to incorporate specific cross-sections is straightforward.

Equations 40-42 are simplified by using the quasi-two level limit (39) to make n_2 a function of n_3, for example:

$$k_4^p = k_{2,2:4}^p \frac{n_2^2}{n_3^2} + k_{2,3:4}^p \frac{n_2}{n_3} + k_{3,3:4}^p = k_{2,2:4}^p \frac{e^{2\theta}}{4} + k_{2,3:4}^p \frac{e^{\theta}}{2} + k_{3,3:4}^p \tag{43}$$

A similar technique can be used to consolidate the other Penning rates, as well as the energy pooling rate coefficients. Additionally, these three levels can be combined into a single kinetic level by summing Equations 40-42 using the grouping of:

$$n^{**} = n_4 + n_5 + n_6 \tag{44}$$

$$\frac{dn^{**}}{dt} = K^p n_3^2 + \frac{\sigma_w}{h\nu_p}(\Omega + \Psi)(n_2 + n_3) - n^{**} n_3 K^{PI} - n^{**} \frac{\sigma^{ph}}{h\nu_p}(\Omega + \Psi) - n^{**} \gamma_{**} \tag{45}$$

An equal distribution for the three states is assumed, such that, $K^p = k_4^p + k_5^p + k_6^p$, $\sigma^{ph} = \sigma_4^{ph} + \sigma_5^{ph} + \sigma_6^{ph}$, and $K^{PI} = k_4^{PI} + k_5^{PI} + k_6^{PI}$, and $\sigma_w = \sigma_L^4 + \sigma_L^6$. Validation of this assumption requires some experimental effort to investigate the true distribution amongst these states. The value $\gamma_{**} = \gamma_4 + \gamma_5 + \gamma_6 - \gamma_{45} - \gamma_{65}$ requires careful consideration, as transfer within this level does not effect the population, but will still be a source of heat loading.

37

The production of intermediates from decay of the Rydberg states or products of the ionic dimer recombination are minor paths excluded from Equations 40, 41, and 42. This approximation allows for the decoupling of the intermediate states from the higher lying levels and an equation of the total intermediate concentration directly from the populations in the three level system.

The rate equations are completed by evaluating the populations in the Rydberg (n_7) and ionized states:

$$\frac{dn_7}{dt} = k_{DR}n_2^+(n_2^+ + n^+) - \gamma_7 n_7 \tag{46}$$

$$\frac{dn_2^+}{dt} = k_a M n^+ N - k_{DR}n_2^+(n_2^+ + n^+) \tag{47}$$

$$\frac{dn^+}{dt} = k^{PI}n_3 n^{**} + \frac{\sigma^{ph}}{h\nu_p}(\Omega + \Psi)n^{**} - k_a M n^+ N \tag{48}$$

where the electron density has been replaced by the sum of the atomic and dimer ion concentrations, as required by charge neutrality, and the association rate proceeds with all alkali collisions.

The effective rate coefficients for the reactions 32-48 from the literature review are provided in Table 6. The complete nine level model is made up of Equations 33, 34, 35, 40, 41, 42, 46, 47, and 48.

Table 6. Full table of kinetic rates for potassium

Parameter	Reaction	Recommended Value	Units
A_{31}	$n_3 \rightarrow n_1 + h\nu$	3.80×10^7	s^{-1}
A_{21}	$n_2 \rightarrow n_1 + h\nu$	3.75×10^7	s^{-1}
A_4	$n_4 \rightarrow n_{i<4} + h\nu$	3.44×10^6	s^{-1}
A_5	$n_5 \rightarrow n_{i<5} + h\nu$	7.23×10^6	s^{-1}

A_6	$n_6 \to n_{i<6} + h\nu$	11.42×10^6	s^{-1}
A_7	$n_7 \to n_{i<7} + h\nu$	2.0×10^6	s^{-1}
A_{45}	$n_4 \to n_5 + h\nu$	3.43×10^6	s^{-1}
A_{65}	$n_6 \to n_5 + h\nu$	4.80×10^6	s^{-1}
σ_b^{D1}		4.87×10^{-15}	cm^2
σ_b^{D2}		3.39×10^{-15}	cm^2
k_{31}	$n_3 + M \to n_1 + M$	0	$cm^3/(atom - s)$
k_{21}	$n_2 + M \to n_1 + M$	0	$cm^3/(atom - s)$
k_{32}	$n_3 + M \to n_3 + M$	6.68×10^{-10}	$cm^3/(atom - s)$
k_{45}	$n_4 + M \to n_5 + M$	2.27×10^{-12}	$cm^3/(atom - s)$
k_{65}	$n_6 + M \to n_5 + M$	3.58×10^{-13}	$cm^3/(atom - s)$
k_4	$n_4 + M \to n_{i<4} + M$	2.29×10^{-12}	$cm^3/(atom - s)$
k_5	$n_5 + M \to n_{i<5} + M$	1.64×10^{-13}	$cm^3/(atom - s)$
k_6	$n_6 + M \to n_{i<6} + M$	8.52×10^{-13}	$cm^3/(atom - s)$
k_7	$n_7 + M \to n_{i<7} + M$	5×10^{-17}	$cm^3/(atom - s)$
$k_{2,2:4}^p$	$n_2 + n_2 \to n_4 + n_1$	3.00×10^{-11}	$cm^3/(atom - s)$
$k_{2,3:4}^p$	$n_2 + n_3 \to n_4 + n_1$	3.48×10^{-11}	$cm^3/(atom - s)$
$k_{3,3:4}^p$	$n_3 + n_3 \to n_4 + n_1$	4.03×10^{-11}	$cm^3/(atom - s)$
k_4^p	$n^* + n^* \to n_4 + n_1$	7.31×10^{-11}	$cm^3/(atom - s)$
$k_{2,2:5}^p$	$n_2 + n_2 \to n_5 + n_1$	1.71×10^{-10}	$cm^3/(atom - s)$
$k_{2,3:5}^p$	$n_2 + n_3 \to n_5 + n_1$	1.51×10^{-10}	$cm^3/(atom - s)$
$k_{3,3:5}^p$	$n_3 + n_3 \to n_5 + n_1$	1.33×10^{-10}	$cm^3/(atom - s)$
k_5^p	$n^* + n^* \to n_5 + n_1$	2.92×10^{-10}	$cm^3/(atom - s)$
$k_{2,2:6}^p$	$n_2 + n_2 \to n_6 + n_1$	2.61×10^{-11}	$cm^3/(atom - s)$
$k_{2,3:6}^p$	$n_2 + n_3 \to n_6 + n_1$	3.03×10^{-11}	$cm^3/(atom - s)$

$k_{3,3:6}^{p}$	$n_3 + n_3 \rightarrow n_6 + n_1$	3.51×10^{-11}	$cm^3/(atom-s)$
k_6^{p}	$n^* + n^* \rightarrow n_6 + n_1$	6.37×10^{-11}	$cm^3/(atom-s)$
K^{p}	$n^* + n^* \rightarrow n_{**} + n_1$	4.29×10^{-10}	$cm^3/(atom-s)$
k_4^{PI}	$n_{2,3} + n_4 \rightarrow n_1 + n^+ + e^-$	5.79×10^{-8}	$cm^3/(atom-s)$
k_5^{PI}	$n_{2,3} + n_5 \rightarrow n_1 + n^+ + e^-$	3.93×10^{-8}	$cm^3/(atom-s)$
k_6^{PI}	$n_{2,3} + n_6 \rightarrow n_1 + n^+ + e^-$	4.49×10^{-8}	$cm^3/(atom-s)$
K^{PI}	$n_{2,3} + n_{**} \rightarrow n_1 + n^+ + e^-$	1.42×10^{-7}	$1/(atom-s)$
k_{DR}	$n_2^+ + e^- \rightarrow n_1 + n_{i \neq 1}$	5.26×10^{-7}	$cm^3/(atom-s)$
k_a	$n^+ + n + M \rightarrow n_2^+ + M$	2.40×10^{-23}	$cm^6/(atom-s)$
σ_L^{4}	$n_{2,3} + h\nu_{p,l} \rightarrow n_4$	3.62×10^{-14}	cm^2
σ_L^{6}	$n_{2,3} + h\nu_{p,l} \rightarrow n_6$	4.84×10^{-14}	cm^2
α		1	
σ_4^{ph}	$n_4 + h\nu_{p,l} \rightarrow n^+ + e^-$	1.40×10^{-17}	cm^2
σ_5^{ph}	$n_5 + h\nu_{p,l} \rightarrow n^+ + e^-$	6.37×10^{-18}	cm^2
σ_6^{ph}	$n_6 + h\nu_{p,l} \rightarrow n^+ + e^-$	3.41×10^{-20}	cm^2

σph	$n^{**} + h\nu_{p,l} \rightarrow n^+ + e^-$	2.03×10^{-17}	cm^2

2.4 Steady-state and integrated rate solutions

The simplified rate equations can be solved analytically, as we assumed that the population in the higher lying states did not affect the population in the three laser levels. The steady state solutions for the lowest three states and the intracavity laser intensity are:

$$n_1 = \frac{(\frac{\sigma_{13}\Omega}{2h\nu_p} + \gamma_3)n_3 + (\frac{\sigma_{12}\Psi}{h\nu_l} + \gamma_2)n_2}{\frac{\sigma_{13}\Psi}{h\nu_p} + \frac{\sigma_{12}\Psi}{h\nu_l}} \tag{49}$$

$$n_2 = \frac{\frac{\sigma_{12}\Psi}{h\nu_l}n_1 + \gamma_{32}n_3}{\frac{\sigma_{12}\Psi}{h\nu_l} + \gamma_2 + 2\gamma_{32}e^{-\theta}} \tag{50}$$

$$n_3 = \frac{2\gamma_{32}e^{-\theta}n_2 + \frac{\sigma_{13}\Omega}{2h\nu_p}n_1}{\frac{\sigma_{13}\Omega}{h\nu_p} + \gamma_{32}e^{-\theta} + \gamma_3} \tag{51}$$

$$\Psi = \eta_0 I_{sat}(\alpha\frac{\Omega}{Isat} - B) \tag{52}$$

where

$$\alpha = \frac{(\frac{\sigma_{21}n}{g_{th}})(2\kappa(1 - e^{-\theta})(\frac{\gamma_{31}}{\gamma_{21}}) - 1) - (3 + 2(1 + 3e^{-\theta})\kappa(\frac{\gamma_{31}}{\gamma_{21}}))}{2[(1 + \kappa(1 - e^{-\theta})) + 2\frac{\Omega}{I_{sat}}]} \tag{53}$$

$$B = (1 + \frac{\sigma_{21}n}{g_{th}})\frac{1 + \kappa(1 + 2e^{-\theta}\frac{\gamma_{31}}{\gamma_{21}})}{\gamma_{21}}))2[(1 + \kappa(1 - e^{-\theta})) + 2\frac{\Omega}{I_{sat}}] \tag{54}$$

$$I_{sat} = \frac{h\nu_p\gamma_3 1}{\sigma_{31}} \tag{55}$$

These equations can be solve simultaneously, to get the decoupled solutions as a function of Ω. The pump intensity needed to create the needed value for Ω is:

$$I_p = \Omega\frac{\sigma_{31}(n_3 - 2n_1)l_g}{e^{\sigma_{31}(n_3-2n_1)2l_g} - 1} \tag{56}$$

41

In practice, I_p is known and Ω is to be computed, but the model is more easily run in reverse: finding the roots of Equations 49-52 and then using Equation 56 to solve for the pump intensity required. The results of this are presented by Hager et al, in (14; 15).

The rest of the energy levels have similar steady state answers:

$$n_4 = \frac{k_4^p * n_3^2 + \frac{\sigma_L^4}{h\nu_p}(\Omega + \Psi)(n_2 + n_3)}{k_4^{PI} n_3 + \frac{\sigma_4^{ph}}{h\nu_p}(\Omega + \Psi) + \gamma_4} \tag{57}$$

$$n_6 = \frac{k_6^p * n_3^2 + \frac{\sigma_L^6}{h\nu_p}(\Omega + \Psi)(n_2 + n_3)}{k_6^{PI} n_3 + \frac{\sigma_6^{ph}}{h\nu_p}(\Omega + \Psi) + \gamma_6} \tag{58}$$

$$n_5 = \frac{k_5^p * n_3^2 + \gamma_{45} n_4 + \gamma_{65} n_6}{k_6^{PI} n_3 + \frac{\sigma_6^{ph}}{h\nu_p}(\Omega + \Psi) + \gamma_6} \tag{59}$$

$$n^+ = \frac{k^{PI}(n_2 + n_3)n^{**} + \frac{\sigma^{ph}}{h\nu_p}(\Omega + \Psi)n^{**}}{k_a M N} \tag{60}$$

$$n_2^+ = \sqrt{\frac{k_a M N n^+}{k_{DR}}} \tag{61}$$

$$n_7 = \frac{k_{DR} n_2^+ (n_2^+ + n^+)}{\gamma_7} \tag{62}$$

Due to the rapid nature of three body association, Equation 71 has assumed $n_2^+ >> n^+$ and been simplified accordingly.

2.5 Model predictions

Figure 11 shows the ratio of δ (first defined in Equation 36) to the total alkali density as a function of total alkali density at many different buffer gas pressures, in the CW regime using the baseline rate parameters of Table 6 and $\Omega = 19.3\,kW/cm^2$. At low alkali density, when photo-excitation dominates, δ grows slower than total density,

and the curves trend downward. Because photo-excitation processes dominate, ion density is both created and destroyed as a linear function of total alkali density, and additional alkali does not create more ions. Because dimer growth depends directly on the ion density, the dimer grows sub-linearly with respect to N and δ grows slower than total density. However, at higher density, when the rate of collisional processes grow, ion creation goes like the square of alkali density and adding alkali causes an increase in ions, resulting in δ growth that is super-linear with N. In general, adding helium causes the delta fraction to decrease and delays the take over of the collisional mechanisms. Most DPAL systems operate with $N < 10^{14}\,cm^{-3}$, and the population in higher lying states is less than 6% of the total. The perturbation approach to the three level system appears appropriate for normal operating conditions.

Figure 12 demonstrates this δ fraction as a function of pump intensity at a fixed helium pressure of 1 atm. At high N, the ion concentration is dominated by Penning ionization, and adding pump intensity does little to the excited population. When density is low, $N <\sim 10^{13}$, though, the excitation processes are dominated by photo effects and population in the higher lying states rises dramatically. Current diode technology limits pump intensity to $< 50\,kW/cm^2$ and again, the fraction of population in the higher lying states is limited to $\sim 7\%$.

At high alkali densities and low pump intensity the delta fraction in Figure 12 is constant with respect to pump intensity. This is due to energy pooling acting as the dominant mechanism. As pump intensity increases, though, photo-excitation processes grow and begin to take over as the largest contributor. Figure 13 demonstrates at what alkali densities and pump intensities each of the two excitation mechanisms are dominant in producing n_6 density, at different buffer gas pressures. Each line represents when the energy pooling rate and the photon excitation rate are equal; at 760 Torr (blue), 1,520 Torr, (orange), and 3,800 Torr (yellow). As alkali density

43
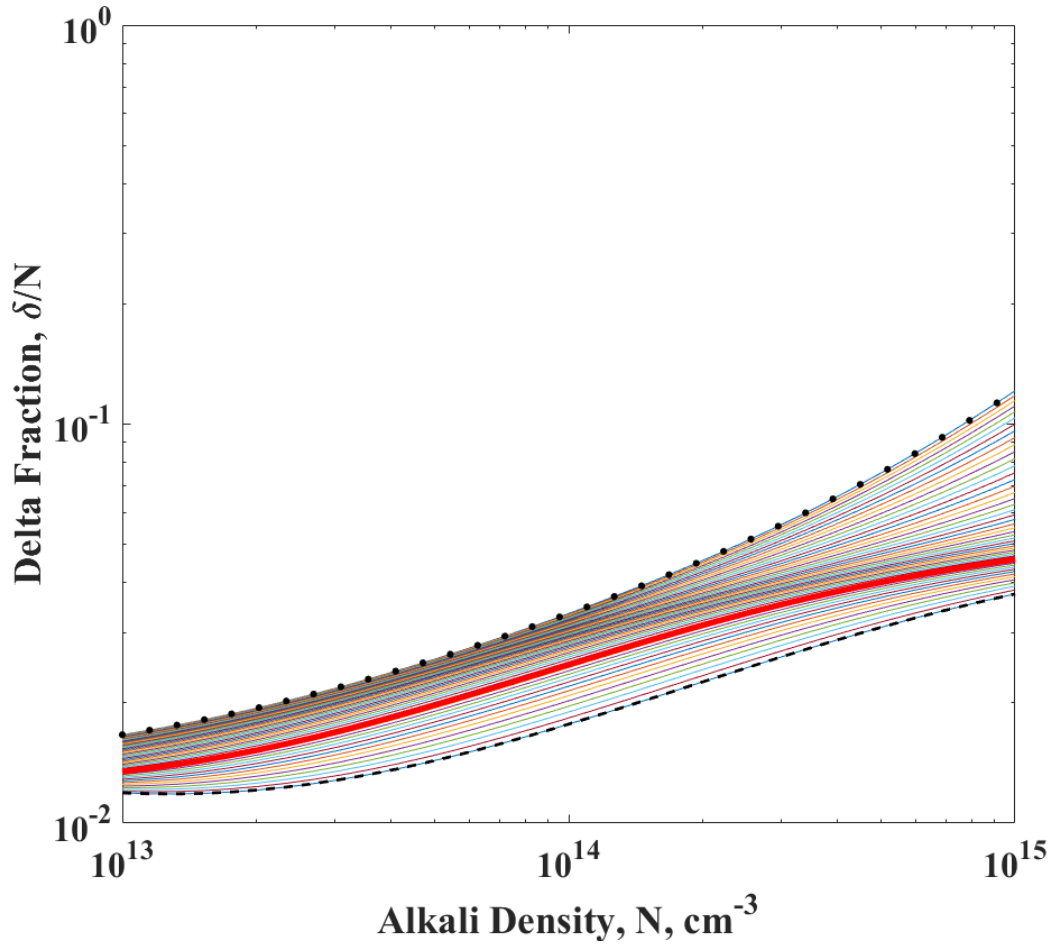
Figure 11. Fraction of population in higher lying states as a function of alkali density for a series of helium densities. The dashed lower line represents the curve at a helium pressure of 4.82 Torr and the dotted upper line represents helium pressure of $4,820$ Torr. The lines in between represent helium density increasing by a factor of 1.15, with the bold red line corresponding to 760 Torr.

rises, more pump intensity is required to match the two rates, however increasing the buffer gas pressure decreases the pump required for all alkali densities. The slope of these lines are the ratio of the excitation cross section and the pooling rate coefficient, going like $\propto k_6^p/\sigma_L^6$.

As mentioned above, the quenching rates out of the intermediate states have not been experimentally observed. Figure 14 demonstrates the effect changing these rates has on the model. It shows the change in total δ if k_4 (blue), k_5 (orange),

44
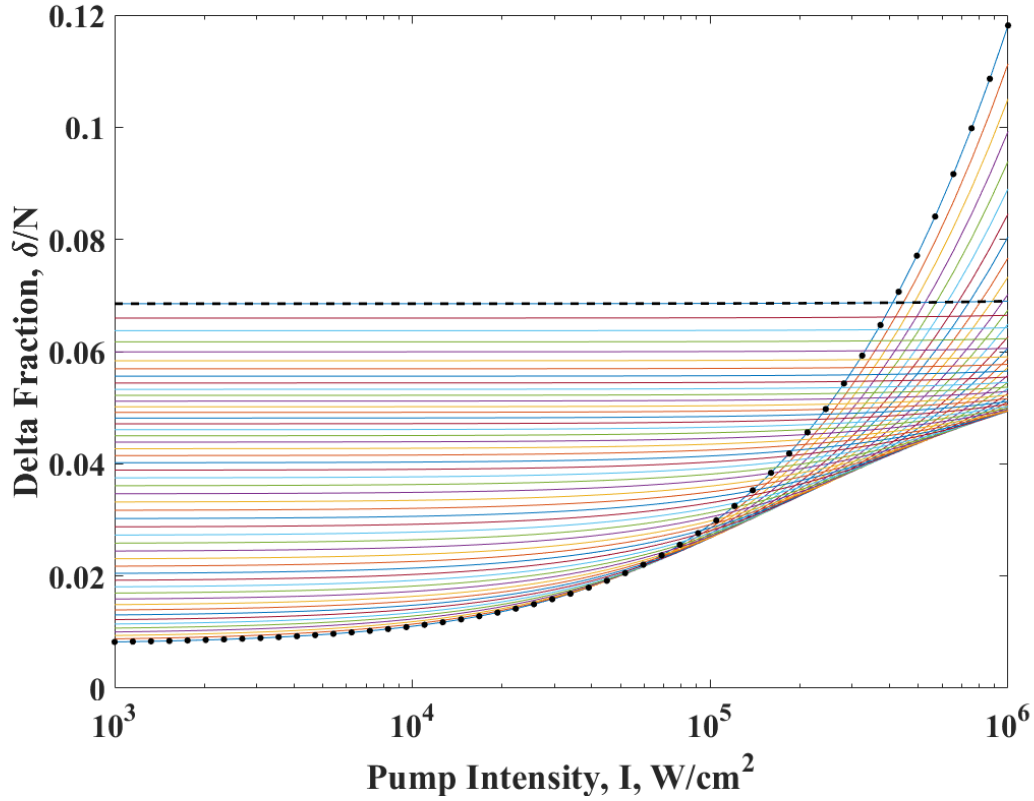
Figure 12. Delta fraction as a function of pump intensity and alkali density. The dotted line here represents an alkali density of $1 \times 10^{13} \, cm^{-3}$ and the dashed has an alkali of $1 \times 10^{16} \, cm^{-3}$. The lines in between represent alkali density increasing by a factor of 20. At low N, photo processes dominate and δ grows rapidly with pump intensity.

and k_6 (yellow) is changed. This is shown at the base line conditions from Table 3 at $I = 10 \, kW/cm^2$. Decreasing any of the quenching rates increases δ, but only increasing k_5 causes a noticeable decrease. Much of the quenching from n_4 and n_6 terminates into n_5, so it does not decrease the total δ, just the composition. Increasing the rate out of n_5, though, sends population back into the lasing levels.

Using the model created by Hager et. al, a prediction of laser intensity can be calculated as a function of alkali density, for a given laser design. Fig. 15 displays the output laser intensity of a longitudinally pumped, static, CW DPAL, with geometry as described in (14), with a gain length of $l_g = 10 \, cm$ and a threshold gain of $g_{th} = 0.086 cm^{-1}$, shown as the solid line. The pump intensity is set to

45
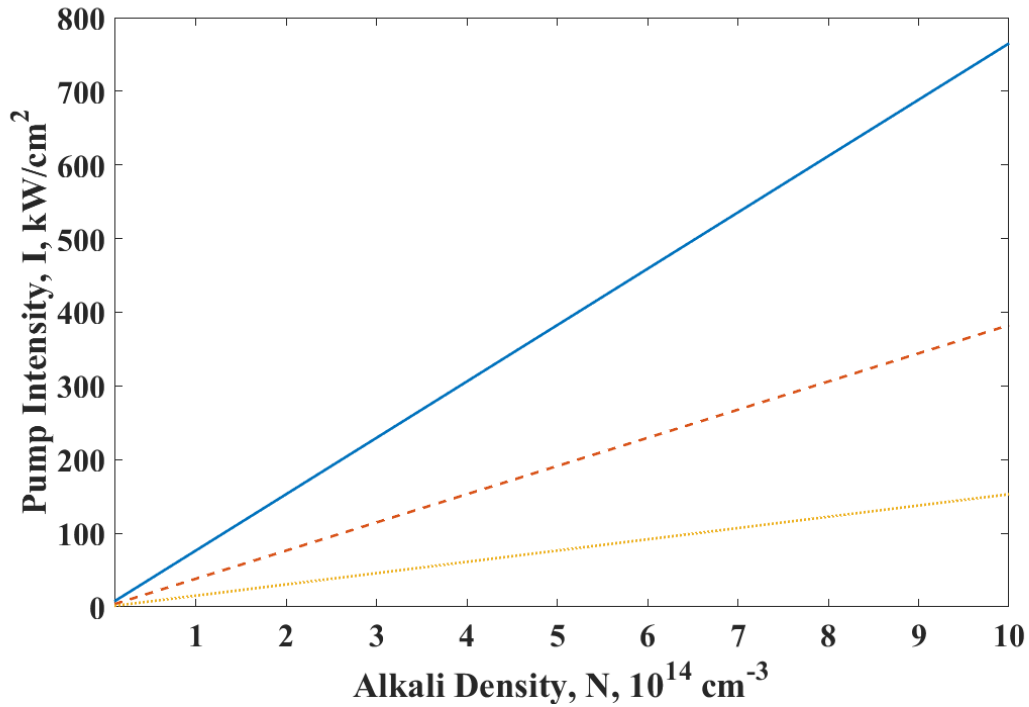
Figure 13. Pump intensity required to match the wing absorption rate to the energy pooling rate, as a function on number density, at $P = 760$ (blue), 1,520 (orange $--$), and 3,800 (yellow •) Torr.

$I_p = 10 \, kW/cm^2$ at a buffer gas pressure of 1 atm of pure helium, at $T = 460 \, K$ setting $\kappa = 279.8$. For $N < 3 \times 10^{12} \, cm^{-3}$, bleached gain is less than cavity losses, and no lasing is achieved. There is an optimum alkali density at $n = 1.66 \times 10^{13} \, cm^{-3}$ after which the lasing decreases, as absorption in the cell becomes too large. The alkali density available to the lasing process including multi-level kinetics is reduced to $N_a = N - \delta$. In Figure 15, $\delta/N = 0.0099$, and the intensity decreases by $1.73 \, W/cm^2$ or $< 0.03\%$. If the fraction of the population in higher lying states were to increase (e.g. by increased wing absorption) the power loss also increases. The loss ratio is defined as 1-(output power with multilevel kinetics / without multi-level kinetics), is illustrated by the dotted curve in Figure 15. For example, if $\delta/N = 0.2$ at the peak output power, the loss ratio would be 0.235.

The scaling of laser output intensity with pump intensity for the base line con-

46

www.manaraa.com
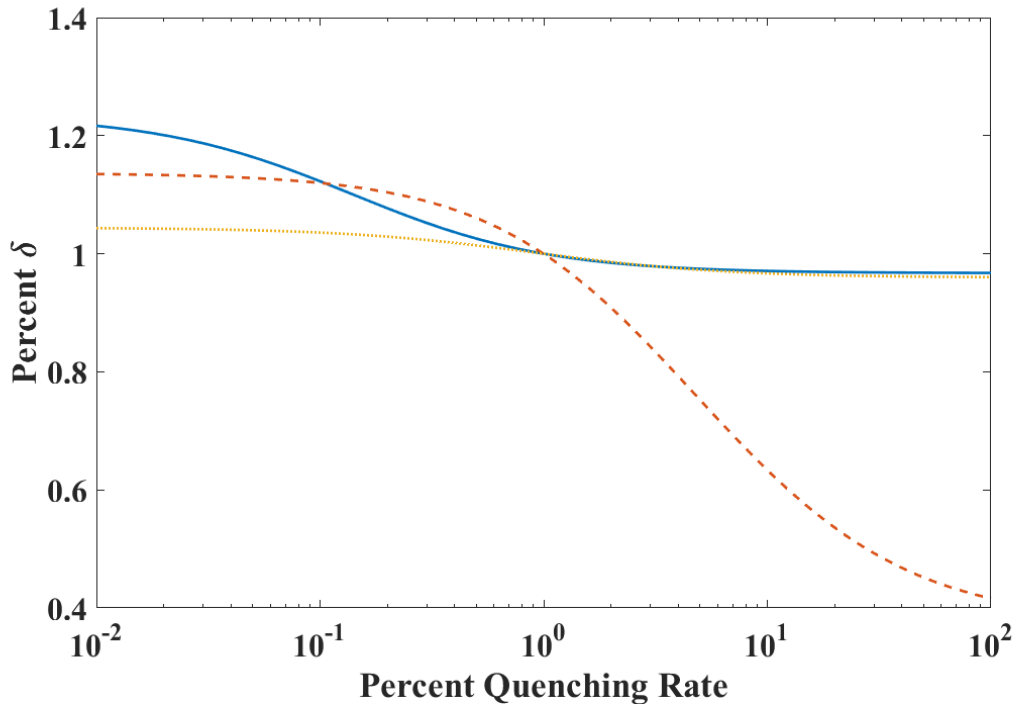
Figure 14. The change in δ is plotted as a function of the change in the quenching rates. Modulating the k_4 is in blue, k_5 is in orange $(--)$, and k_6 is in yellow $(\bullet)$.

ditions is illustrated in Figure 16, similar to the cases provided in Figure 4. The bleached limit occurs near $I_p = 20 \, kW/cm^2$, as the fine structure mixing rate limits output power and the system becomes bottle necked. At higher pump intensities, the production of higher lying states increases, δ/N increases, and output power declines. At $100 \, kW/cm^2$ the degradation is significant with a loss factor of $\sim 5\%$. The roll off of power exhibited at very high pump powers may be similar to that shown experimentally by Zhdanov *et. al* in (7), but occurring at much higher intensities here. The rolloff exhibited at lower powers is likely not do to multi-level kinetics, but can be caused by any effect that drives the apparent alkali density down; diffusion due to temperature gradients in the alkali can cause δ to increase.

These figures illustrate the limited effect ionization has on laser power. The density of alkali available to lase decreases a small amount and that can have adverse effects

47
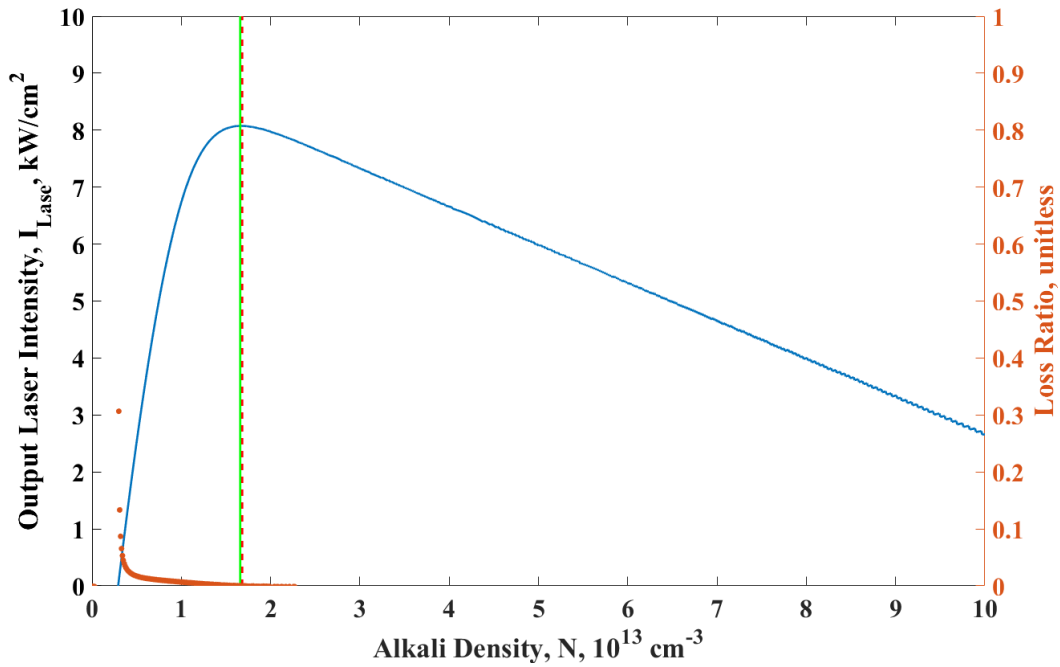
Figure 15. Three level laser performance as a function of alkali density, at $10\,kW/cm^2$ pump intensity and 1 atm helium buffer gas. The solid vertical line represents the number density in which the intensity out is maximized and the dashed vertical line represents the alkali density available to lase if set to the maximum total alkali density and higher level kinetics are included. The magnitude of the degradation is shown with the loss ratio (•).

on laser power. However this loss can be recovered by simply adding more alkali to the cell, to compensate for these deleterious processes. Due to the imperfect measurement techniques of alkali density, the δ fraction may be lower than the error of the density measurement.

As mentioned above, one of the primary assumptions required to create this model was that δ is a small perturbation of the lower three levels, only effecting the total population available to lase, such that the true alkali density is $N_a = N - \delta$. Using this, the model should converge on a value of δ when iterated. To do this, δ is computed using the total alkali density. The alkali density is reduced by this value and a new δ is recomputed. Figure 17 shows that it does converge. After the first iteration δ is varied by $< 2.1\%$ and only $< 0.03\%$ after the second iteration.
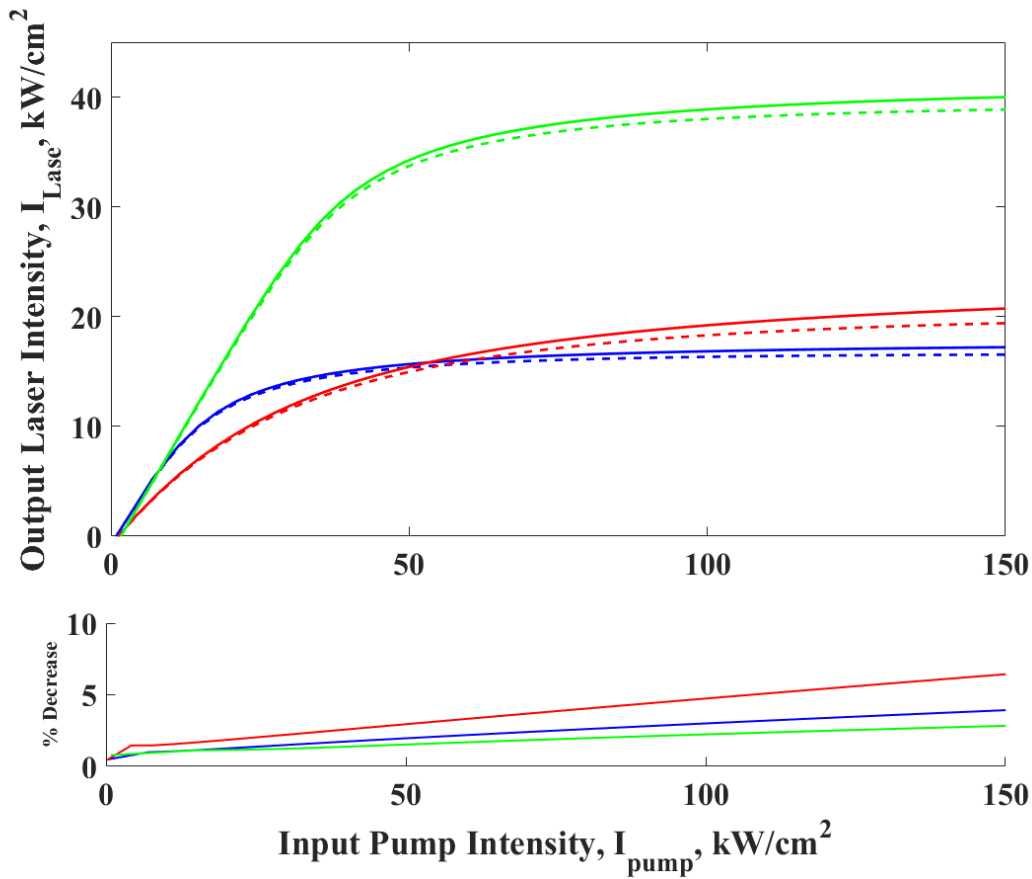
Figure 16. Laser intensity as a function of pump intensity, with and without multi-level kinetics (−−). The cases presented here are the same as in fig:PsiOmega. The blue is consistent with the parameters in Table 3, the alkali density is doubled for the green and the helium density is doubled for the red.

2.6 Conclusion

With the goal to resolve the controversy surrounding multi-level kinetics in a DPAL, a thorough literature review on mechanisms relevant to DPAL ionization has been conducted and the best rates of each mechanism is given. New scaling laws were developed to appropriately determine some rate constants, specifically, energy pooling, broadening of higher transitions, and Penning ionization. Some of these rates are well established in the literature, such as the spin-orbit mixing rates and the absorption cross section of the pump and lasing transitions; others were found measured

49
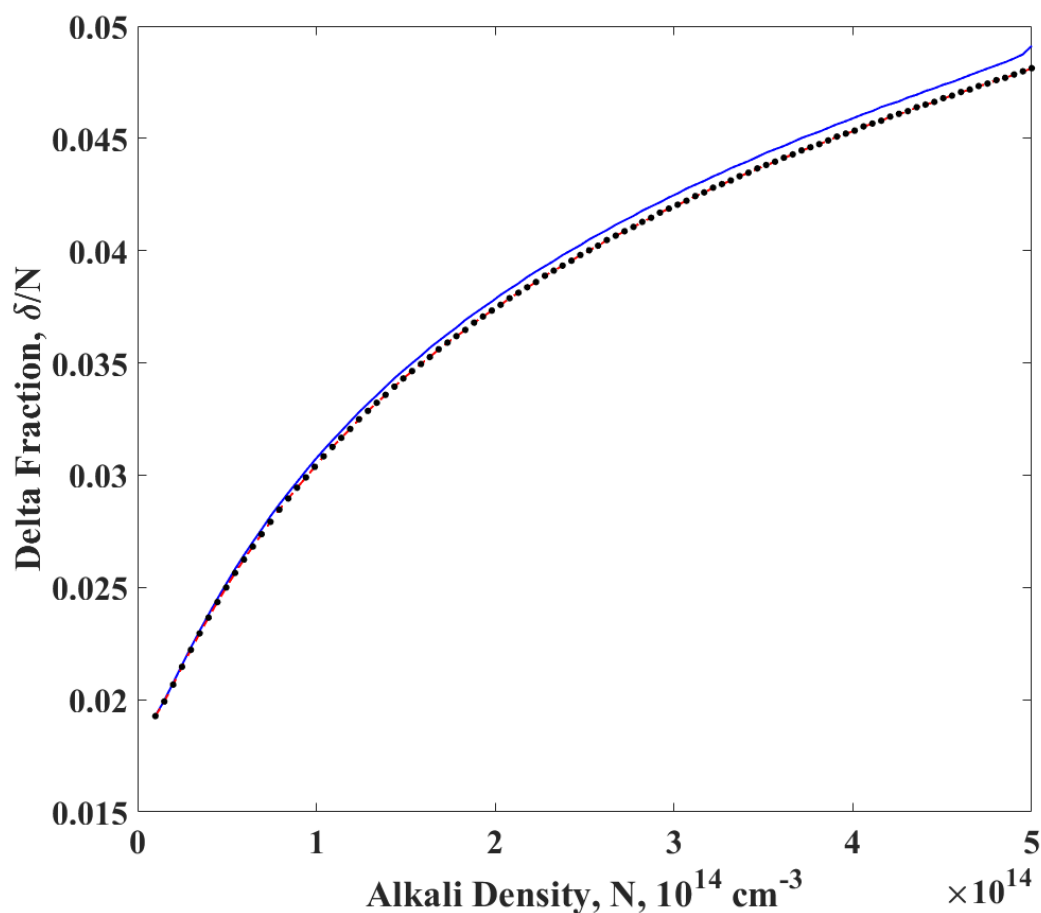
Figure 17. The values of δ as a function of alkali density at $P = 250$ **Torr is iterated to assure convergence. The initial value is the blue solid line, the first iteration is the red dashes ($--$) and the second iteration is shown as black filled circles ($\bullet$).**

for potassium and are likely accurate, such as energy pooling and photoionization. Rates for Penning ionization, dimer formation and dissociative recombination have only been determined for other alkali metals, so the true value may be different than the one presented here. Lastly, quenching rates of the intermediates and absorption line shapes for high transitions have not been measured at all and require significant future study.

A new nine level kinetic model has been produced adopting the most important mechanisms found in the literature. Using existing laser performance data as a guide,

appropriate approximations allow for this model to be analytic and predict the population that has escape the lasing process as a function of laser system parameters. Population is excited to the intermediate states by both energy pooling and photo-excitation into the far wings of the absorption profile. The intermediates are then ionized mostly through Penning and photo-ionization. Atomic ions quickly undergo a three body collision that forms the ionic dimer, and dissociative recombination populates the Rydberg states. The Rydberg states radiate and quench in a cascading fashion back to the ground state.

The model predicts small values for δ/N, between $1 - 12\%$ depending on laser parameters, and recommends methods to mitigate any adverse effects on laser power. The ionic dimer is a major component of δ, when the suggested rates are used, resulting in the model presented here. If not for this large dimer population, a simpler four level model would be possible. However, the added complexity gives use to side fluorescence measurements taken from DPAL systems.

III. Kinetics of higher lying states in a high power, transverse flow diode pumped potassium vapor laser

Fluorescence emitted by a high power, transverse flow potassium DPAL was collected to characterize the highly excited state population at total alkali densities of $N = 0.63 - 1.87 \times 10^{14}\,cm^{-3}$ and buffer gas pressures of $P = 250 - 1200$ Torr. The population in these states was found to be less than 5% for all cases. The observations are compared to a nine level kinetic model and a new rate package is recommended to accurately match the observed densities.

3.1   Introduction

Dramatic progress in power scaling of Diode Pumped Alkali Lasers (DPALs) has been achieved with 1-2 kW systems demonstrated in potassium (18) and cesium (5) and recently ~ 30 kW for Rb (6). Ideal, quasi two-level performance is achieved when the cycle rate is limited only by diode pump intensity. For example, a pulsed potassium laser has been demonstrated with the time scale for fine structure mixing of 70 ps (9). The influence of higher lying states and ionization on DPAL power efficiency and beam quality is a current topic of some controversy. Some studies indicate that the rate of photoionization is significant in situations with high buffer gas pressures (10; 13). However, pulsed experiments have pumped 30 times higher than threshold with no significant loss in efficiency (69).

Several previous models to describe ionization in DPALs have been developed (10; 11; 12). For example a kinetic mechanism and fluid dynamics model to investigate static and flowing cesium DPAL, focused on the role of hydrocarbons in the lasing process (12). Oliker et. al also produced a static model for a cesium DPAL that incorporates kinetic and fluid dynamics (11). This three dimensional model included a look at thermal aberrations but neglects dissociative recombination. Knize

suggests ionization rates may be catastrophically high in all alkalies but does not fully evaluate restorative processes like recombination (10). We recently developed a kinetic mechanism for the population in the excited states (70). This nine level model includes the 3 primary lasing levels–$4^2 S_{\frac{1}{2}}$, $4^2 P_{\frac{3}{2}}$ and $4^2 P_{\frac{1}{2}}$ in potassium–3 intermediate states–$6^2 S, 5^2 P$ and $4^2 D$– the Rydberg states, the atomic ion, K^+ and the ionic dimer, K_2^+. This model suggests that multi-level kinetics do not significantly reduce laser performance for typical operating conditions if the alkali density is properly controlled. However, experiments to benchmark these models and specify key rates are lacking. In particular, the dominant mechanism for populating the intermediate states, the collisional de-excitation rates of the intermediate and Rydberg states and ion recombination rates require further study.

Prior alkali laser fluorescence studies were primarily limited to energy pooling and spin orbit kinetics at low pressure and pump intensity (42; 43; 58). Characteristic alkali spectra has been collected mostly with multi-photon excitation, where strong blue lines (in addition to the near IR lines) were observed (71; 72). Observations of emission from higher lying states under DPAL conditions are rather limited. Zhandov et. al observed side flourescense from a static DPAL and identified four sets of atomic lines, however effects of alkali density and helium pressure were unreported (16).

In the present study we compare the nine level model derived in (70) with observations from a high power ($\sim$kW), transverse flow potassium laser. Emission from ~ 30 atomic potassium states with principal quantum number as high as $n = 11$ are observed for pump intensities of $> 10 \, kW/cm^2$. Quenching rates for the $4\,^2D$ and $6\,^2S$ intermediates are determined. A comparison of the data and model indicate additional rates of population and destruction of the excited states.

53

3.2   Experimental setup

The flowing K DPAL experimental apparatus is shown in Figure 18. The laser system is designed with a transverse diode pump laser and transverse gas flow. Six DILAS diode 425 W modules pump the alkali volume, each module consists of 8 micro channel cooled bars coupled to a single 600 μm core fiber with $NA = 0.22$. These are temperature tuned with a volume Bragg grating (VBG) with a bandwidth of $51.6 - 56.3$ pm (26.4-28.8 GHz) as current increases, $i = 40 - 96$ A. The combined spectral bandwidth at 3 kW is $58\, pm$ (29.7 GHz) FWHM (73). For this study, the diodes were run at $i = 54.6\, A$, with an output power of $1.2\, kW$. The diode current was maintained within $\pm .05\, A$, to assure laser power variation of $< 10\, W$. Diode power transmitted through the cell was measured using an Ophir 5000W-SH power meter placed ~ 15 cm behind the cell.
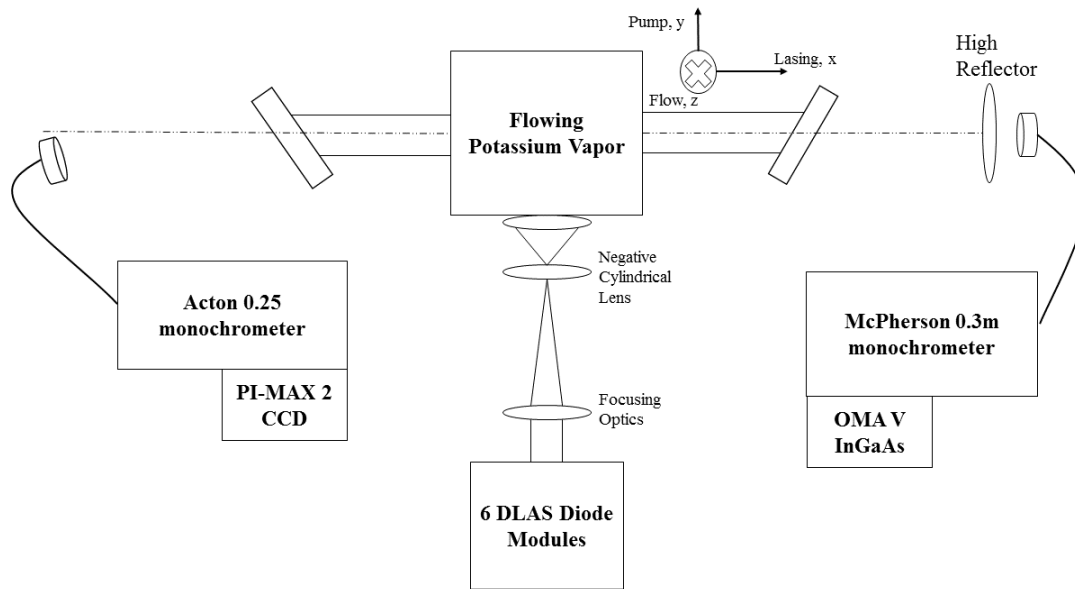
Figure 18. A block diagram of the laser setup used in this experiment.

Two Thorlabs AL100200-B aspheric lenses (10 cm diameter, 20 cm focal length, N-BK7 glass) reimage the fiber bundle onto a LEO negative cylindrical lens (10 cm

by 8 cm, -15 cm focal length, UV fused silica) to spread the beam and match the width of the alkali flow. The irradiance at the focus is $I = 37.4 \, kW/cm^2$, or $\sim 1,550$ times the saturation intensity.

The alkali chamber is described in detail in reference (18). The stainless steel chamber houses an alkali flow, the potassium density in the chamber was held between $N = 0.63 - 1.87 \times 10^{14} \, cm^{-3}$ and monitored as described below. The melt pool temperature was $T = 473 - 533 \, K$, indicating $12 - 42\%$ saturation. Two Machined Glass Specialists, INC. TSC-3 substrate windows, etched with a random anti-reflection coating, are installed in the pump direction and two similar uncoated windows are installed at Brewster's angle in the laser direction to minimize reflections and parasitic lasing. A secondary helium gas flow is circulated across these windows to protect them from contamination. Gaseous helium, type 1 grade A, provided by Air Products and Chemicals, Inc. is optionally mixed with Airgas UHP GR 4.0 methane and is streamed over the alkali melt pool, consisting of Sigma-Aldrich potassium–ingot, 99.95% metals basis, and into the cell. The primary contaminants are rubidium (143 ppm), sodium (48 ppm), and titanium (48 ppm). The melt pool temperature, as well as the entire cell temperature, is regulated by Watlow EZ-ZONE heat controllers. Temperature was monitored at twelve different locations with the key measurements before and after the potassium bed and in the laser cavity with Omega TMQSS-125G-6 K-type and T-type thermocouples.

The vacuum system supported helium flow rates of up to 250 SLM, but these tests employed 50 SLM using an MDC inline valve. The flow speeds correspond to residence times of $0.022 - 0.104 \, s$ over the melt pool. Two Honeywell 060-J033-01ZA transducers measure the pressure immediately before and after the laser chamber. Two Stellar Technology ST1550-1000A-107 sensors are used to measure the pressures in the flow of the two buffer gases, helium and methane, and Stellar Technology ST1550-100A-

107 sensor measured the pressure over the potassium bed. The pressure traducers are rated to 6.8 atm (5,170 Torr), but the total pressure was maintained between $250 - 1200$ Torr for the entire study.

Optical diagnostics included two spectrometers for visible and near infrared florescence, power meters, and laser absorbance for potassium density. The side fluorescence was collected, just off of the lasing axis. One LG-455-020-3 fiber bundle in the forward lasing direction, passes the visible spectrum using a ThorLabs F810SMA-780 output coupler and a 750 nm short-pass filter, and entering a Acton SpectraPro-275 monochrometer with a Princeton Instruments, PI-MAX 2 CCD. This visible spectrometer is fitted with two 1,200 gr/mm gratings, with a blaze at 750 nm or 300 nm. The spectral resolution was typically 0.036 nm. The bandwidth of ~ 35 nm required 13 spectra to cover the full range of 381-715 nm. Spectra were recorded with an integration time of 1 sec, and summed in the vertical slit direction. The smallest signal to baseline ratio was 3, while the largest was over 10000. An additional Thorlabs BFL200LS02 fiber bundle is placed on the backwards lasing axis, behind the LEO RX-700-900-B-MPC high reflector mirror, to collect the near IR spectrum. A Thorlabs F810SMA-1310 fiber bundle, transmitted the emission to a 218 McPhearson 0.3 meter scanning monochrometer (600 gr/mm, 1.25 um blaze grating) and Roper Scientific, OMA V InGaAs array. The spectral resolution for this was 0.1 nm and the band width was ~ 100 nm, so 5 spectra were required for the range of $900 - 1,335$ nm.

Detector response was characterized in two steps, $D = D_\lambda D_t$, as the product of relative spectral response D_λ and absolute D_t response. The relative spectral response of both spectrometers was calibrated with an Oriel Instruments Quartz Halogen lamp, and peaked at 900 nm. The absolute response of the visible monochromator was estimated using three approaches. First, an estimation using radiometry, using the

collection solid angle of 0.057 rad, and a viewing volume defined by the diode pump beam at the focus of 0.24 cm^3, yields a detectivity value of $D_t = 0.0011$. A second estimate of absolute detectivity, D_t, can be obtained from the observed D_2 line. The population in the $4\,^2P_{\frac{3}{2}}$ state, n_3, is bleached by the intense diode pump, so that $n_3/N = 0.47$ (14). However, the peak of the D_2 line is obscured by scattered diode radiation. The far wing, detuned by 900-1,230 cm^{-1} from line center is observable. While the line shape is non-Lorentzian at high pressure, the numerical predictions are available (51). The predictions are sensitive to the accuracy of the surface calculations (74). Unfortunately, the detectivity computed in this manner depends on alkali density, $D_t = 0.004 - 0.018$ (70). Finally, the absolute detectivity could be estimated by the emission from the $4\,^2D$ state, using the kinetic model for populations discussed below. For a predicted $^2D_{\frac{5}{2},\frac{3}{2}}$ density of $4.47 \times 10^{10} cm^{-3}$ at $N = 1.87 \times 10^{14}\, cm^{-3}$ and pure helium at 250 Torr we obtain $D_t = 0.0043$. These three methods provide a range of detectivites of $D_t = 0.11 - 1.8 \times 10^{-2}$, and we use $D_t = 0.43 \times 10^{-2}$ in reporting photon densities.

Potassium density was measured by tunable diode laser spectroscopy on the $4\,^2S_{\frac{1}{2}} - 5\,^2P_{\frac{3}{2}}$ transition at 404.41 nm. A 45 mW Toptica Photonics tunable diode laser with 100 kHz line width was transmitted along the diode pump axis, $l = 2.53$ cm, prior to each experiment. The laser is sent through a waveplate, then split into four beams; one beam through an etalon, one through a low pressure reference cell held at 393 K, one through the laser cavity, and one through free space to serve as I_0. The beam that traverses the etalon is monitored by a Thorlabs PDA100A Si amplified detector, while the other three use New Focus 2032 large-area UV photoreceivers.

These tests were completed in March 2017. Over 50 full bandwidth spectra were collected with potassium bed temperatures between $473 - 533\,K$, corresponding to potassium densities $N = 0.65 - 1.87 \times 10^{14}\, cm^{-3}$ in the cell. Buffer pressure was

varied from 250 to 1200 Torr. Most of the tests were performed in pure helium, but a few were collected with methane added, 7.9 and 16.13 % by mass. All of these tests were collected at a single pump power, 1.23 kW, in the absence of lasing. The output coupler was removed from the laser setup and transmitted power was monitored.

3.3 Results

3.3.1 Potassium Density Measurements.

Characterization of the potassium density delivered to the gain cell is critical to the kinetic conditions for these experiments. Typically, the fraction of the saturated vapor pressure (75) realized in the flowing system is $10-50\%$, and is measured using the tunable blue absorption diagnostic, with a typical absorption spectrum illustrated in Figure 19.

A Lorenztian fit is also shown in Figure 19 and is used to determine the peak absorbance and potassium density. This diagnostic was primarily designed for moderate temperatures and high pressure. The Lorentzian width of the K $4\,{}^2S_{\frac{1}{2}} - 5\,{}^2P_{\frac{3}{2}}$ line centered at $\lambda = 404.4$ nm was fit to $8.5 \pm 0.1\,GHz$. The integrated absorbance of $3.653 \pm 0.005 \times 10^{10}$ Hz yields a K density of $N = 6.352 \pm 0.009 \times 10^{13}\,cm^{-3}$, using a integrated cross section of $\int \sigma = 7.54 \times 10^{-5}\,cm^2 - Hz$. This cross section has been evaluated using values from the NIST database (3).

TDLAS observations are compared with the vapor pressure in Figure 20. The degree of saturation decreases from $41.8 - 5.4\%$ as the melt pool temperature increases from $473 - 513$ K, so that the potassium density is rather constant, $N = 0.64 - 0.96 \times 10^{14}\,cm^{-3}$. The density at the highest tested temperature, $T = 533$ K is considerably higher, $N = 1.87 \pm 0.17 \times 10^{14}\,cm^{-3}$, 12.2% of the saturated vapor pressure.

To confirm the K density measurement, the transmitted diode pump power was measured as shown in Figure 21. The transmitted power declines slightly with helium
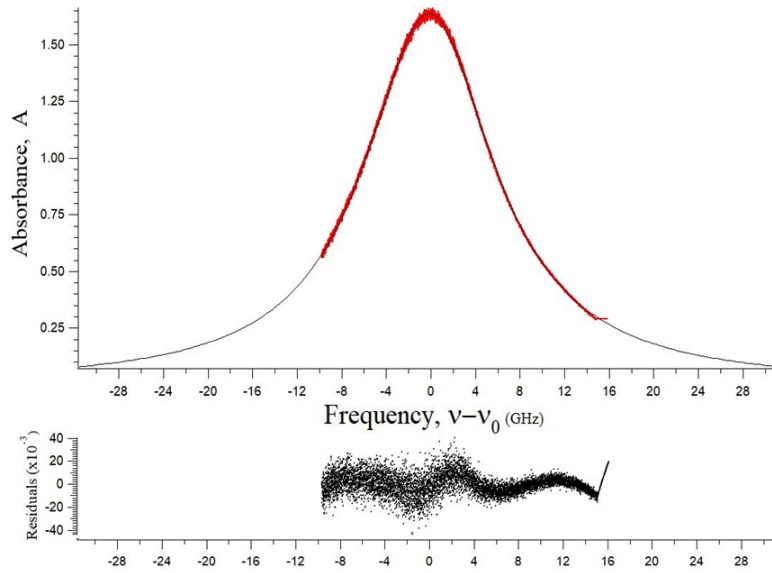
Figure 19. An example K $4\,{}^2S_{\frac{1}{2}} - 5\,{}^2P_{\frac{3}{2}}$ **diagnostic with K density of** $N = 0.65 \times 10^{14}\,cm^{-3}$ **at bed temperature of** $T = 473$ **K: red points represent the observed spectra, and the black curve is the Lorentzian fit.**

pressure primarily due to improved matching between the absorption line shape and the diode spectral distribution. The transmitted power is weakly dependent on melt pool temperature for $T = 473 - 523$ K, consistent with the TDLAS observations. At 533 K, the transmitted power decreases from 900 W to 400 W, as expected for the higher potassium density. The transmitted power has been predicted using a three-level DPAL model (14). The potassium densities required to match the model and observed powers are compared with the TDLAS observations in Figure 20. The TDLAS measurements are preferred, as the DPAL model assumes an unfocused pump beam, clearly violated in the present apparatus.

The number density depends on helium pressure as shown in Figure 22. Number density in the gain path is influenced by both flow transit time over the potassium bed and condensation of the alkali between the bed and the gain path. Helium pressure is regulated in the cell by varying flow speed, which effects both of these factors. Slower

59
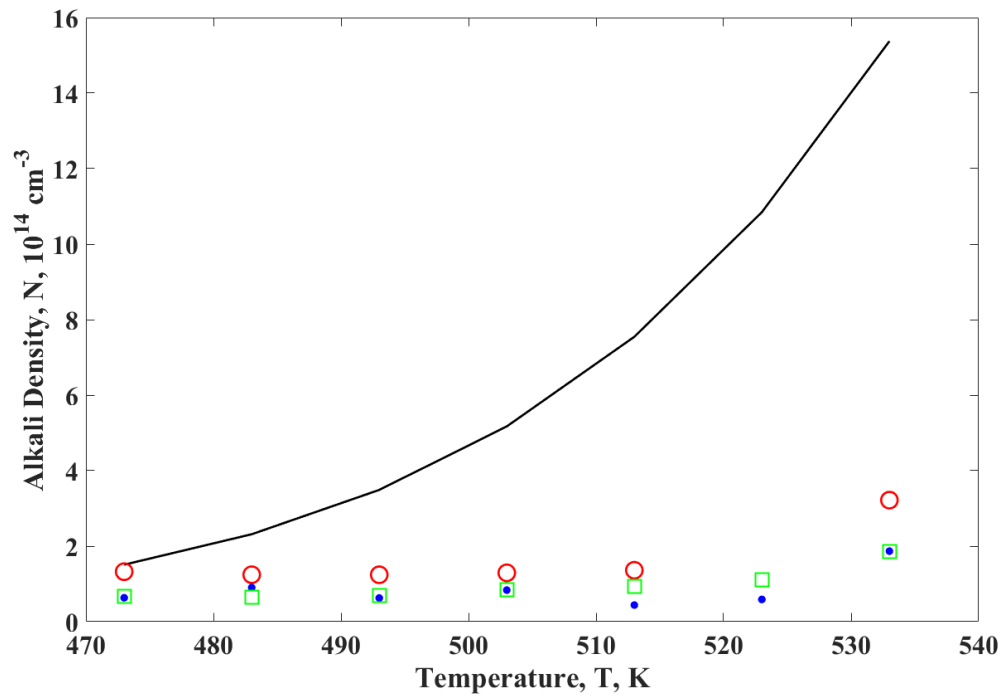
Figure 20. Potassium density measurements: (black line) vapor pressure as a function of melt pool temperature (75), (blue •) TDLAS measurements, (red ○) estimates from transmitted power, and (green □) estimates from K $4\,^2D$ emission. Observations for helium pressure of 250 Torr and flow speed of 0.98 m/s, and melt pool residence time of 0.104 s.

flow increases the flow transit time over the bed increasing the vapor saturation, but it also increases the likelihood of alkali condensing on the walls before it reaches the laser. The alkali density, as estimated by the K $4\,^2D$ population, trends downward .
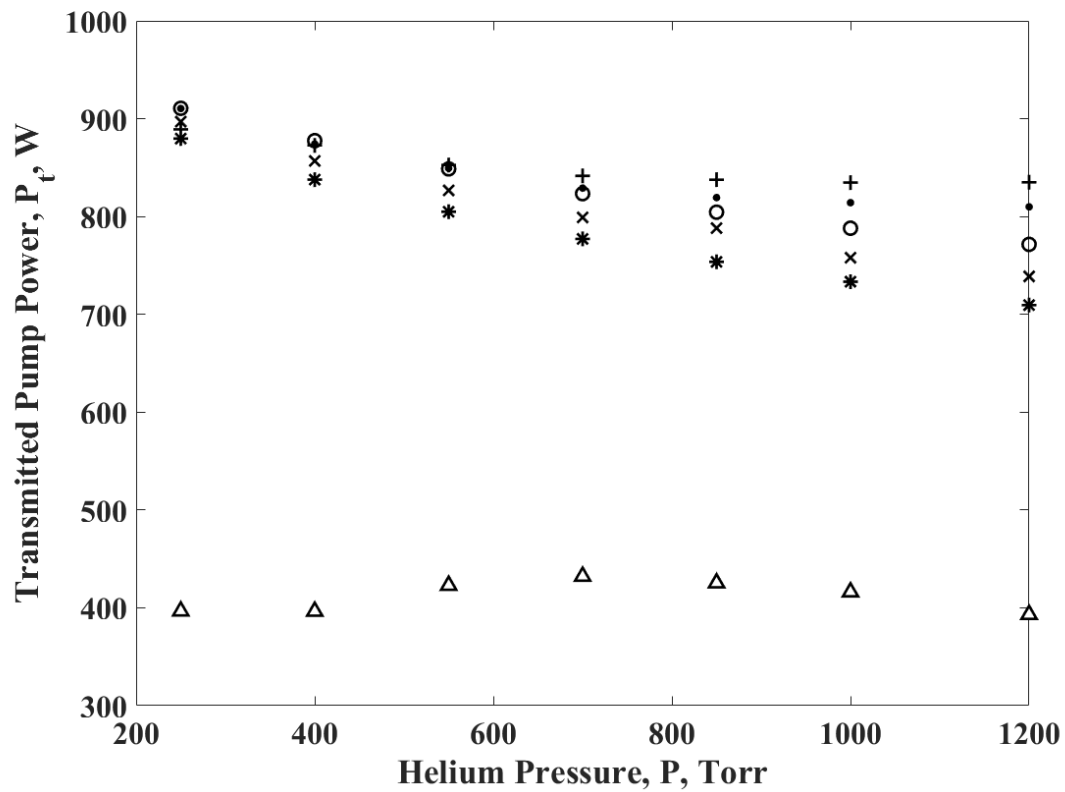
Figure 21. The pump power transmitted through the alkali cell as a function of buffer gas pressure for $T = 473$ **K** (+)**, 483 K** (•)**, 493 K** (○)**, 503 K** (×)**, 513 K** (∗) **and 533 K** (△)**. The incident pump power is 1.23 kW.**
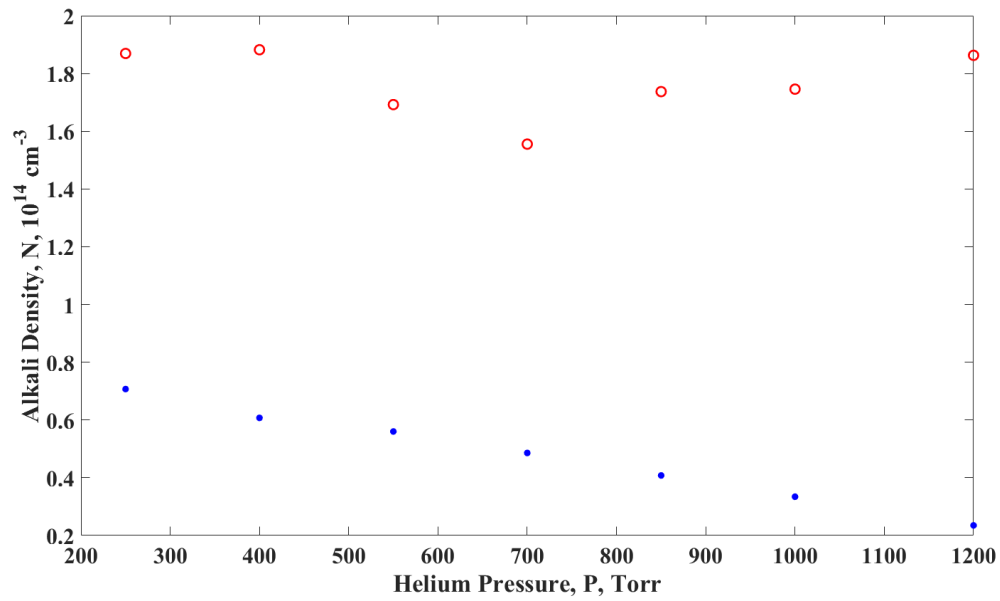
Figure 22. The alkali density as estimated by the K $4\,^2D$ emission as a function of helium pressure at alkali bed temperatures of $T = 473$ K (blue •) and $T = 533$ K (red ○).

62

3.3.2 Fluorescence Spectra.

A sample visible spectrum is provided in Figure 23. The spectral assignments have been annotated and include $n = 4 - 11$ with 32 atomic transitions in potassium as well as 4 rubidium and 2 sodium lines. A list of the observed atomic transitions are provided in Table 7 and illustrated graphically on the energy level diagram in Figure 24. The intermediate states, $6S$, $5P$ and $4D$, lie near the energy of two pump photons, indicated by the higher dashed line in Figure 24. The energy associated with one pump photon below the ionization level is indicated by the lower dashed line. The strong blue emission arises from the $5P - 4S$ transition. The higher lying P states emit outside the range of the visible spectrometer, including the $6P - 4S$ line near 344 nm, and the $9P - 5S$ line near 839 nm.

The observed intensities in Figure 23, I, have been scaled by detector response, D, for an integration time of 1 s. For example the blue emission near 404 nm, observed a peak spectral intensity of $I = 4.18 \times 10^5$ counts/nm, with a detector response corresponds of $D = 8.95 \times 10^{-9}$ counts/photon-s, corresponding to a photon emission rate of 4.67×10^{13} 1/nm-s. Figure 25 demonstrates a simultaneous fit for these two blue transitions, $5\,^2P_{\frac{3}{2},\frac{1}{2}} \to 4\,^2S_{\frac{1}{2}}$. The spectral resolution, as specified by the Lorentzian FWHM is 0.28 nm. The instrumental line shape is rather symmetric but exhibits some non-Lorentzian character, resulting in residuals of 6% (of the peak) in the wings. A constant baseline was found to be less than 1×10^{-3} the peak value. These Lorenztian fits are used to calculate the densities in the excited states.

The spectral signal-to-noise of 3,000 leads to a well determined amplitude of $1.22 \pm 0.02 \times 10^{17}$. Similar fits for all the lines yield the observed intensities reported in the final column of Table 7.
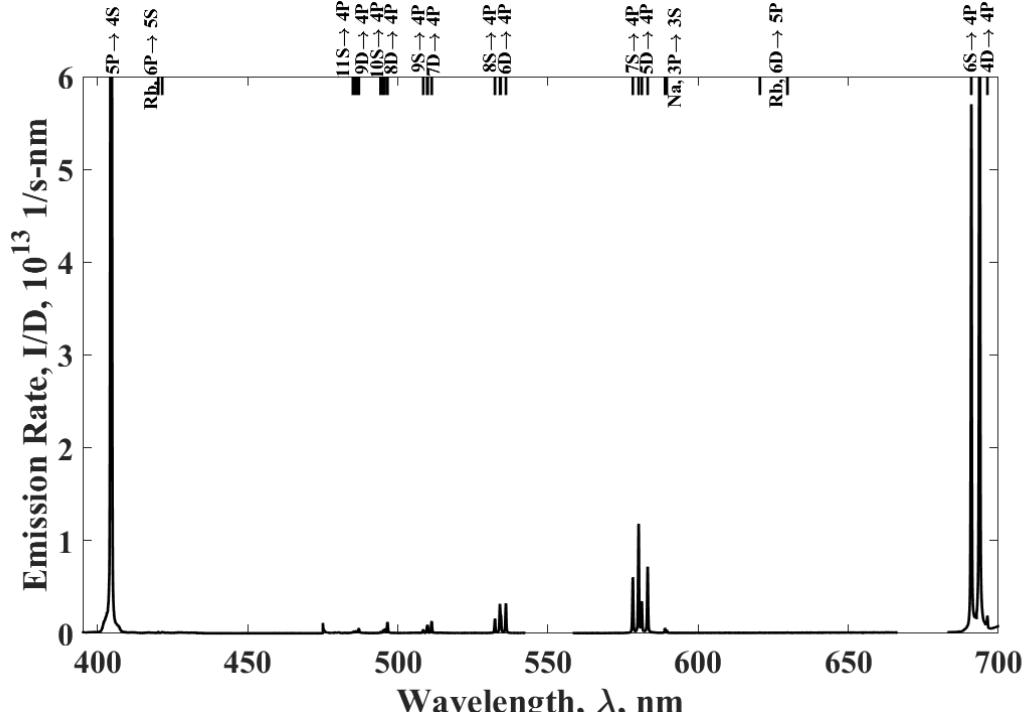
Figure 23. **Visible fluorescence spectrum collected at a K bed temperature of 533 K at 250 Torr of pure helium.**

Table 7. **Observed atomic K transitions with A-coefficients, and fit intensity amplitude for test conditions** $T = 260$ **K** $(N = 1.87 \times 10^{14}\,cm^{-3})$ **and** $P = 250$ **Torr.**

Upper State, i	Lower State, j	λ_{ij}, nm	A_{ij}, $10^6\,s$	Observed Intensity	Intensity Uncertainty
$5^2\,P_{\frac{3}{2}}$	$4^2\,S_{\frac{1}{2}}$	404.41	1.16	2.88×10^{17}	3.9×10^{15}
$5^2\,P_{\frac{1}{2}}$	$4^2\,S_{\frac{1}{2}}$	404.72	1.07	1.52×10^{17}	2.6×10^{15}
$11^2\,S_{\frac{1}{2}}$	$4^2\,P_{\frac{1}{2}}$	484.98	0.14	2.81×10^{14}	5.9×10^{12}
$9^2\,D_{\frac{3}{2}}$	$4^2\,P_{\frac{1}{2}}$	485.61	0.18	5.25×10^{14}	6.1×10^{12}
$11^2\,S_{\frac{1}{2}}$	$4^2\,P_{\frac{3}{2}}$	486.35	0.29	4.57×10^{14}	5.9×10^{12}
$9^2\,D_{\frac{3}{2}}$	$4^2\,P_{\frac{3}{2}}$	486.97	0.035	1.33×10^{15}	7.7×10^{12}
$9^2\,D_{\frac{5}{2}}$	$4^2\,P_{\frac{3}{2}}$	486.98	0.21		
$10^2\,S_{\frac{1}{2}}$	$4^2\,P_{\frac{1}{2}}$	494.20	0.213	2.60×10^{14}	1.2×10^{13}

64

$8^2 D_{\frac{3}{2}}$	$4^2 P_{\frac{1}{2}}$	495.08	0.22	7.01×10^{14}	1.2×10^{13}
$10^2 S_{\frac{1}{2}}$	$4^2 P_{\frac{3}{2}}$	495.61	0.425	9.22×10^{14}	1.2×10^{13}
$8^2 D_{\frac{3}{2}}$	$4^2 P_{\frac{3}{2}}$	496.50	0.046	3.07×10^{15}	1.6×10^{13}
$8^2 D_{\frac{5}{2}}$	$4^2 P_{\frac{3}{2}}$	496.50	0.26		
$9^2 S_{\frac{1}{2}}$	$4^2 P_{\frac{1}{2}}$	508.42	0.35	7.29×10^{14}	1.3×10^{13}
$7^2 D_{\frac{3}{2}}$	$4^2 P_{\frac{1}{2}}$	509.72	0.29	1.37×10^{15}	2.5×10^{13}
$9^2 S_{\frac{1}{2}}$	$4^2 P_{\frac{3}{2}}$	509.92	0.70	9.51×10^{14}	2.5×10^{13}
$7^2 D_{\frac{3}{2}}$	$4^2 P_{\frac{3}{2}}$	511.22	0.076	2.87×10^{15}	1.7×10^{13}
$7^2 D_{\frac{5}{2}}$	$4^2 P_{\frac{3}{2}}$	511.23	0.35		
$8^2 S_{\frac{1}{2}}$	$4^2 P_{\frac{1}{2}}$	532.32	0.63	3.39×10^{15}	4.5×10^{13}
$8^2 S_{\frac{1}{2}}$	$4^2 P_{\frac{3}{2}}$	533.97	1.26	6.12×10^{15}	5.7×10^{13}
$6^2 D_{\frac{3}{2}}$	$4^2 P_{\frac{1}{2}}$	534.30	0.40	3.13×10^{15}	4.8×10^{13}
$6^2 D_{\frac{3}{2}}$	$4^2 P_{\frac{3}{2}}$	535.95	0.076	7.14×10^{15}	5.4×10^{13}
$6^2 D_{\frac{5}{2}}$	$4^2 P_{\frac{3}{2}}$	535.96	0.46		
$7^2 S_{\frac{1}{2}}$	$4^2 P_{\frac{1}{2}}$	578.24	1.23	1.13×10^{16}	7.6×10^{13}
$7^2 S_{\frac{1}{2}}$	$4^2 P_{\frac{3}{2}}$	580.18	2.46	2.18×10^{16}	8.8×10^{13}
$5^2 D_{\frac{3}{2}}$	$4^2 P_{\frac{1}{2}}$	581.21	0.28	5.82×10^{15}	7.0×10^{13}
$5^2 D_{\frac{3}{2}}$	$4^2 P_{\frac{3}{2}}$	583.17	0.054	1.34×10^{16}	7.1×10^{13}
$5^2 D_{\frac{5}{2}}$	$4^2 P_{\frac{3}{2}}$	583.18	0.32		
$6^2 S_{\frac{1}{2}}$	$4^2 P_{\frac{1}{2}}$	691.11	2.72	7.72×10^{16}	5.3×10^{14}
$4^2 D_{\frac{3}{2}}$	$4^2 P_{\frac{1}{2}}$	693.63	0.026	1.49×10^{17}	7.0×10^{14}
$6^2 S_{\frac{1}{2}}$	$4^2 P_{\frac{3}{2}}$	693.88	3.9		
$4^2 D_{\frac{3}{2}}$	$4^2 P_{\frac{3}{2}}$	696.42	0.0051	2.79×10^{15}	4.4×10^{14}
$4^2 D_{\frac{5}{2}}$	$4^2 P_{\frac{3}{2}}$	696.47	0.041		
$3^2 D_{\frac{3}{2}}$	$4^2 P_{\frac{1}{2}}$	1169.02	22.0	4.95×10^{15}	4.4×10^{14}

$3^2 D_{\frac{3}{2}}$	$4^2 P_{\frac{3}{2}}$	1176.96	4.24	8.73×10^{15}	6.0×10^{14}
$3^2 D_{\frac{5}{2}}$	$4^2 P_{\frac{3}{2}}$	1177.28	25.9		
$5^2 S_{\frac{1}{2}}$	$4^2 P_{\frac{1}{2}}$	1243.22	7.9	8.22×10^{15}	1.2×10^{14}
$5^2 S_{\frac{1}{2}}$	$4^2 P_{\frac{3}{2}}$	1252.21	15.6	1.22×10^{16}	1.3×10^{14}
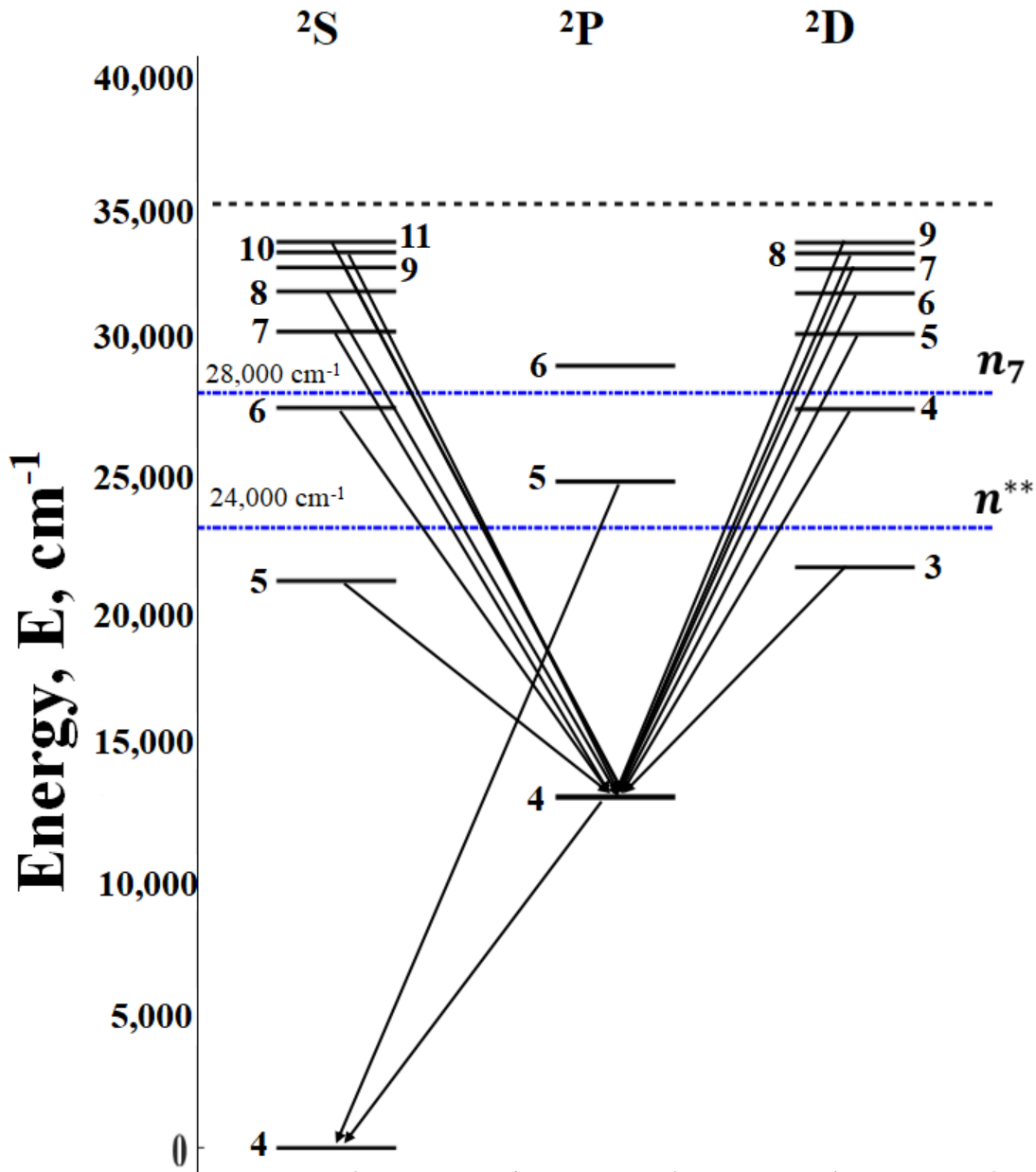
Figure 24. Energy diagram for potassium with observed spectral lines. The states between the two dot-dash lines are the intermediate states, and the Rydberg states are all states above the second blue line.
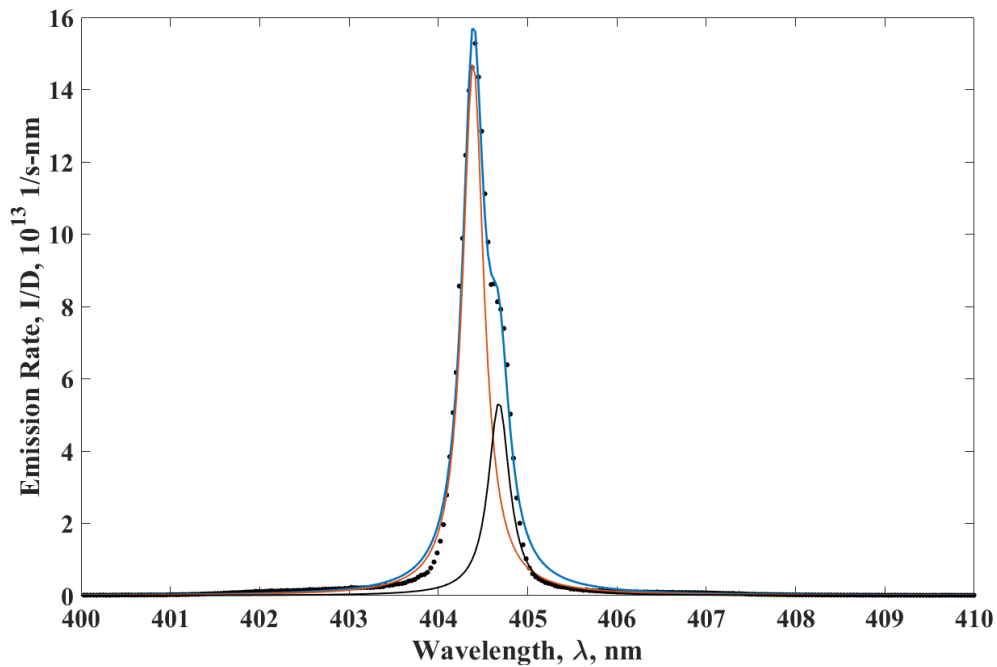
Figure 25. An example of the Lorenztian for the two blue lines at a potassium bed temperature of $T = 533$ K, and $N = 1.87 \times 10^{14}\, cm^{-3}$ at a pure helium buffer gas of $P = 250$ Torr.

The dependence of the fluorescence spectra on buffer gas (He and methane) pressure and potassium density are provided in Figures 26-28. The intensity of nearly all lines decreases at higher pressure due to quenching of the excited states. There are a few non-Lorenztian features that grow as buffer gas is increased, in the far blue wing of the D_2 line and near the two blues lines. The intensity of the primary atomic lines increases significantly with alkali density as expected. The highest intensities of atomic lines are observed with no methane. At 7.6% methane, the fluorescence intensity is decreased by a factor of 3-10. Non-Lorenztian features begin to grow as methane is added, specifically the far wing of the D_2 line. There are also additional molecular spectral features that arise in the range $475 - 550\, nm$.

The higher lying excited states are statistically distributed with temperatures of $T = 1,860 - 2,620$ K, as shown in Figure 29. A Boltzmann gas temperature of the
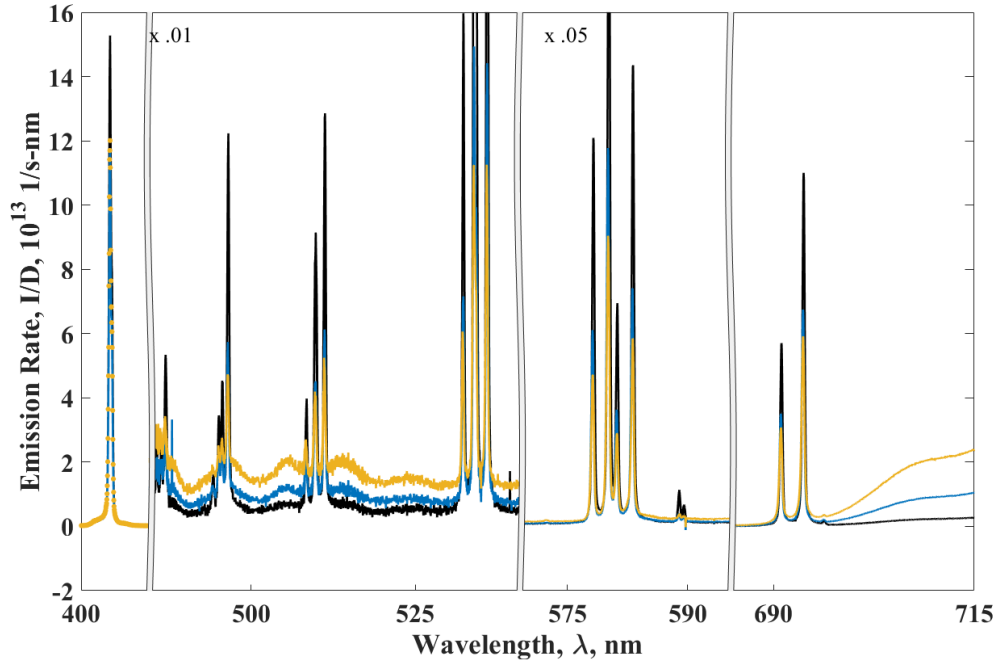
Figure 26. The addition of more buffer gas decreases the intensity of all of the transitions. The black curve are at 250 Torr, blue at 700 Torr, and yellow represents 1200 Torr, all with a density of $1.9 \times 10^{14} \, cm^{-3}$.

Rydberg states can be calculated from the observed lines by fitting a curve to

$$\frac{n_i}{n_0} = \frac{g_i}{g_0} e^{\Delta E/kT} \tag{63}$$

where $n_{i,0}$ is the population in the fine structure split state i and the ground state, respectively, and $g_{i,0}$ are their degeneracies, $\Delta E = E_i - E_0$ is the energy difference between the upper and ground state, and k is the Boltzmann's constant. This curve does a poor job of estimating the lower states because the population in the excited states is not statistically distributed, driven instead by a complex kinetic mechanism. The Rydberg states are likely rapidly equilibrated, though, so a Boltzmann temperature may be appropriate. The density in the higher P states which are not observed in the visible spectra can be estimated using this temperature. The curves on Figure 29 correspond to gas temperatures of $T = 2,620 \pm 290$, $1,210 \pm 350$, and $1,860 \pm 250$

69
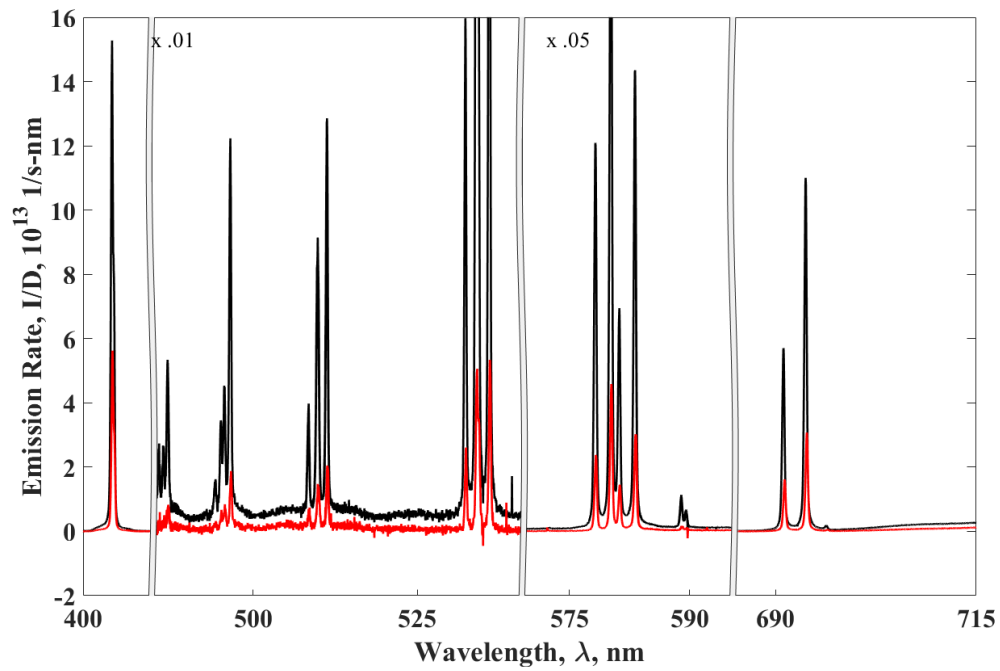
Figure 27. The fluorescence of the lines goes up with alkali density. The density of the red curve is $0.6 \times 10^{14}\,cm^{-3}$ and the black represent a density of $1.87 \times 10^{14}\,cm^{-3}$ with pure helium buffer gas at a pressure of 250 Torr.

K for pressures of $P = 250$, 700, and 1,200 Torr, respectively.
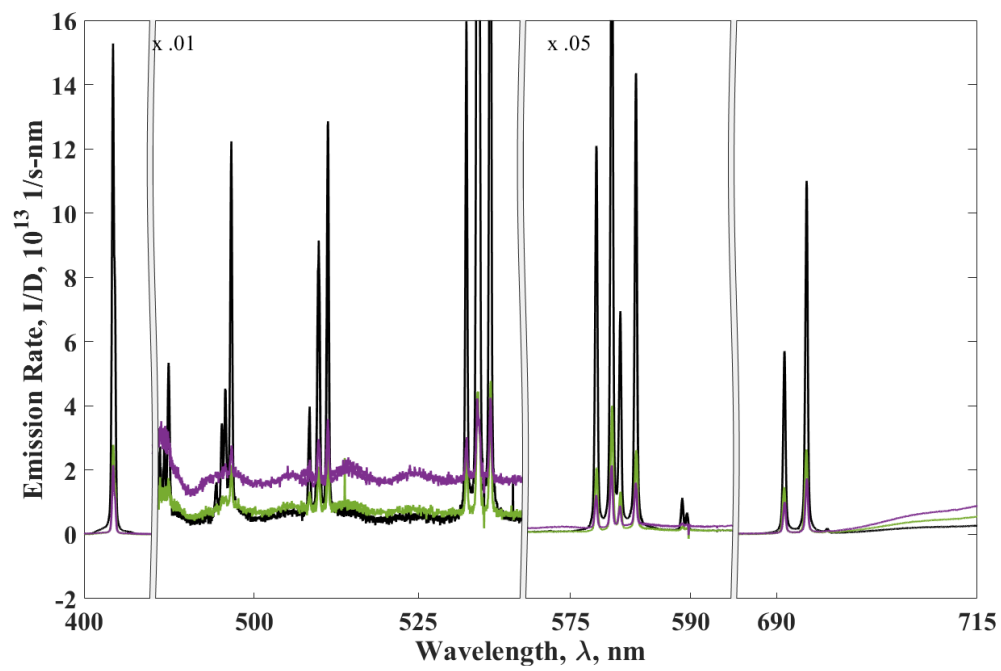
Figure 28. Methane rapidly quenches fluorescence. Methane mass fractions are 0% (black), 7.6% (green), and 13.5% (purple) with a total pressure of 250 Torr, at $1.9 \times 10^{14}\,cm^{-3}$.
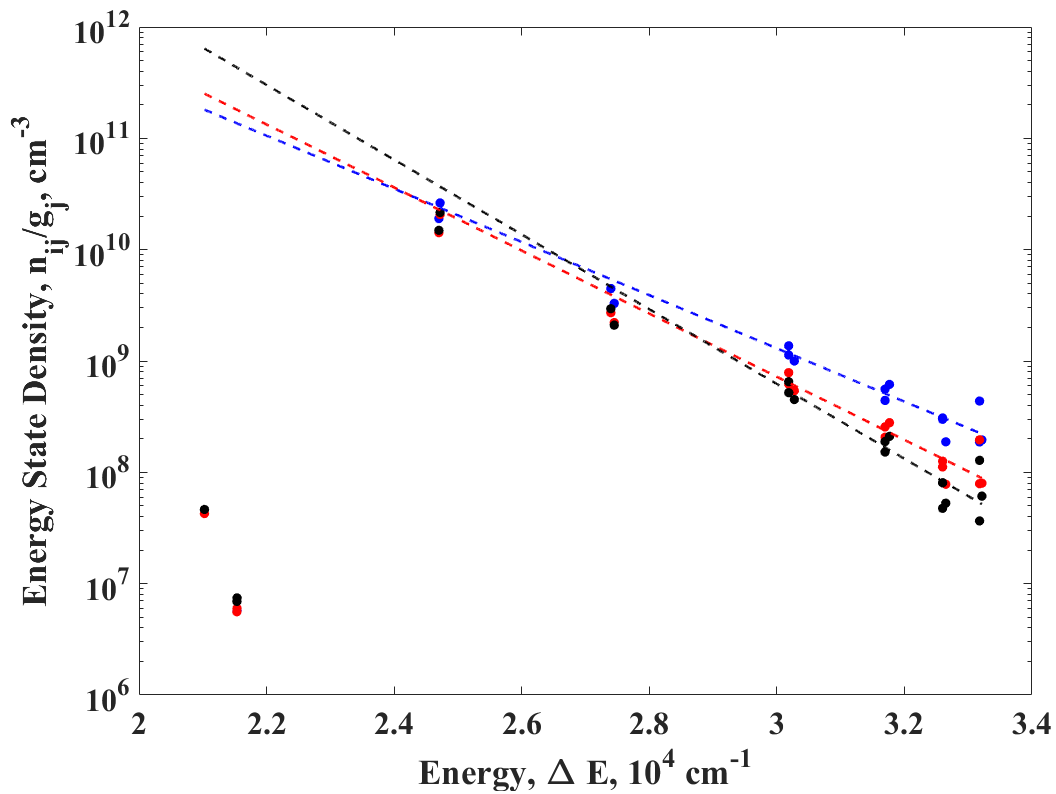
Figure 29. Boltzmann temperatures derived from excited state density at buffer gas pressures of 250 Torr (blue), 700 Torr (red), and 1,200 Torr (black). These temperatures range from 1,050-1,350 K.

3.4 Kinetic modeling

3.4.1 Reaction mechanism and rates.

A kinetic model describing the population of the higher energy states was recently developed (70). The two major parameters that this model seeks to predict are the density excited out of the lowest lasing states, δ, and the additional heat loading of the alkali vapor due to the relaxation of these highly excited states. The model considers nine energy levels as described in Table 8. The model builds on the prior analytic formulation of the three lasing states, n_1, n_2, and n_3 (14). The population moved out of these states is considered as a small perturbation. The intermediate states, $4^2D(n_4)$, $5^2P(n_5)$, and $6^2S(n_6)$ are populated through photo-excitation into the far non-Lorenztian wings of the absorption feature and energy pooling. Photo-

Table 8. Relevant potassium energy levels and term symbols

State	Term Symbol	Level, i	Energy, E_i (cm^{-1})	g_i
Ground State	$4^2S_{\frac{1}{2}}$	1	0	2
Upper Laser State	$4^2P_{\frac{3}{2}}$	2	12,985.186	2
Pumped State	$4^2P_{\frac{1}{2}}$	3	13,042.896	4
Intermediates	$4^2D_{\frac{3}{2},\frac{5}{2}}$	4	27,398.147	4
			27,397.077	6
	$5^2P_{\frac{1}{2},\frac{3}{2}}$	5	24,701.382	2
			24,720.139	4
	$6^2S_{\frac{1}{2}}$	6	27,450.710	2
Rydberg States	higher n	7	28,000-35,009	
Atomic Ion	$^1S_0$	8	35,009.814	1
Ionic Dimer	$X^2\Sigma_g$	9	28,880	2

excitation occurs when a pump or laser photon is absorbed by an atom in the $4P$ states and is excited to either the $4D$ or $6S$, $K(4P) + h\nu \rightarrow K(4D, 6S)$. The rate of this excitation is uncertain as insufficient potential surfaces for the upper states exist (76). Energy pooling occurs when two excited alkali collide resulting in the

73

formation of a doubly excited atom and one in the ground state, $K(4P) + K(4P) \rightarrow$ $K(4D, 5P, 6S) + K(4S)$. The rates for these processes have been studied in some detail for in all alkali metal vapors (42; 43; 44; 45).

Destruction of the intermediate states occurs through radiative processes, collisional de-excitation (quenching), and ionization. Ionization occurs primarily through photo-ionization and Penning ionization. Penning ionization is the ionizing analogue of energy pooling (77). The ion density is monitored as n^+. The dominant recombination process passes through the ionic dimer, n_2^+ (78). Dissociative recombination creates a ground state alkali and excited states, above the intermediate states. All levels above the intermediate states are combined into one model level, the Rydberg states, n_7.

The steady state solutions for all nine levels in a CW regime have been recently developed (70) and are:

$$n_1 = \frac{(\frac{\sigma_{13}\Omega}{2h\nu_p} + \gamma_3)n_3 + (\frac{\sigma_{12}\Psi}{h\nu_l} + \gamma_2)n_2}{\frac{\sigma_{13}\Psi}{h\nu_p} + \frac{\sigma_{12}\Psi}{h\nu_l}} \tag{64}$$

$$n_2 = \frac{\frac{\sigma_{12}\Psi}{h\nu_l}n_1 + \gamma_{32}n_3}{\frac{\sigma_{12}\Psi}{h\nu_l} + \gamma_2 + 2\gamma_{32}e^{-\theta}} \tag{65}$$

$$n_3 = \frac{2\gamma_{32}e^{-\theta}n_2 + \frac{\sigma_{13}\Omega}{2h\nu_p}n_1}{\frac{\sigma_{13}\Omega}{h\nu_p} + \gamma_{32}e^{-\theta} + \gamma_3} \tag{66}$$

$$n_4 = \frac{k_4^p * n_3^2 + \frac{\alpha^4\sigma_L^4}{h\nu_p}(\Omega + \Psi)(n_2 + n_3)}{k_4^{PI}(n_2 + n_3) + \frac{\sigma_4^{ph}}{h\nu_p}(\Omega + \Psi) + \gamma_4} \tag{67}$$

$$n_6 = \frac{k_6^p * n_3^2 + \frac{\alpha^6\sigma_L^6}{h\nu_p}(\Omega + \Psi)(n_2 + n_3)}{k_6^{PI}(n_2 + n_3) + \frac{\sigma_6^{ph}}{h\nu_p}(\Omega + \Psi) + \gamma_6} \tag{68}$$

$$n_5 = \frac{k_5^p * n_3^2 + \gamma_{45}n_4 + \gamma_{65}n_6}{k_5^{PI}(n_2 + n_3) + \frac{\sigma_5^{ph}}{h\nu_p}(\Omega + \Psi) + \gamma_5} \tag{69}$$

74

$$n^+ = \frac{k^{PI}(n_2 + n_3)n^{**} + \frac{\sigma^{ph}}{h\nu_p}(\Omega + \Psi)n^{**}}{k_a M N} \tag{70}$$

$$n_2^+ = \sqrt{\frac{k_a M N n^+}{k_{DR}}} \tag{71}$$

$$n_7 = \frac{k_{DR} n_2^+ (n_2^+ + n^+)}{\gamma_7} \tag{72}$$

where $\sigma_{13,12}$ are the stimulated emission cross section for the pump and lase transition, respectively, Ω and Ψ are the intracavity longitudinally averaged pump and laser intensity, respectively, and $\nu_{p,l}$ are the pump and lasing frequencies. The pseudo first order spin-orbit mixing rate for the $4\,^2P$ states, γ_{32} constrained by detailed balance with $\theta = \Delta E_{32}/kT$, where ΔE_{32} is the spin orbit splitting. All other excited states decay radiatively and collision with the rates $\gamma_i = A_i + k_{qi}M$, where A_i is the sum of the Einstein A-coefficients out of the given state, k_{qi} is the quenching rate, and M is the buffer gas density. The effective pooling rate out of $n_{2,3}$ to $n_{4,5,6}$ are specified by $k_{4,5,6}^p$ and σ_w is the wing absorption cross section to $n_{4,6}$ by either a pump or lase photons. The rate coefficients $k_{4,5,6}^{PI}$ and optical cross sections $\sigma_{4,5,6}^{ph}$ are for Penning ionization and photo-ionization out of the intermediate states. Lastly, k_a is the dimer association rate and k_{DR} is the dissociation recombination rate. The mechanism and recommended rate coefficients from the literature review in reference (70) are summarized in Table 9.

Table 9. Kinetic mechanisms with updated rates

Parameter	Reaction	Recommended Value (70)	Modified Value (current result)	Units
A_{31}	$n_3 \rightarrow n_1 + h\nu$	3.80×10^7	3.80×10^7	s^{-1}
A_{21}	$n_2 \rightarrow n_1 + h\nu$	3.75×10^7	3.75×10^7	s^{-1}
A_4	$n_4 \rightarrow n_{i<4} + h\nu$	3.44×10^6	3.44×10^6	s^{-1}

A_5	$n_5 \rightarrow n_{i<5} + h\nu$	7.23×10^6	7.23×10^6	s^{-1}
A_6	$n_6 \rightarrow n_{i<6} + h\nu$	11.42×10^6	11.42×10^6	s^{-1}
A_7	$n_7 \rightarrow n_{i<7} + h\nu$	2.0×10^6	2.0×10^6	s^{-1}
A_{45}	$n_4 \rightarrow n_5 + h\nu$	3.43×10^6	3.43×10^6	s^{-1}
A_{65}	$n_6 \rightarrow n_5 + h\nu$	4.80×10^6	4.80×10^6	s^{-1}
σ_b^{D1}		4.87×10^{-15}	4.87×10^{-15}	cm^2
σ_b^{D2}		3.39×10^{-15}	3.39×10^{-15}	cm^2
k_{31}	$n_3 + M \rightarrow n_1 + M$	0	0	$cm^3/(atom-s)$
k_{21}	$n_2 + M \rightarrow n_1 + M$	0	0	$cm^3/(atom-s)$
k_{32}	$n_3 + M \rightarrow n_3 + M$	6.68×10^{-10}	6.68×10^{-10}	$cm^3/(atom-s)$
k_{45}	$n_4 + M \rightarrow n_5 + M$	2.27×10^{-12}	5.53×10^{-12}	$cm^3/(atom-s)$
k_{65}	$n_6 + M \rightarrow n_5 + M$	3.58×10^{-13}	2.32×10^{-12}	$cm^3/(atom-s)$
k_4	$n_4 + M \rightarrow n_{i<4} + M$	2.29×10^{-12}	1.11×10^{-11}	$cm^3/(atom-s)$
k_5	$n_5 + M \rightarrow n_{i<5} + M$	1.64×10^{-13}	1.11×10^{-12}	$cm^3/(atom-s)$
k_6	$n_6 + M \rightarrow n_{i<6} + M$	8.52×10^{-13}	5.53×10^{-12}	$cm^3/(atom-s)$
k_7	$n_7 + M \rightarrow n_{i<7} + M$	8.54×10^{-12}	1.7×10^{-12}	$cm^3/(atom-s)$

k_4^p	$n^* + n^* \rightarrow n_4 + n_1$	7.31×10^{-11}	7.31×10^{-11}	$cm^3/(atom-s)$
k_5^p	$n^* + n^* \rightarrow n_5 + n_1$	2.92×10^{-10}	1.18×10^{-10}	$cm^3/(atom-s)$
k_6^p	$n^* + n^* \rightarrow n_6 + n_1$	6.37×10^{-11}	1.21×10^{-11}	$cm^3/(atom-s)$
k_4^{PI}	$n_{2,3} + n_4 \rightarrow n_1 + n^+ + e^-$	5.79×10^{-8}	5.95×10^{-8}	$cm^3/(atom-s)$
k_5^{PI}	$n_{2,3} + n_5 \rightarrow n_1 + n^+ + e^-$	3.93×10^{-8}	8.07×10^{-8}	$cm^3/(atom-s)$
k_6^{PI}	$n_{2,3} + n_6 \rightarrow n_1 + n^+ + e^-$	4.49×10^{-8}	1.11×10^{-7}	$cm^3/(atom-s)$
K^{PI}	$n_{2,3} + n_{**} \rightarrow n_1 + n^+ + e^-$	1.42×10^{-7}	2.51×10^{-7}	$1/(atom-s)$
k_{DR}	$n_2^+ + e^- \rightarrow n_1 + n_{i \neq 1}$	5.26×10^{-7}	5.26×10^{-7}	$cm^3/(atom-s)$
k_a	$n^+ + n + M \rightarrow n_2^+ + M$	2.40×10^{-23}	2.40×10^{-23}	$cm^6/(atom-s)$
σ_L^4	$n_{2,3} + h\nu_{p,l} \rightarrow n_4$	3.62×10^{-14}	3.62×10^{-14}	cm^2
σ_L^6	$n_{2,3} + h\nu_{p,l} \rightarrow n_6$	4.84×10^{-14}	4.84×10^{-14}	cm^2
α^4		1	1.23×10^3	
α^6		1	0.62	

σ_4^{ph}	$n_4 \ + \ h\nu_{p,l} \ \rightarrow$ $n^+ + e^-$	1.40×10^{-17}	1.40×10^{-17}	cm^2
σ_5^{ph}	$n_5 \ + \ h\nu_{p,l} \ \rightarrow$ $n^+ + e^-$	6.37×10^{-18}	6.37×10^{-18}	cm^2
σ_6^{ph}	$n_6 \ + \ h\nu_{p,l} \ \rightarrow$ $n^+ + e^-$	3.41×10^{-20}	3.41×10^{-20}	cm^2
σph	$n^{**} \ + \ h\nu_{p,l} \ \rightarrow$ $n^+ + e^-$	2.03×10^{-17}	2.03×10^{-17}	cm^2

3.4.2 Revised rates from observed fluorescence.

Figures 32-37 compare the densities of the intermediate and Rydberg states observed in the present study with the model's predictions of Equations 64-72. A better agreement between the observations and predictions is obtained with the modified rate parameters reported in Table 9. A justification and methodology for obtaining the best agreement is provided in the following discussion.

Constraining the pooling rate to the prior recommended value, the wing absorption rate and quenching rate were modified to best fit the data. The mechanism presented in (70) for n_4 production is dominated by energy pooling, and the population grows rapidly with alkali density at densities seen here. The wing absorption rate is increased here so that it is non-negligible and matches the trends seen here, as shown in Figure 30. The red open circles are the prediction of (70) and grow superlinearly with alkali density. The blue open circles represent the new rate suggested here and trend correctly with the observed populations, here as the filled blue circles.

A similar approach is taken to better estimate the quenching rate of the $4\,^2D$ state. Figure 31 demonstrates the need for the new quenching rate recommend in
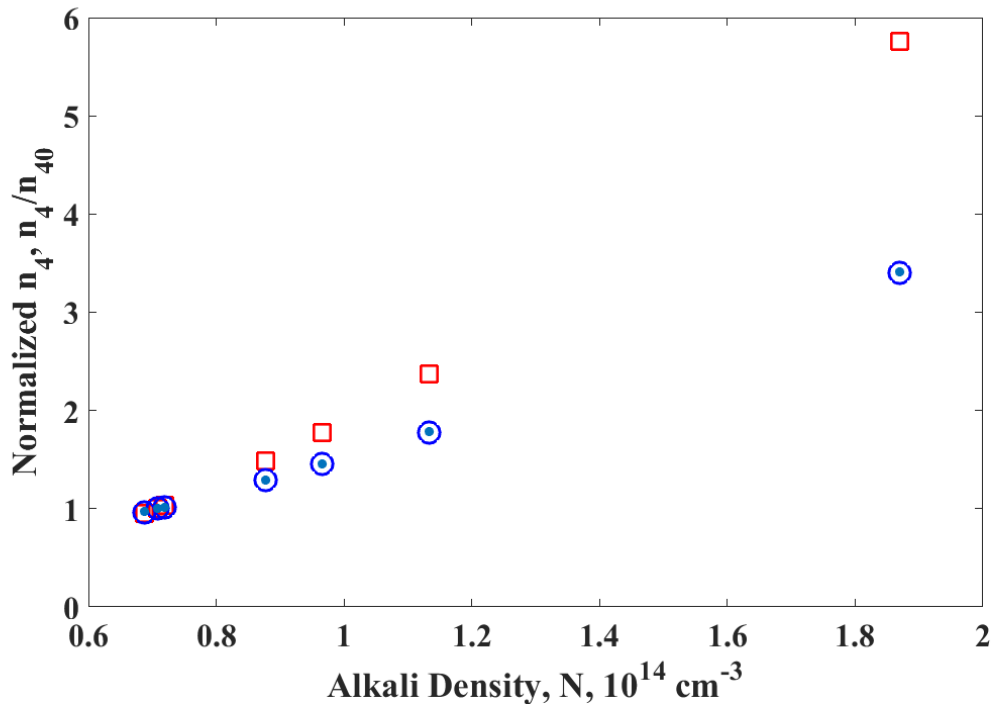
78

Figure 30. The density in $4\,^2D$ (normalized to the population when $N = 0.68 \times 10^{14}\,cm^{-3}$) as a function of alkali density. The new prediction suggested here (blue $\circ$) trends with the data ($\bullet$) much better than the previous values of (70) (red $\square$) at $P = 250$ **Torr.**

this study. Again, the open red circles are predicted from the previous quenching rate and the open blue circle are predicted with the new rates and match the data much better (filled blue circles).

The $4\,^2D$ population is shown in Figures 32-33. The error bounds in Figure 32 are determined from the statistical error in fitting the Lorentzian peak of the associated spectral feature. The systematic errors though, such as that associated with the Einstein A-coefficients, will only change the scale of these measurements and not their trends. For this reason, they will not be shown on these plots. The solid lines from the prediction of Equation 77, assumes a constant potassium density independent of helium pressure. The comparison is poor, particularly for lower K density and higher helium pressure where the degree of vapor saturation is strongly varying. The pressure dependence of the K density, as illustrated in Figure 22, can
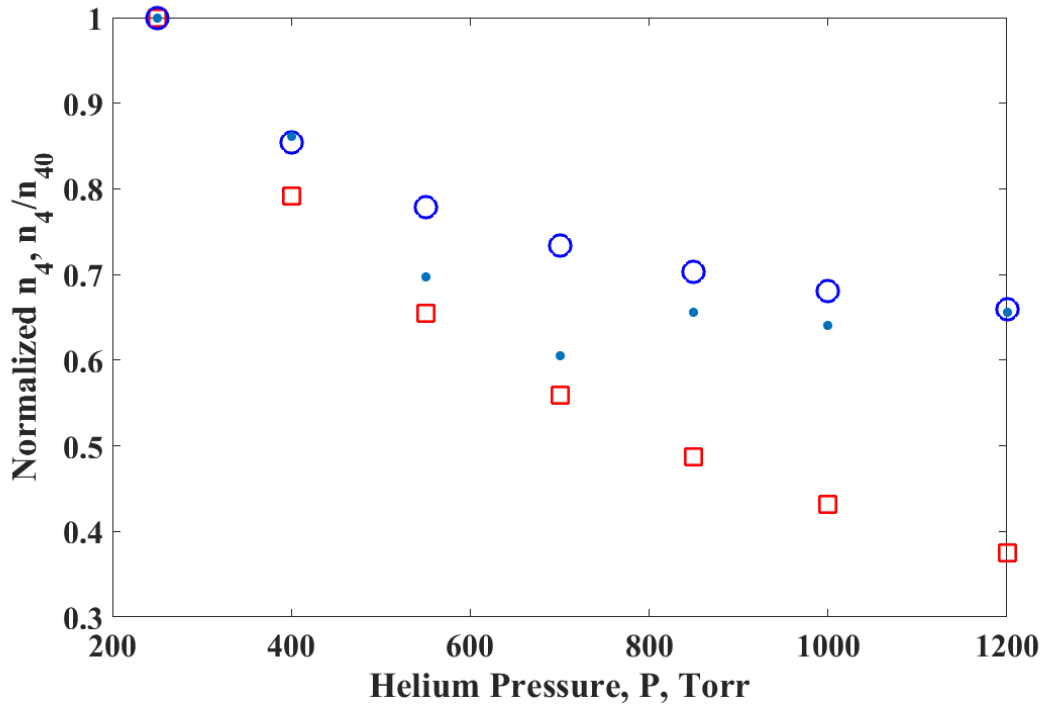
79

Figure 31. The density in $4\,^2D$ **(normalized to the population when** $P = 250$ **Torr) decreases rapidly with pressure. The new prediction suggested here (blue ○) trends with the data (●) much better than the previous values of (70) (red □) at** $N = 1.87 \times 10^{14}\,cm^{-3}$.

be ascertained by requiring the observed $4\,^2D$ state density to equal the prediction. The values for these K densities at 250 Torr are compared with the TDLAS and other observations in Figure 19. These results are generally higher than the TDLAS results, and lower than the transmitted power results. Figure 33 demonstrates the perfect fit of the model and the data when these new densities are used. These new K density values will be used to predict the population in the other excited states.

A similar approach is taken to adjust the rates for the $6\,^2S$, $5\,^2P$, and Rydberg states. Figure 34 demonstrates this for the $6\,^2S$. The mechanism from (70) greatly over predicts the number density, so the pooling rate is greatly decreased to match the observed data. This requires modification to the wing, Penning and quenching rate as well, to match the trend with pressure.

The predicted and observed population of $6\,^2S$, $5\,^2P$, and the Rydberg states are
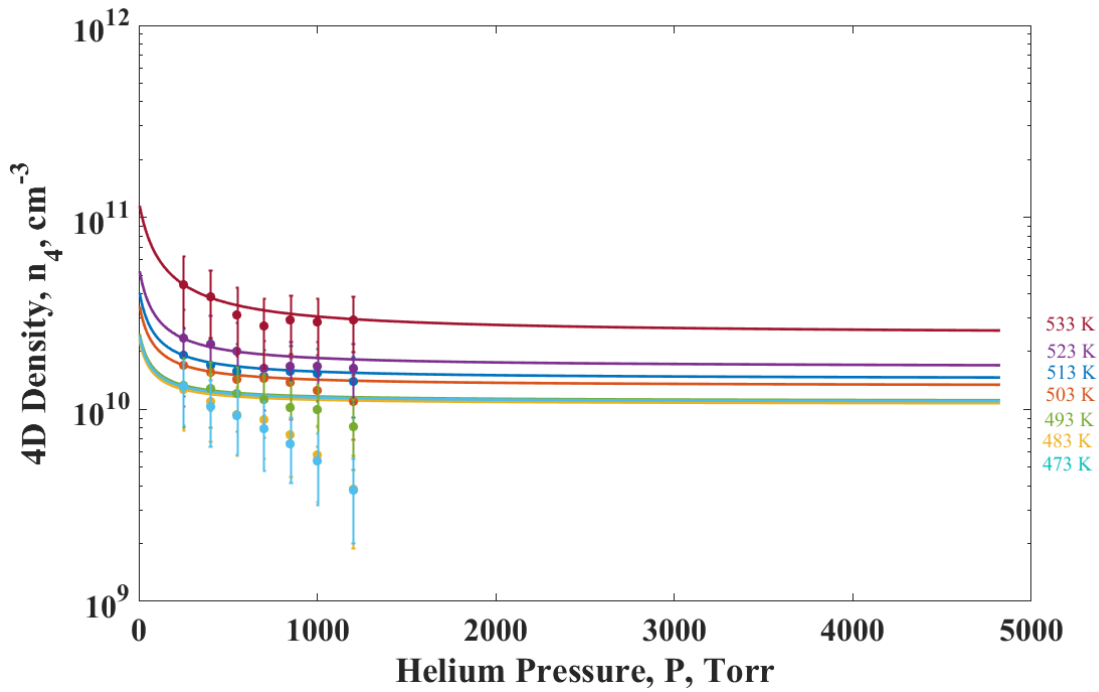
Figure 32. Predicted and observed (•) density in the $4D$ states as a function of pressure for bed temperatures of 473 (cyan), 483 (yellow), 493 (green), 503 (orange), 513 (blue), 523 (purple), and 533 (red), assuming a constant number density for each bed temperature. The uncertainty is the statistical error in fitting the Lorentzian peak.

shown in Figures 35, 36, and 37 respectively. The error bar associated with the fit's statistical error ($< 2.5\%$) is smaller than the data's marker on all of these figures. The Rydberg state population is the sum of the population in all of the observed states and the unobserved P states with energy less than the highest observed state using the temperatures from Figure 29. The modified model does an excellent job of predicting the data in the $6\,^2S$ states, though at low density and high pressure the observed values are systematically elevated over the model. The model also adequately predicts the $5\,^2P$ population; with a similar under prediction the density at high pressure. The $5\,^2P$ state is directly populated by relaxation from both the $6\,^2S$ and the $4\,^2D$ states and any variability in their predictions is propagated to this comparison. These issues are even more pronounced in the Rydberg population comparisons, as all the uncertainties in the three previous levels are prevalent.
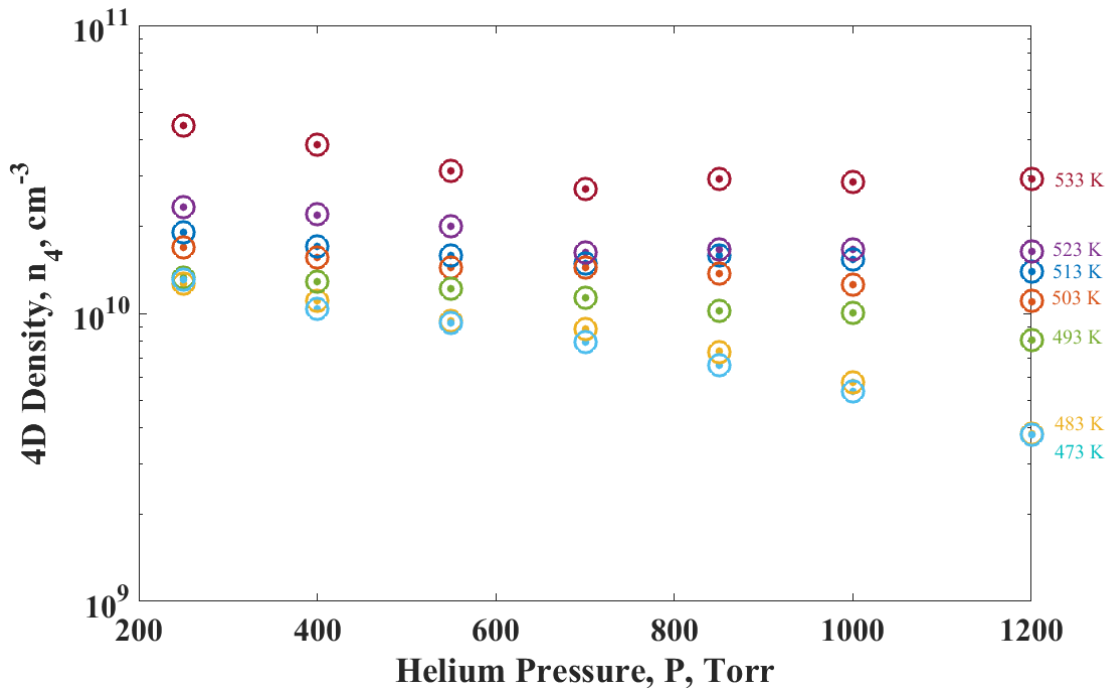
81

Figure 33. Predicted (○) and observed (●) density in the 4D states as a function of pressure for bed temperatures of 473 (cyan), 483 (yellow), 493 (green), 503 (orange), 513 (blue), 523 (purple), and 533 (red).

Figure 38 demonstrates the predicted and observed values of the higher excited states as a function of potassium density. The model predicts a near linear rise with alkali density, though, the data indicates that superlinear growth maybe possible at lower alkali densities. The inability to more accurately predict the $5\,^2P$ density (and by extension the Rydberg density) at low alkali density is due to bounds set by invariable rates. The linear production of $5\,^2P$ cannot be larger than the quenching rate of the other intermediate states, and the destruction is bounded below by the A-coefficient. These two constraints make it impossible to correctly predict the population of $5\,^2P$ at all densities, with the current mechanism. This is shown in Figure 39. The data requires that pooling be less dominant in production than the model suggests, however there is no other production mechanism that can be modified.

This seems to indicate that additional kinetics may be in play here. This exper-
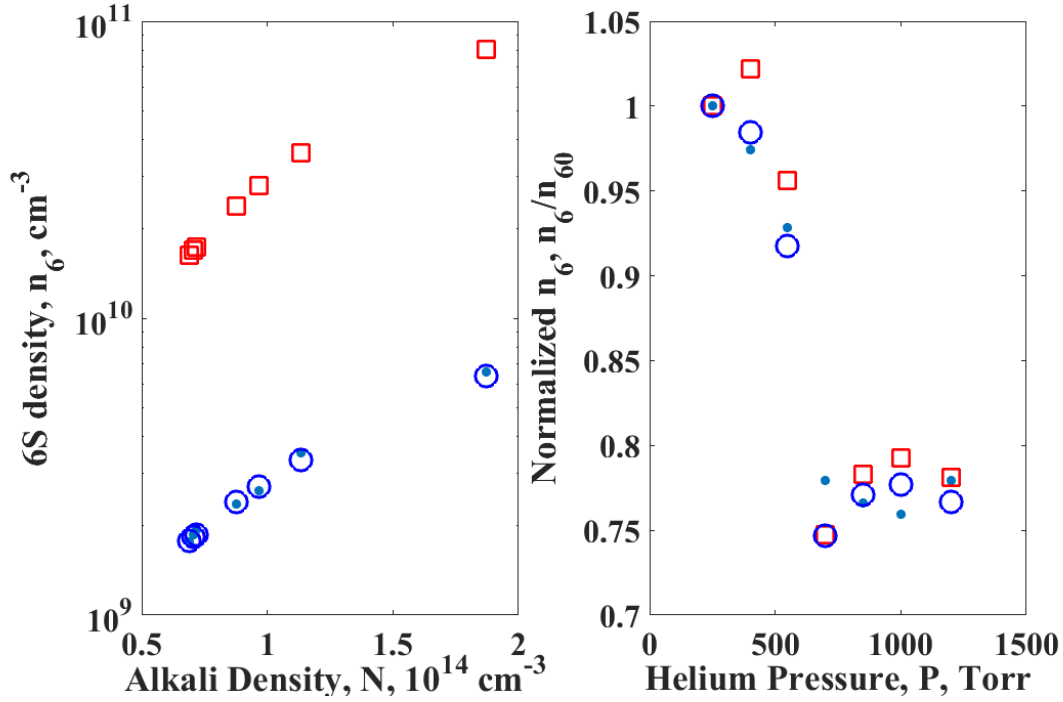
82

Figure 34. The density in $6\,^2S$ (normalized to the population when $N = 1.13 \times 10^{14}\,cm^{-3}$ on the right) as a function of number density (left) and pressure (right). The new prediction suggested here (blue ○) trends with the data (●) much better than the previous values of (70) (red □) at $N = 1.87 \times 10^{14}\,cm^{-3}$.

iment was unable to collect any electron density data, nor provide any information on the ion recombination rate. Compared to the helium density, the electron density is quite small. But even a small electron population could be coupled to the neutral density or the incident laser fields and effect the population in the higher states. The ion recombination rate dictates the electron density observed. Additionally, the ion density, specifically the dimer ion, makes up a majority of the total alkali density out of the lowest laser states. Figure 40 demonstrates this and shows the importance of the recombination rate on excited population. The solid line represents $\delta = n_4 + n_5 + n_6 + n^+ + 2n_2^+ + n_7$, the total alkali density removed from the lowest three levels, and the dashed line represents the potassium density in the dimer ion state. The dimer ion makes up more than $\sim 90\%$ of the total for all alkali densities. As the ion recombination rate changes, this proportion changes as well, but the dimer

Figure 35. Predicted (∘) and observed (●) density in the $6S$ states as a function of pressure for bed temperatures of 473 (cyan), 483 (yellow), 493 (green), 503 (orange), 513 (blue), 523 (purple), and 533 (red).
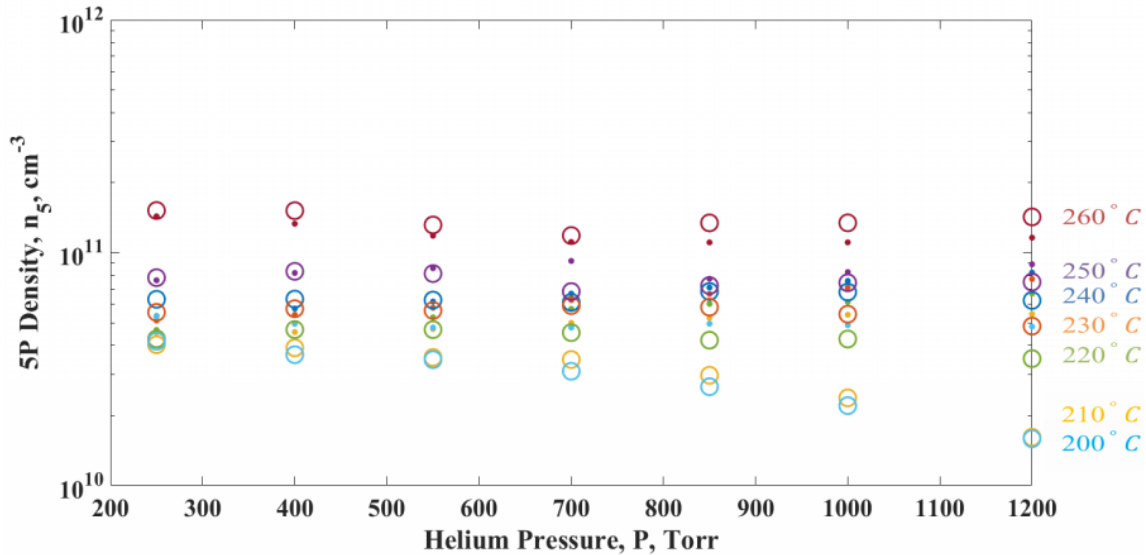
Figure 36. Predicted (∘) and observed (●) density in the $5P$ states as a function of pressure for bed temperatures of 473 (cyan), 483 (yellow), 493 (green), 503 (orange), 513 (blue), 523 (purple), and 533 (red).

still makes up $> 70\%$ of δ when the ion recombination rate is increased by a factor of 10 from the recommended value, in green on Figure 40.
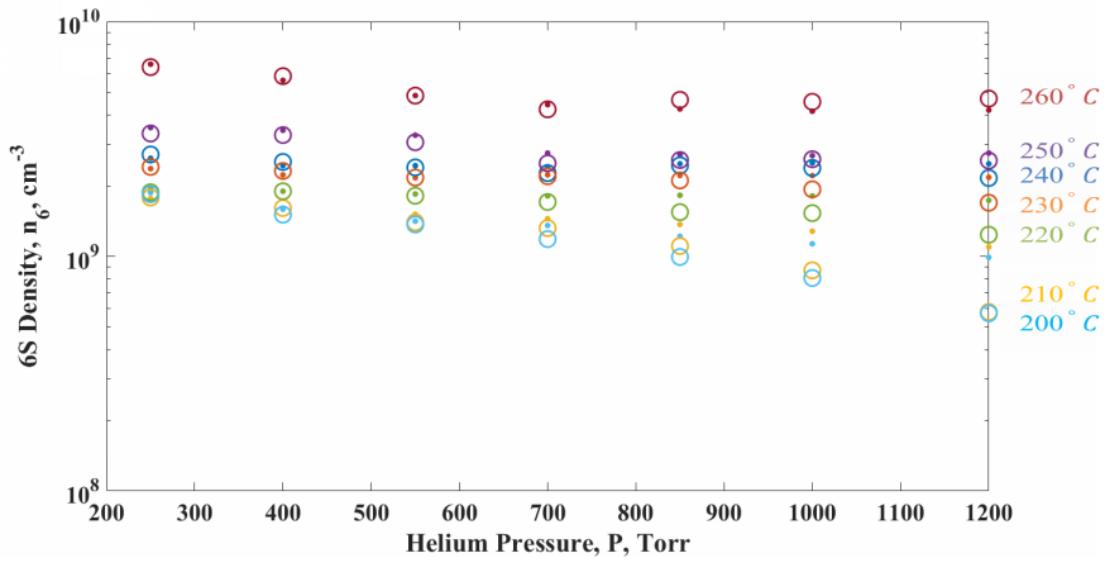
84
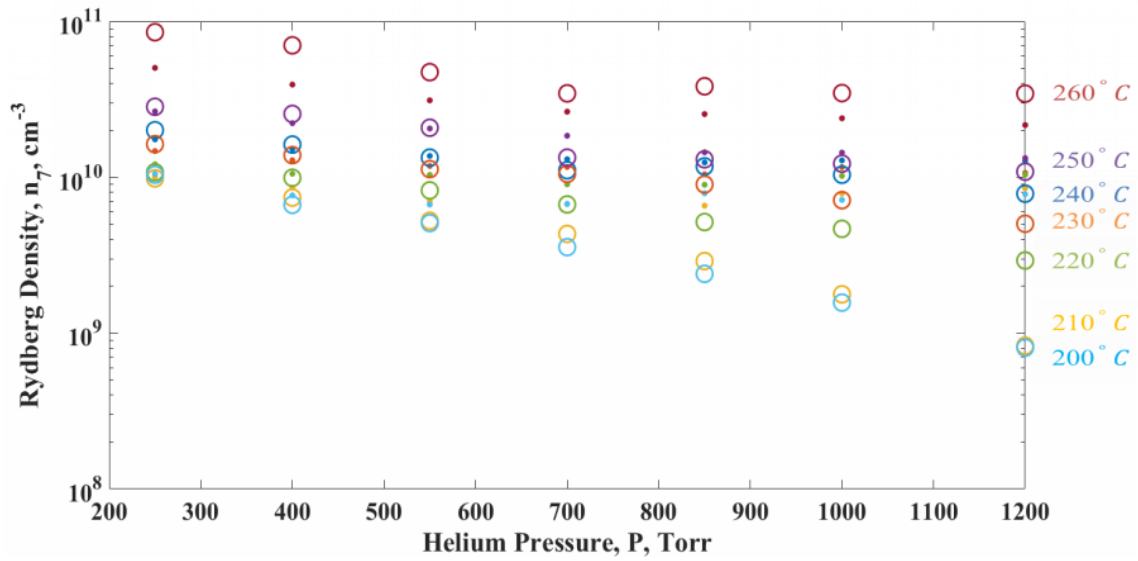
Figure 37. Predicted (○) and observed (●) density in the Rydberg states as a function of pressure for bed temperatures of 473 (cyan), 483 (yellow), 493 (green), 503 (orange), 513 (blue), 523 (purple), and 533 (red).
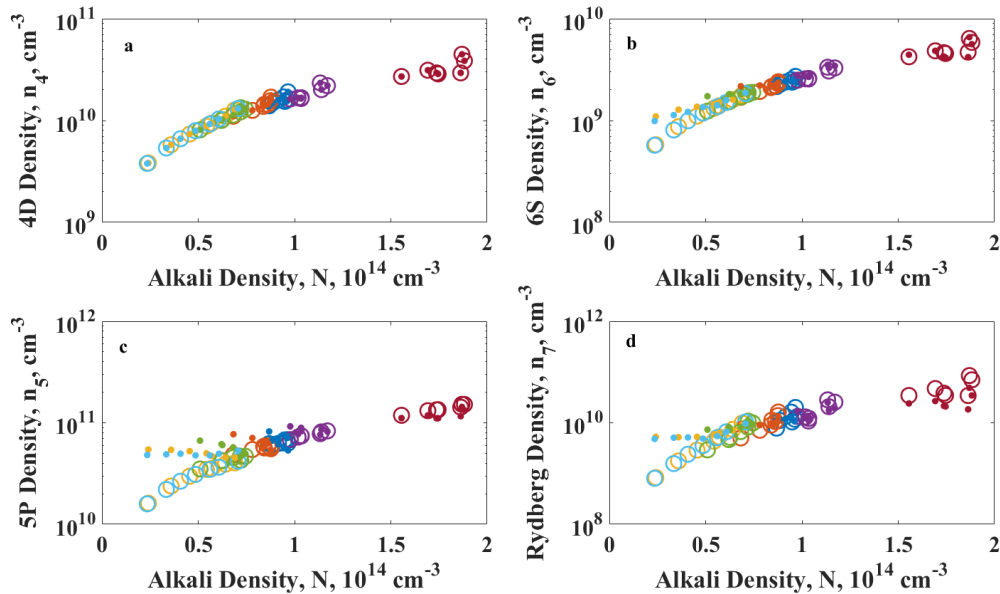
Figure 38. The population of the n_4 (a), n_6 (b), n_5 (c), and n_7 (d) states observed (●) and predicted (○) as a function of alkali density for bed temperatures of 473 (cyan), 483 (yellow), 493 (green), 503 (orange), 513 (blue), 523 (purple), and 533 K(red).

No ionic lines were observed in this experiment, that does not indicate the absence of molecular ions in the pumped volume. The first excited state of K^+ is at

85
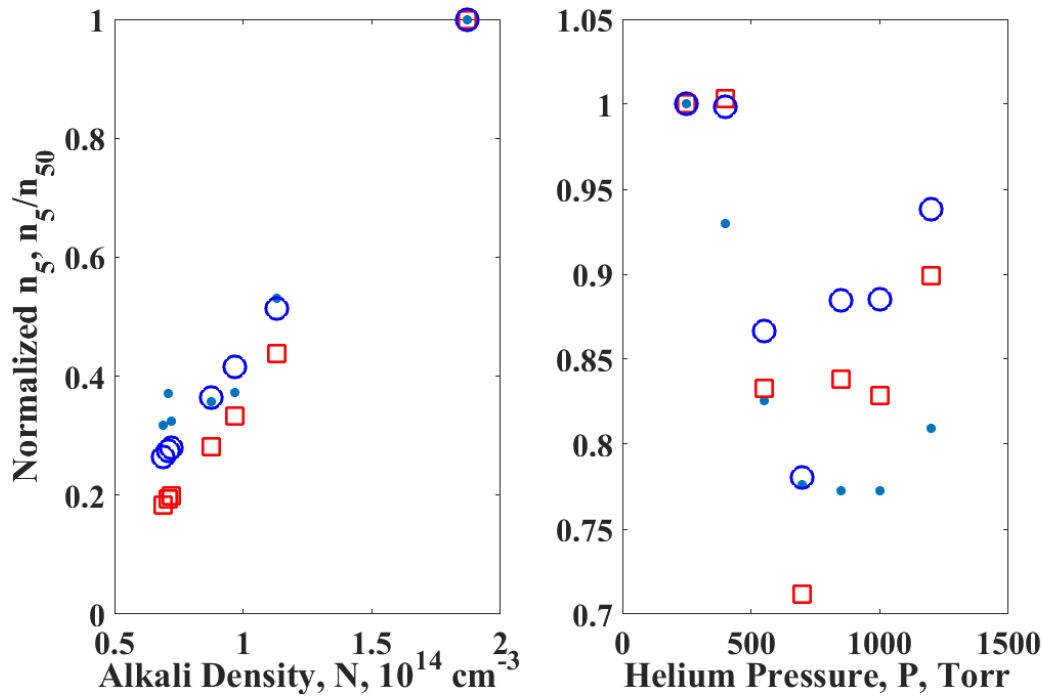
Figure 39. The density in $5\,^2P$ (normalized to the population when $N = 1.87 \times 10^{14}\,cm^{-3}$ and P=250 Torr) as a function of number density (left) and pressure (right). The new prediction suggested here (blue ○) trends with the data (•) much better than the previous values of (70) (red □) at $N = 1.87 \times 10^{14}\,cm^{-3}$.

$151,008\,cm^1$ (3). While ion density likely exists in the cell, it cannot reach an excited state and no fluorescence is observed. Similarly, the ionic dimer may too be present, even though no observed fluorescence is attributed to the ionic dimer. There are currently no potential energy surfaces for the ionic dimer in the literature, it is unclear at what wavelengths the fluorescence spectra from the ionic dimer would be. With adequate estimates of these surfaces, it may be possible to identify this spectra in future studies.

86
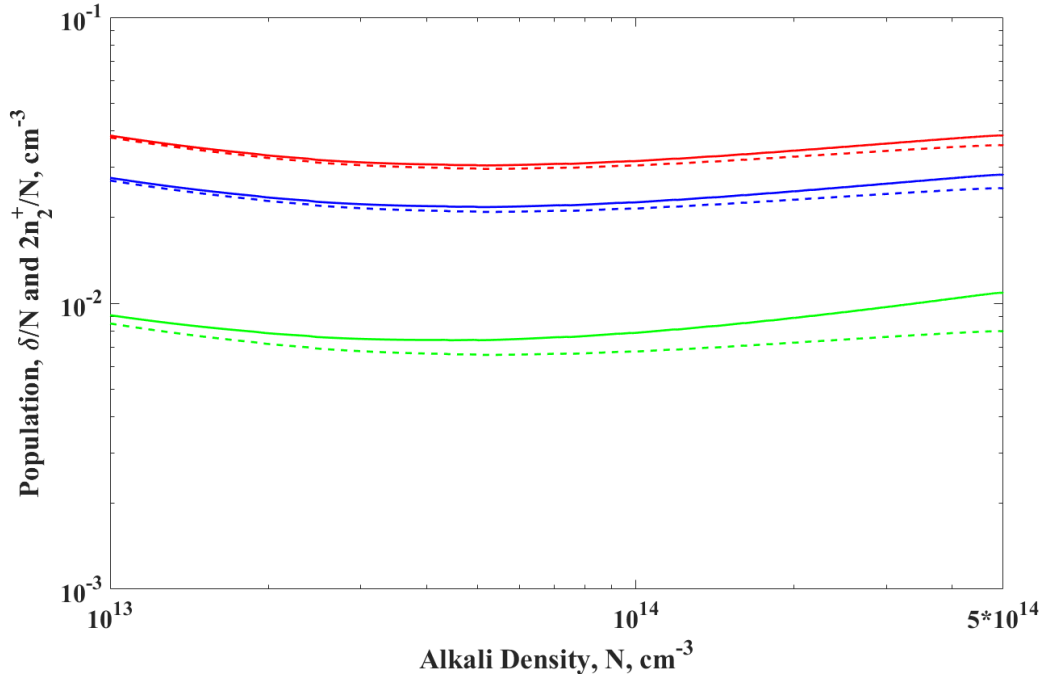
Figure 40. The dimer (–) and δ population (solid) as a function of alkali density for different ion recombination rates: the rate recommended in (70) (blue), half of that rate (red), and 10 times larger (green).

3.5 Conclusion

Florescence spectra from a high power, transverse flow K laser setup (in the absence of lasing) has been analyzed in light of the recent multi-level kinetic DPAL model. The 9-level mechanism is consistent with the observations, if the quenching rates, pooling rates, and wing absorption cross-sections are reasonably adjusted. The scaling with K density suggests a strong wing absorption for the P-D transition. Further validation of this result would be enabled via observations under lasing conditions. The quenching of the intermediate states is moderately fast, $k = 0.11 - 1.11 \times 10^{-11} cm^3/(atom - s)$, with the primary products leading to production of the high lying P states. The comparison of observations and model predictions is adequate, but not fully satisfying, with the scaling of excited state density with K density at higher pressure most problematic. Improved agreement may be achiev-

87

able even within the limits of the present mechanism, by further optimization of the rates, particularly when considering the trade between pooling, wing absorption and Penning ionization. Indeed, the recommended modification to the rate coefficients currently reported must be validated with additional experiments, as the solution is not unique. The current analysis does not consider the role of free electrons, which could significantly alter the conclusions.

IV. Power scaling effects on multi-level kinetics of high power, transverse flow diode pumped potassium vapor laser

Fluorescence emitted by a high power, transverse flow potassium DPAL was collected to characterize the highly excited state population for pump intensities of $I_p = 20 - 60 \, kW/cm^2$ in buffer gas of pure helium and containing methane. The new observations are compared to previous fluorescence data and discrepancies in the two are identified and resolved. The effects of methane on higher state density is discussed and the model is updated with new rates for the inclusion of methane.

4.1 Introduction

A nine level kinetic mechanism has been formulated to describe the higher lying state populations in a high power Diode Pumped Alkali Laser (DPAL). The primary production mechanisms in this are energy pooling and photo-excitation into the far wings. A full set of kinetic rates has been recommended for both potassium and rubidium in pure helium (70; 79). Prior experiments were under taken to quantify the ratio of energy pooling to far wing absorption and a new set of rates for potassium was presented (80). However, this study neglected the dependence on pump intensity.

Hydrocarbons, such as methane or ethane, are often added to buffer gas to optimize laser output (12). The spin orbit mixing rate is much faster than in pure helium (81) and low pressure systems become possible (82). The current helium rate package would require modification to predict the effects of methane.

In this experiment, more observations from a high power ($\sim$ 1-2 kW), transverse flow potassium laser are compared to the nine level kinetic model. Emission from $\sim$ 30 atomic potassium states with principal quantum number as high as n=13 are observed for a range of pump intensities of $22 - 56 \, kW/cm^2$, in both pure helium and helium-methane buffer gas. These new observations are integrated with the previous

89

ones and the incongruities are explained. The required modifications to the kinetic rate package due to the addition of methane are also analyzed.

4.2   Experimental setup

The flowing potassium DPAL apparatus is similar to the system used in Chapter III, and the new apparatus is shown in Figure 41. This data collection included an additional spectrometer and replaced the output coupler to achieve lasing. The new, 209 McPherson 1.3 meter scanning monochrometer (1,800 gr/mm, 350-800 nm blaze grating) outfitted with a Princeton Instruments, PI-MAX 2 CCD also monitored the visible spectrum, but did so with a much better spectral resolution, 0.0087 nm. It has a bandwidth of ~ 4.2 nm and 30 spectra were required for the range $475 - 600$ nm. A CeramOptec 8325 bundle situated behind the high reflector mirror transmitted the emission to this new spectrometer.
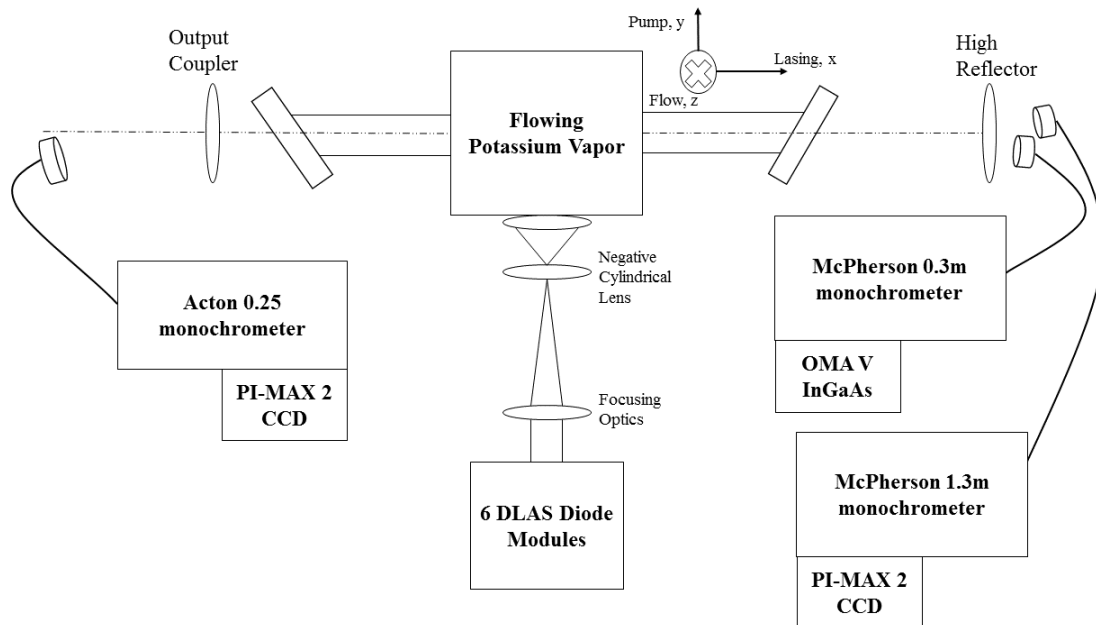
Figure 41. A block diagram of the laser setup used in this experiment.

A comparison of the two spectrometers' observation of sets of lines is shown in

90

Figure 42. The two are normalized such that the peak at 578 nm have the same area. The spectrum from the 1.3 m demonstrates a lower baseline and well defined peaks, so it will be used to compute the densities in the Rydberg states. The Acton spectra detector was placed much further from the laser cell than that for the 1.3 m, so the Acton's response is normalized to the peak at 578 nm for each run to correct for variable viewing volume.
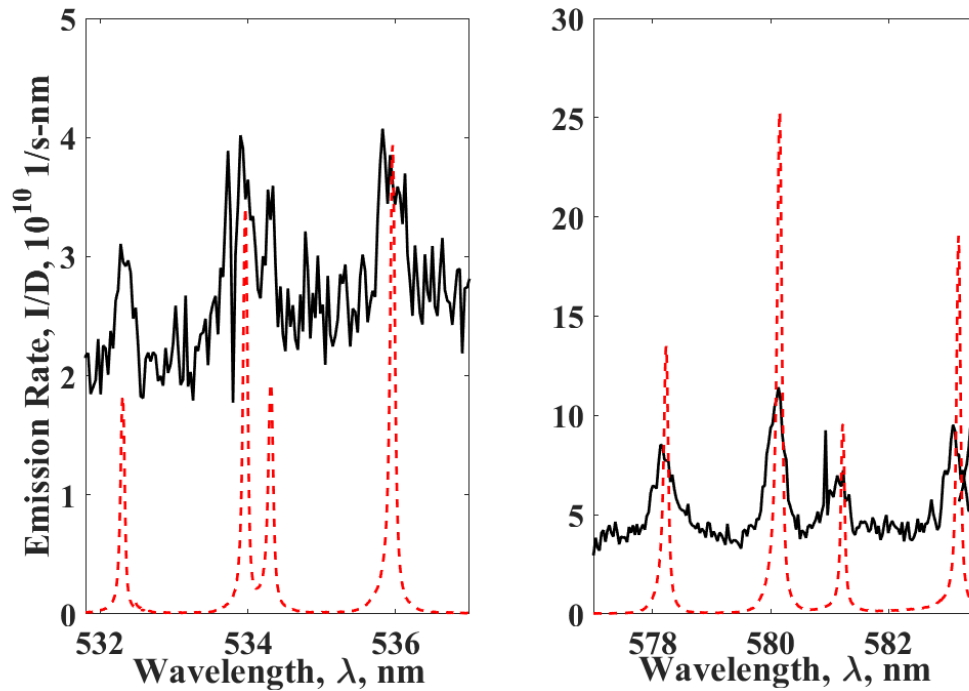
Figure 42. Spectral lines as collected by the Acton (black solid) and 1.3 m McPherson (red −−) spectrometers.

Alkali density was monitored in this experiment in real time. The tunable diode laser absorption introduced in Chapter III has been updated to probe a volume ~ 25 cm beneath the lasing plane. This results in more accurate measurements than the last collection. As in Chapter III, the detector response was chosen by equating the $4\,^2D$ state observed density with that of the model presented in Chapter II, in this case using alkali density of $N = 1.77 \times 10^{14}\,cm^{-3}$, pure helium buffer gas pressure of $P = 450$ Torr, and pump intensity of $I_p = 34.2\,kW/cm^2$, in the absense of lasing.

91

Using these values, we establish $D_t = 4.37 \times 10^{-4}$.

The gas temperature was measured 4.75 cm above and below the center of gain region. Before the gain medium is measured using an Omega TMQSS-125G-6 K-type thermocouple and after with an Omega TMQSS-125G-6 T-Type thermocouple. Temperatures are collected every 0.3 seconds during the duration of the experiment. All other measurements are kept the same, including flow speeds and pump beam focus.

This experiment was undertaken in June 2018. Over 35 full bandwidth spectra was collected with pump laser intensities ranging from $I_p = 22.4 - 56.0 \, kW/cm^2$. Pure helium and helium-methane buffer pressure was varied from 250 to 1,200 Torr. The alkali density in the cell ranged between $N = 0.83 - 19.4 \times 10^{13} \, cm^{-3}$. No attempt optimal cavity was taken, however weak lasing still occurred with lasing power $P_l = 5 - 100 \, W/cm^2$.

4.3 Results

4.3.1 Laser Performance.

Laser intensity is plotted as a function of pump intensity in Figure 43, for both pure helium and helium-methane buffer gas mixtures. Laser performance was not the purpose of this investigation, so little cavity optimization was done. This manifests as poor mismatch of the pump and laser volume, as well as poor focus of the pump beam. Using a pump area of $A_p = 0.3 \, cm^2$ and lasing area of $A_l = 0.046 \, cm^2$ the broadband three level model presented in (15) can accurately match the data. The diodes are quoted as Gaussian with $\sim 0.5 \, nm$ bandwidth. This output power prediction is also shown in Figure 43. The addition of methane to the cell greatly enhances lasing and may be due an apparent decrease in alkali density in the pump laser path with just helium. The heat capacity of methane is larger than helium, and it is significantly

92

more massive, therefore experiencing slower diffusivity. It requires more heat to raise the temperature and more time for the alkali to diffuse out of the beam path when methane is added. An alkali density decrease of 60% in the pure helium buffer gas is required to match the three level model to the observations.
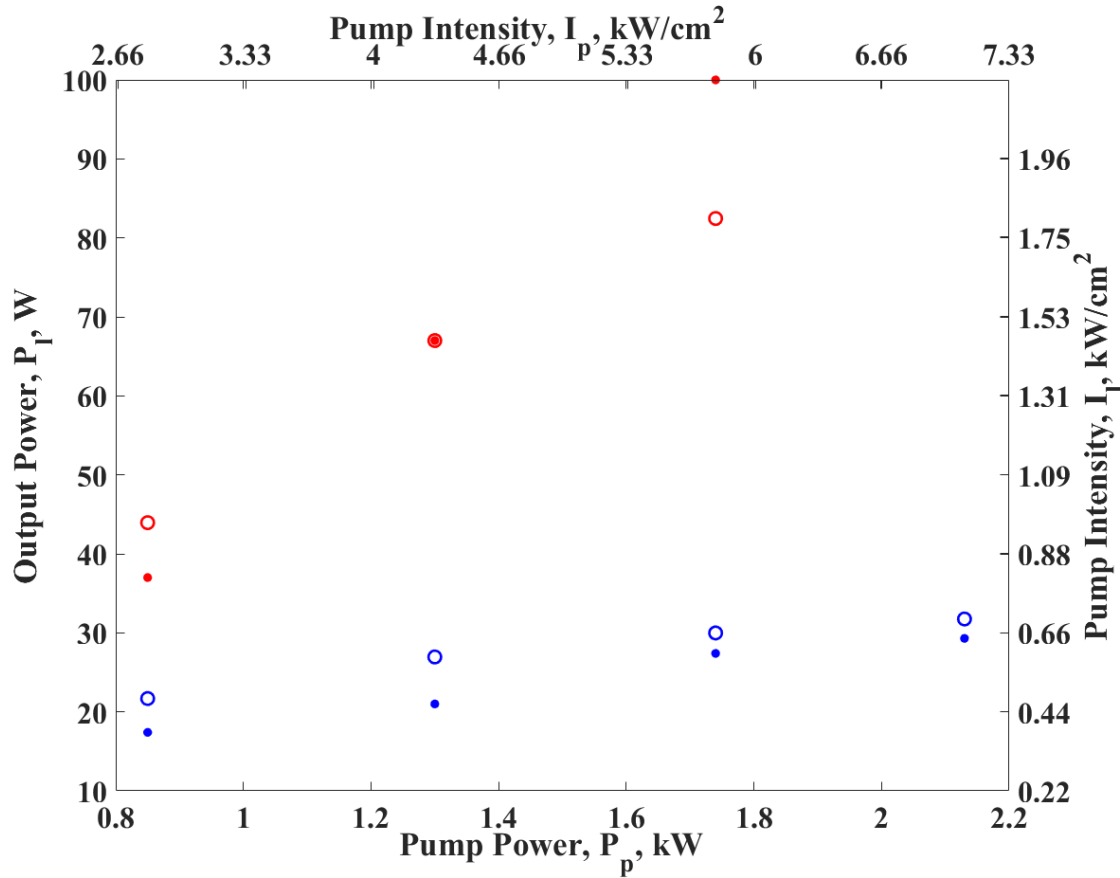
Figure 43. Observed (●) and predicted (○) laser intensity as a function of pump intensity, for pure helium (blue) and helium-methane (red). The alkali density is $N = 3.3 \times 10^{13} cm^{-13}$ for the methane case and a pressure P= 450 Torr. The pump laser has an assumed 0.5 nm bandwidth. The pump area and lasing area are $A_p = 0.3 \, cm^2$ and $A_l = 0.046 \, cm^2$ respectively. A decrease in the number density by 60% is required to match the observations in pure helium.

4.3.2   Fluorescence Spectra.

With the new, longer spectrometer is capable of resolving an additional 8 atomic lines in potassium. These lines and their associated A-coefficients are shown in Table

93

10. The dependence on pump intensity is shown in Figure 44. The intensity of all lines grows with pump intensity, but this trend is very sensitive to number density and tends to be most prominent at low alkali densities.

Table 10. Observed atomic K transitions with A-coefficients (3) and fit intensity amplitude for test conditions $N = 1.87 \times 10^{14}\,cm^{-3}$**, P= 450 Torr and** $I_p = 2.24\,kW/cm^2$**.**

Upper State, i	Lower State, j	λ_{ij}, nm	A_{ij}, $10^5\,s$	Observed Intensity	Intensity Uncertainty
$13^2\,S_{\frac{1}{2}}$	$4^2\,P_{\frac{1}{2}}$	474.09	0.80	6.38×10^{12}	4.5×10^{11}
$11^2\,D_{\frac{3}{2}}$	$4^2\,P_{\frac{1}{2}}$	474.43	0.98	1.36×10^{13}	4.5×10^{11}
$13^2\,S_{\frac{1}{2}}$	$4^2\,P_{\frac{3}{2}}$	475.39	1.60	1.00×10^{13}	4.7×10^{11}
$11^2\,D_{\frac{3}{2}}$	$4^2\,P_{\frac{3}{2}}$	475.74	1.90	2.40×10^{13}	5.9×10^{11}
$11^2\,D_{\frac{5}{2}}$	$4^2\,P_{\frac{3}{2}}$	475.74	1.20		
$12^2\,S_{\frac{1}{2}}$	$4^2\,P_{\frac{1}{2}}$	478.65	1.03	6.95×10^{12}	4.9×10^{11}
$10^2\,D_{\frac{3}{2}}$	$4^2\,P_{\frac{1}{2}}$	479.10	1.30	1.82×10^{13}	5.4×10^{11}
$12^2\,S_{\frac{1}{2}}$	$4^2\,P_{\frac{3}{2}}$	479.98	2.07	1.64×10^{13}	5.3×10^{11}
$10^2\,D_{\frac{3}{2}}$	$4^2\,P_{\frac{3}{2}}$	480.43	0.26	3.89×10^{13}	6.7×10^{11}
$10^2\,D_{\frac{5}{2}}$	$4^2\,P_{\frac{3}{2}}$	480.43	1.60		

A summary of the data is presented in Figure 45, the intermediate density as a function of pump intensity. As intensity is increased, the intermediate density is mostly unchanged. This indicates that wing absorption is the dominant production mechanism. As helium pressure increases from $P = 450$ Torr (red) to 850 Torr (blue) the intermediate density is increased by a factor of ~ 3. This is unexpected, as pressure decreased the intermediate density in the previous study, in Chapter III, also annotated on the figure as pentagrams ($\star$) for similar alkali density and helium pressures. An attempt to explain this discrepancy is presented below. The addition of

94
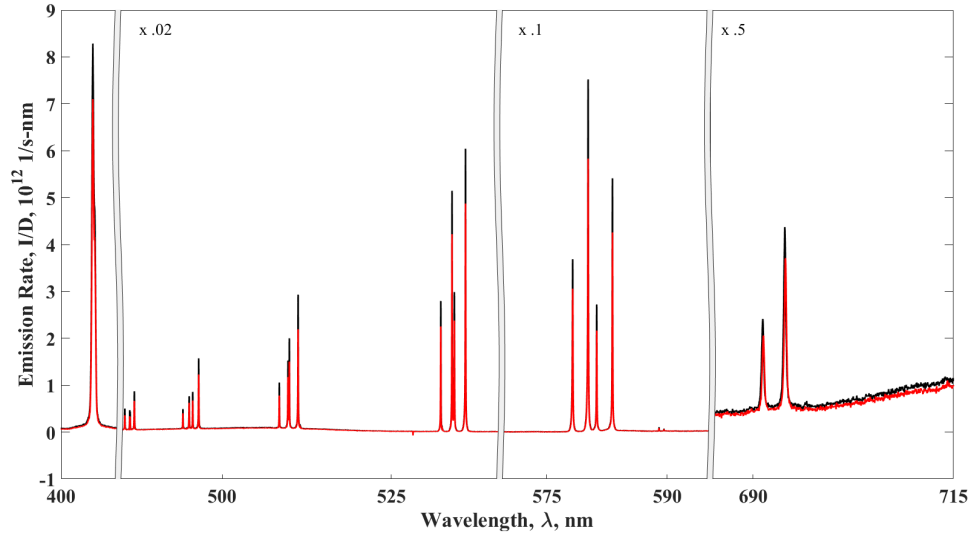
Figure 44. The fluorescence of the lines goes up with pump intensity. The pump intensity of the red curve is $22.3\,kW/cm^2$ and the black represent an intensity of $34.2\,kW/cm^2$ with pure helium buffer gas at a pressure of 450 Torr and an alkali density of $3.43 \times 10^{13}\,cm^{-3}$.

methane greatly decreases the alkali density, by a factor of over 100, shown in green. This result does not indicate that the addition of methane greatly decreases the adverse effects of multi-level kinetics. The density in the higher states is also almost negligible with just helium. The addition of methane cannot increase performance, as it is minimally effected in the first place.

The observed density in the intermediate states is shown as a function of pump intensity in Figures 46-57. Figures 46-48 illustrate this comparison for $N \sim 2 \times 10^{13}\,cm^{-3}$. For these low density cases the $5\,^2P$ and $6\,^2S$ states are well described by the prediction, but the $4\,^2D$ is over estimated.

The same plots for the higher density cases, $N \sim 1 \times 10^{14}\,cm^{-3}$ are shown are Figures 49-51. The model does a very poor job of predicting the data for all intermediate states. The unexpected pressure dependence is exhibited for only the $4\,^2D$ and $6\,^2S$, where increasing pressure causes an increase in the intermediate density. This trend is not observed for the $5\,^2P$ density, where the model over estimates the data

95
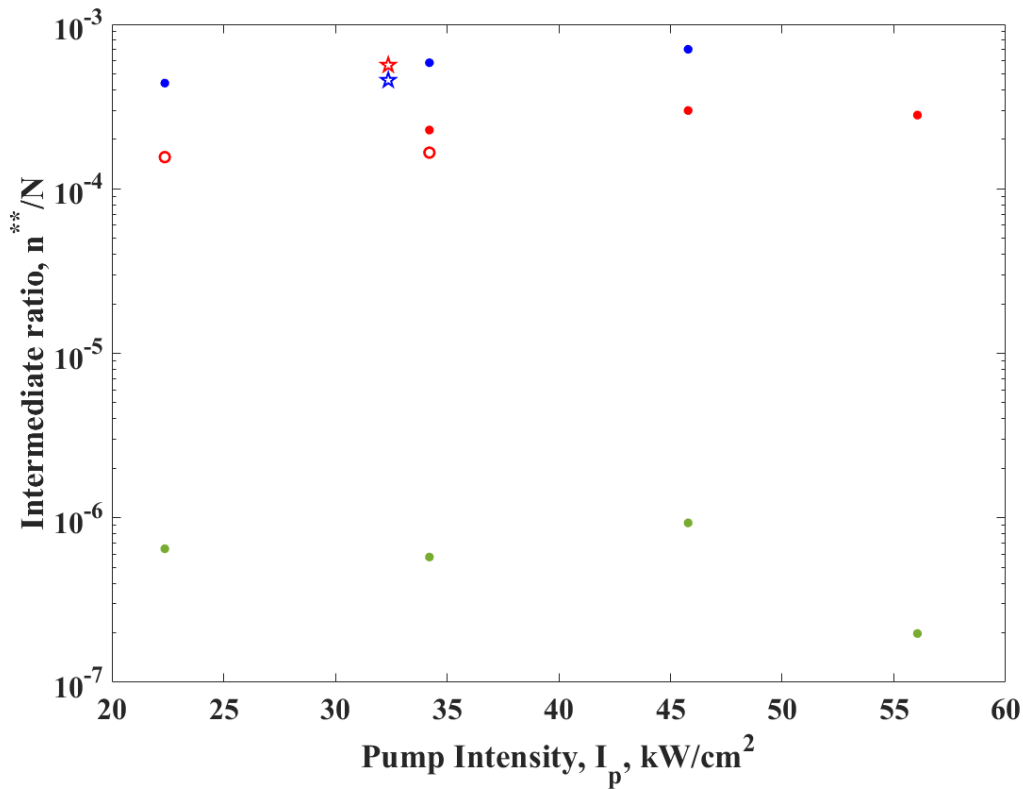
Figure 45. Observed intermediate density as a function of intensity at $N \approx 1.5 \times 10^{14} cm^{-3}$ for no lasing (○) and weak lasing (●), at P= 450 (red) and 850s Torr (blue) of pure helium buffer gas, and P= 450 Torr of 6.7% methane buffer gas (green). The results from Chapter III are shown in ⋆.

for both pressures.

The Rydberg density observed in shown in Figures 52, 53, and 58. The same trends observed in the other energy states are seen here as well: the Rydberg density is under estimated at low alkali density and increase with pressure at high alkali density. The Rydberg density is dependent on the intermediate densities, so it is expected that the trends are similar.

96

Figure 46. The observed ($\bullet$) and predicted ($\circ$) density in the $5\,^2P$ state as a function of pump intensity at $N \sim 2 \times 10^{13}\,cm^{-3}$ with helium pressures of **P**= 450 (black) and 850 (blue) Torr. The model presented in (80) is used to calculate the intermediate prediction.

97

Figure 47. The observed (●) and predicted (○) density in the $4\,^2D$ state as a function of pump intensity at $N \sim 2 \times 10^{13}\,cm^{-3}$ with helium pressures of P=450 (black) and 850 (blue) Torr. The model presented in (80) is used to calculate the intermediate prediction.

Figure 48. The observed (●) and predicted (○) density in the $6\,^2S$ state as a function of pump intensity at $N \sim 2 \times 10^{13}\,cm^{-3}$ with helium pressures of **P**= 450 (black) and 850 (blue) Torr. The model presented in (80) is used to calculate the intermediate prediction.

Figure 49. The observed (●) and predicted (○) density in the $5\,^2P$ state as a function of pump intensity at $N \sim 1 \times 10^{14}\,cm^{-3}$ with helium pressures of **P**= 850 (blue) without lasing, and **P**= 450 with (red) and without (black) lasing. The model presented in (80) is used to calculate the intermediate prediction.
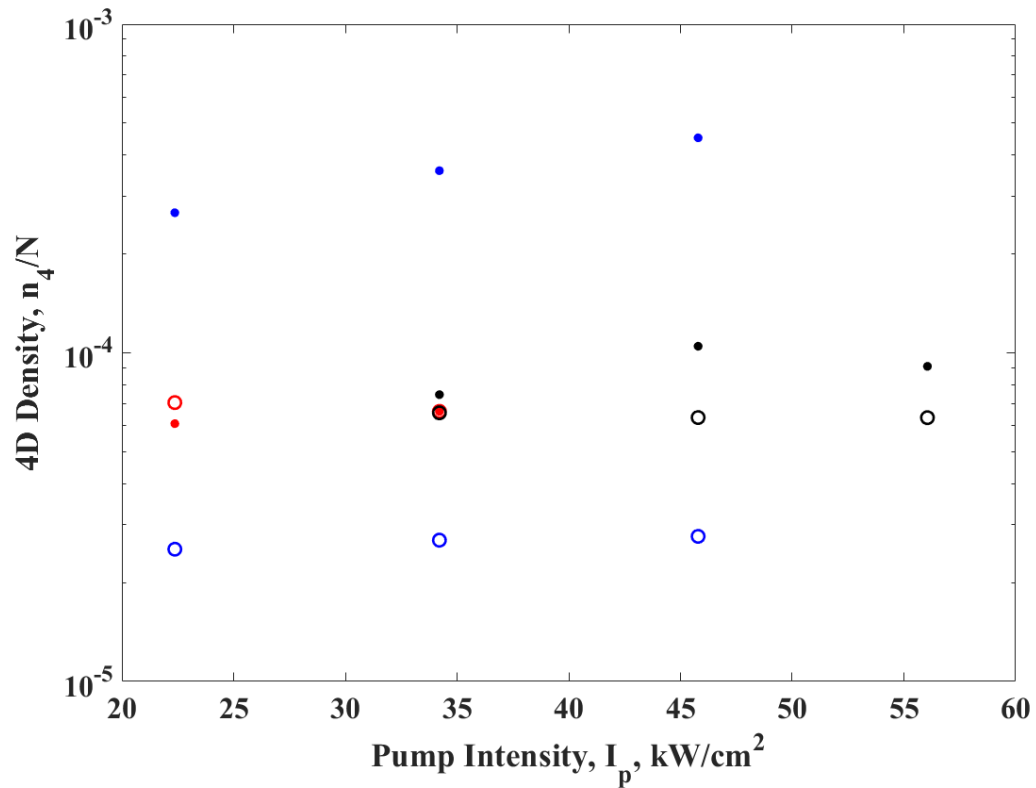
Figure 50. The observed (●) and predicted (○) density in the $4\,^2D$ state as a function of pump intensity at $N \sim 1 \times 10^{14}\, cm^{-3}$ with helium pressures of $\mathbf{P} = 850$ (blue) without lasing, and $\mathbf{P} = 450$ with (red) and without (black) lasing. The model presented in (80) is used to calculate the intermediate prediction.
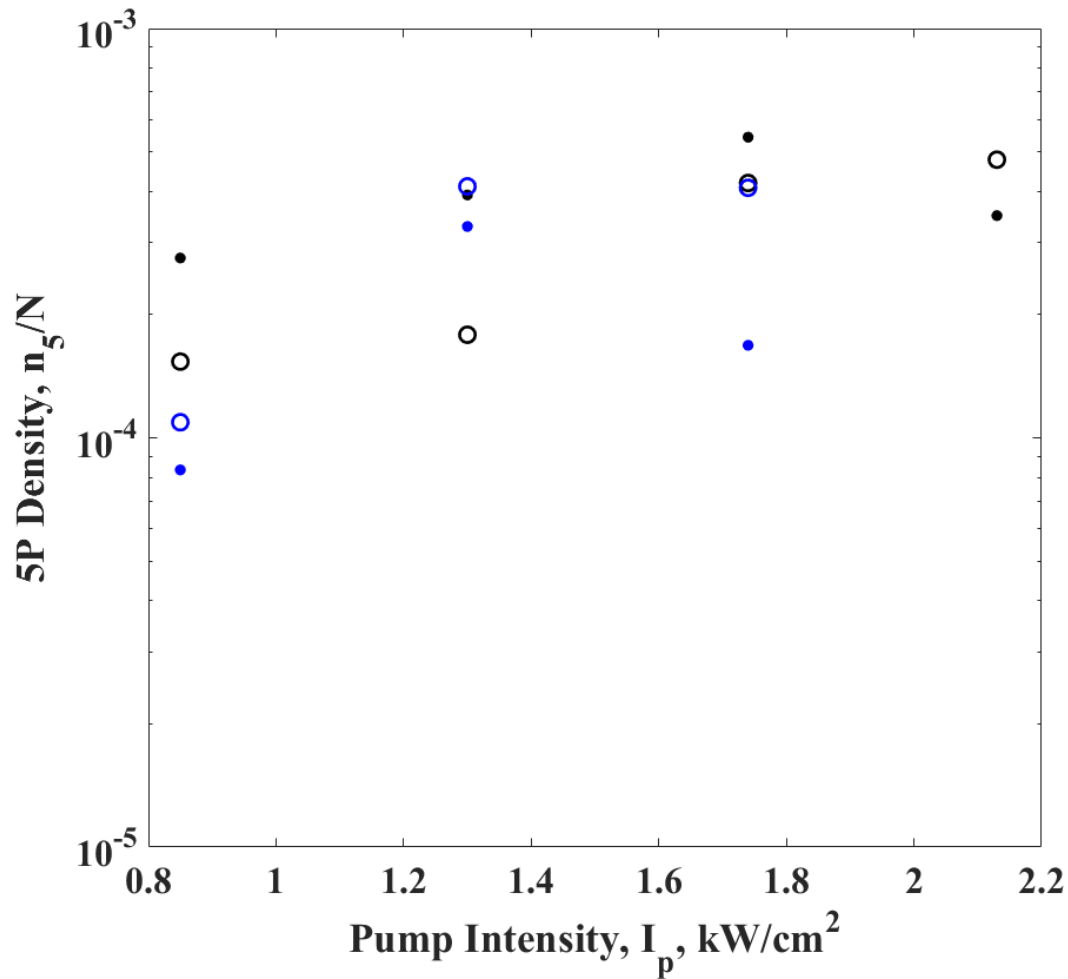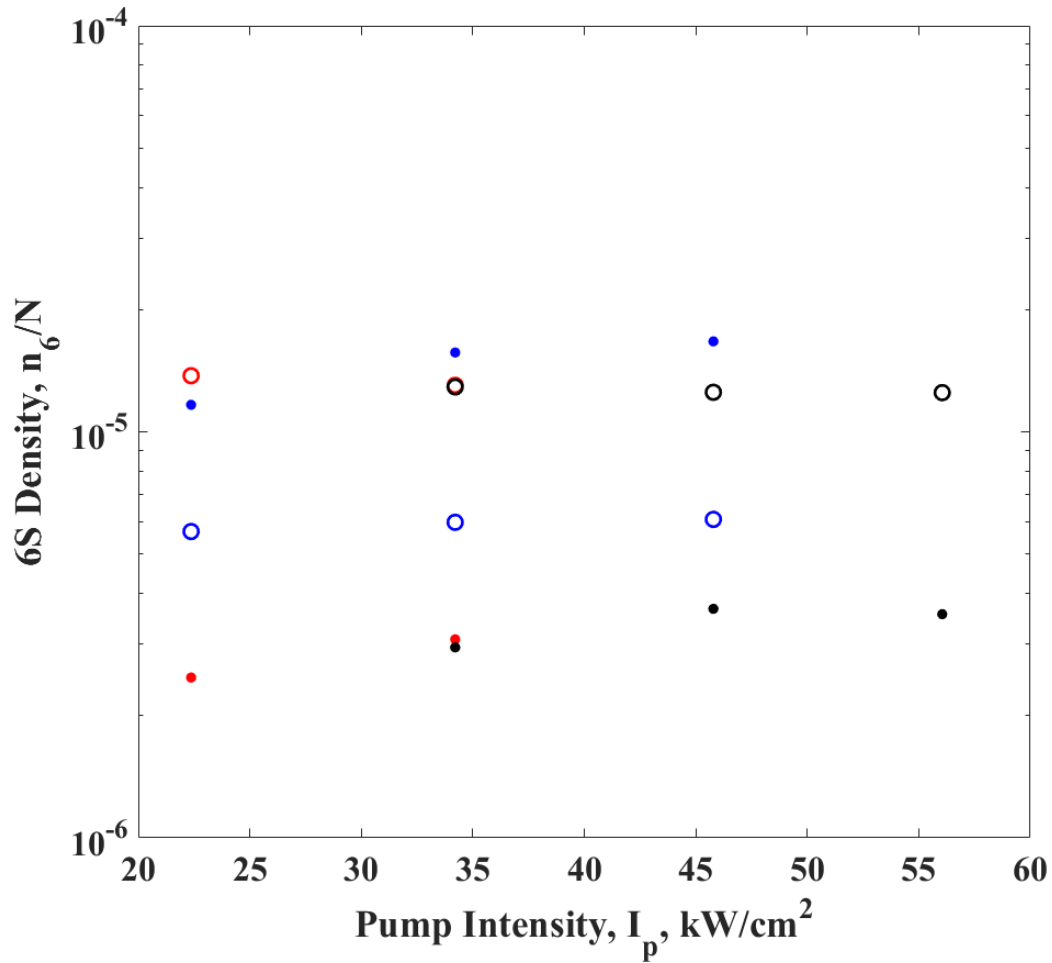
Figure 51. The observed (●) and predicted (○) density in the $6\,^2S$ state as a function of pump intensity at $N \sim 1 \times 10^{14}\,cm^{-3}$ with helium pressures of $\mathbf{P}=850$ (blue) without lasing, and $\mathbf{P}=450$ with (red) and without (black) lasing. The model presented in (80) is used to calculate the intermediate prediction.
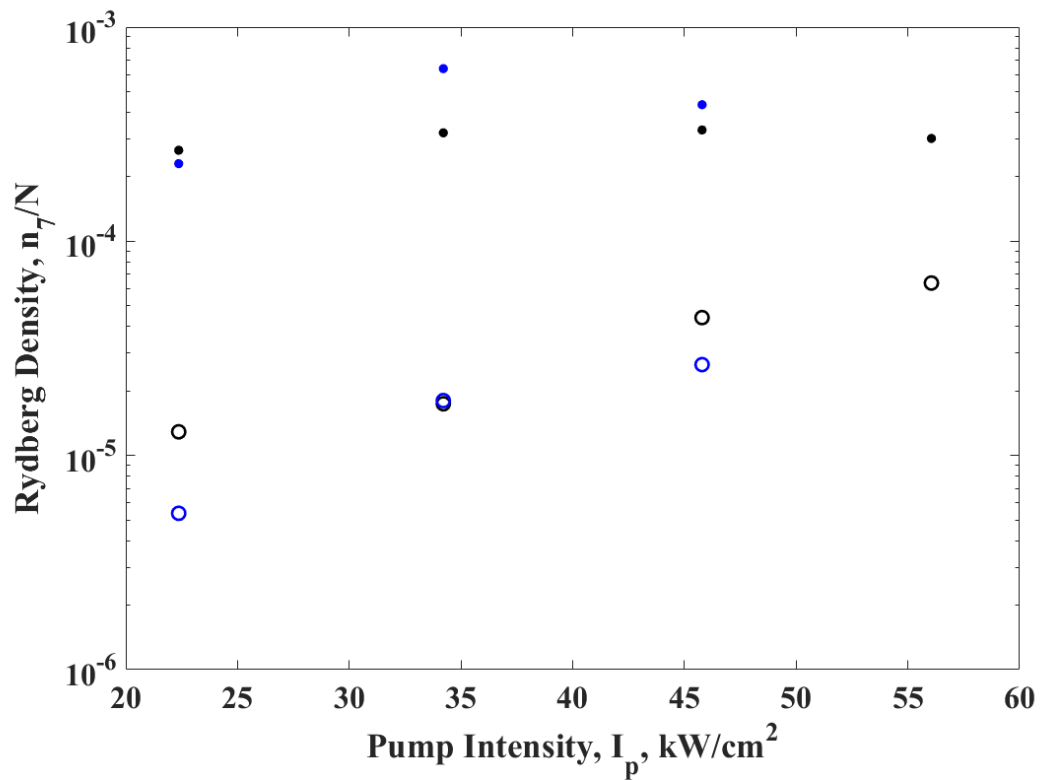
Figure 52. The observed (•) and predicted (○) density in the Rydberg states as a function of pump intensity at $N \sim 2 \times 10^{13} \, cm^{-3}$ with helium pressures of **P**= 450 (black) and 850 (blue) Torr. The model presented in (80) is used to calculate the intermediate prediction.
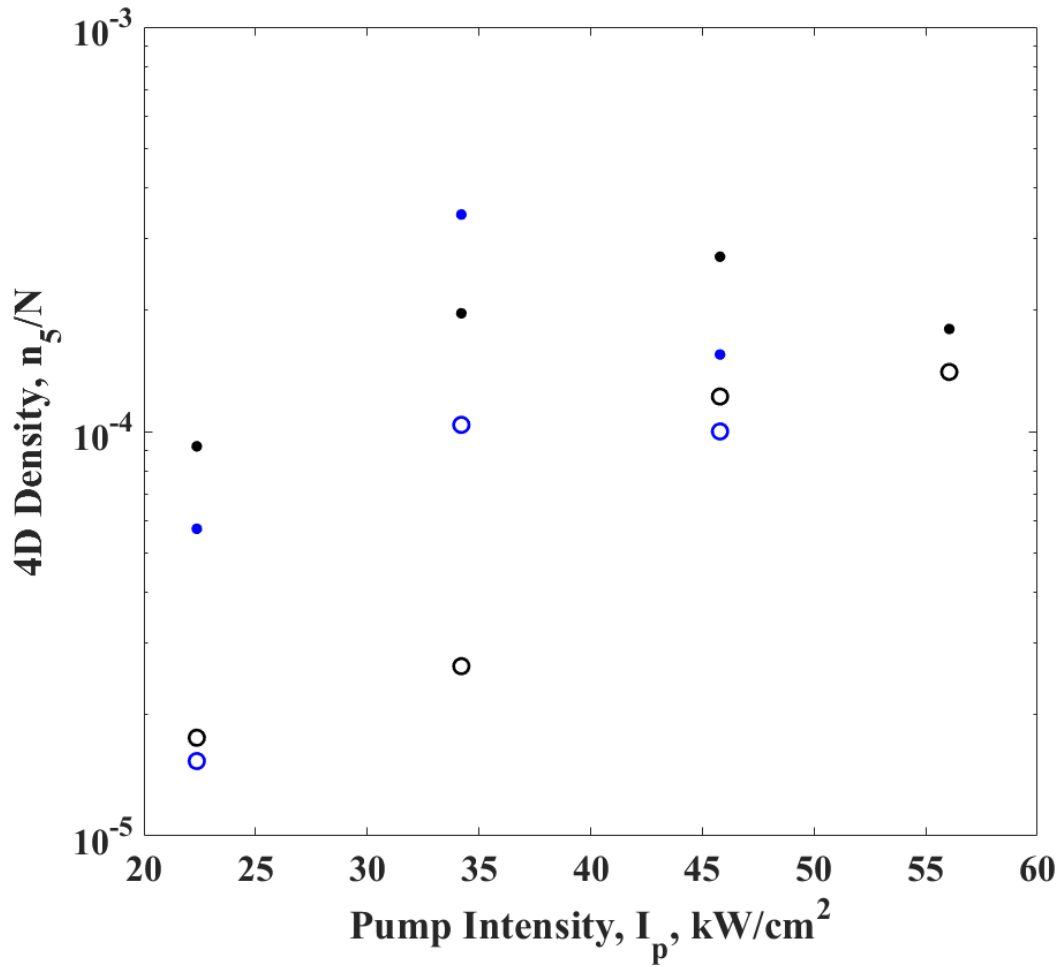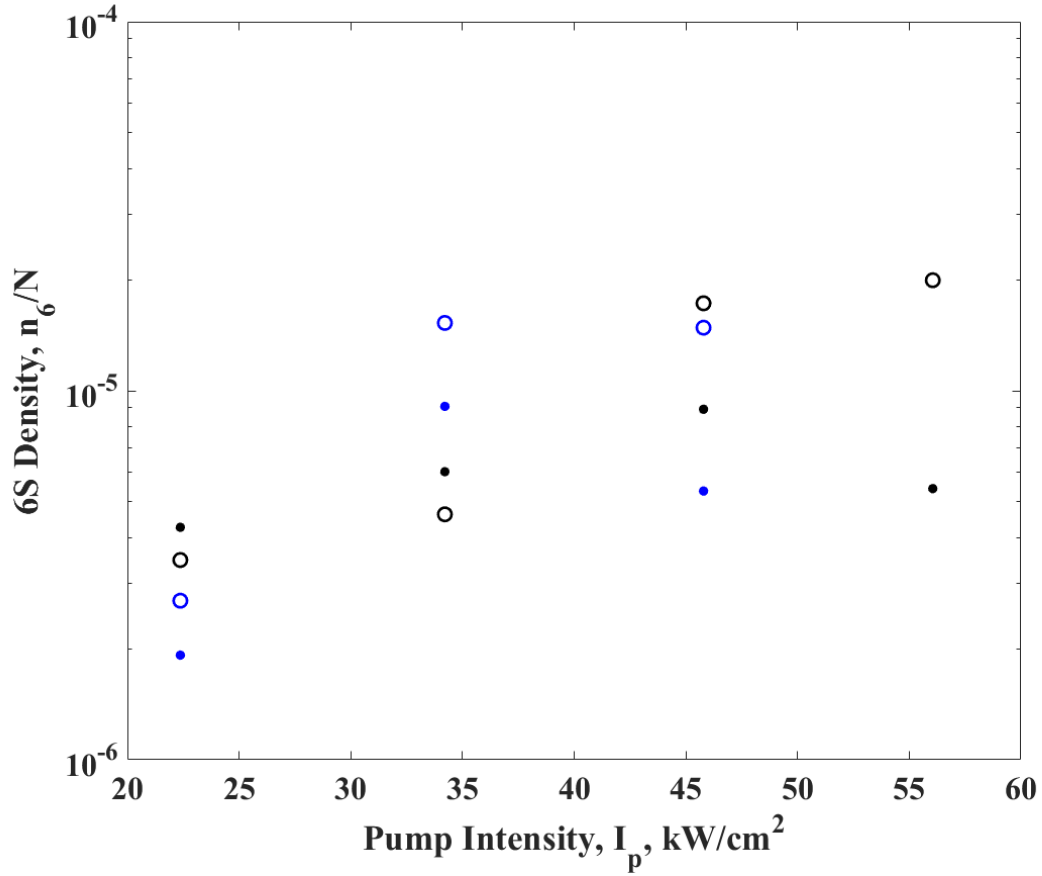
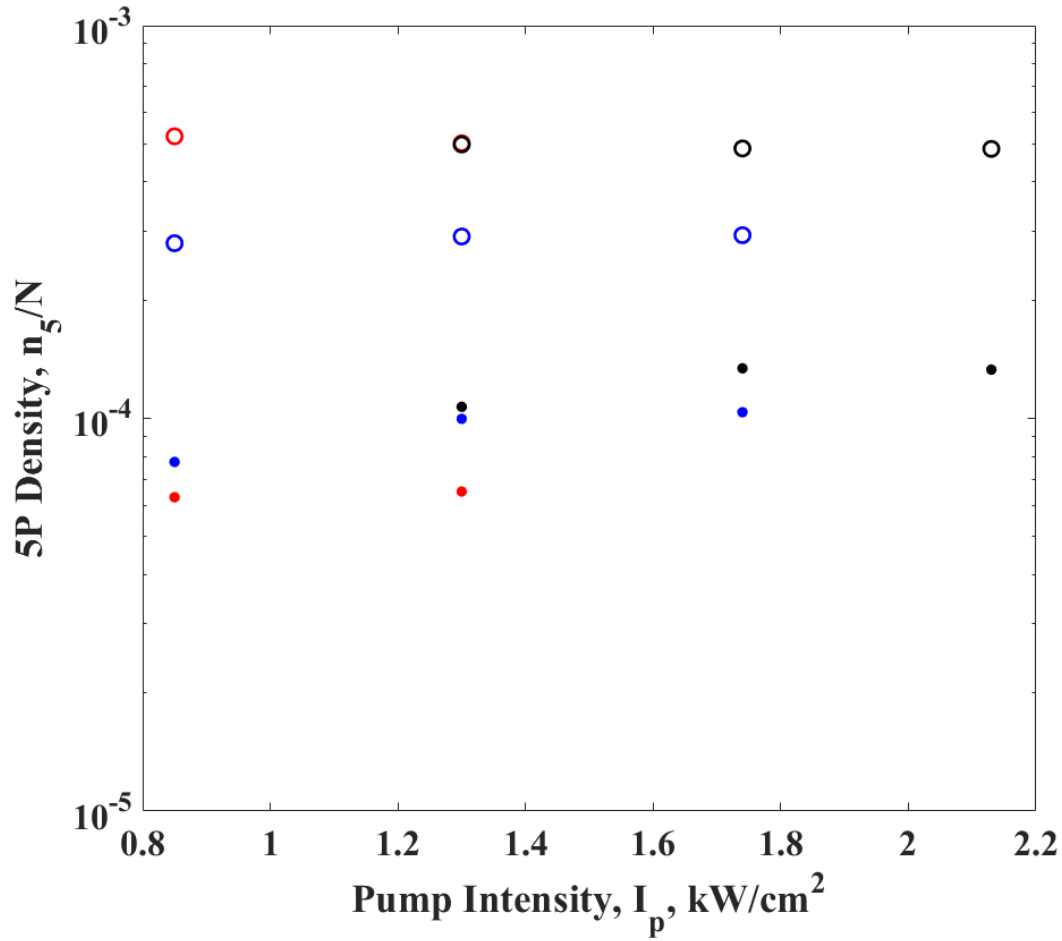Figure 53. The observed (●) and predicted (○) density in the Rydberg states as a function of pump intensity at $N \sim 1 \times 10^{14} \, cm^{-3}$ with helium pressures of **P**= 850 (blue) without lasing, and **P**= 450 with (red) and without (black) lasing. The model presented in (80) is used to calculate the intermediate prediction.

Only a few conditions could have changed between the previous and current study to explain the population discrepancies: detector response stability, number density diagnostic accuracy, diode spectral intensity, and cell contamination.

Density calculation is extremely sensitive to detector response, and even small changes can greatly effect the observed density. If this value was changed day-to-day or between collections, the intermediate populations would vary together. This is not observed as the $4\,^2D$ and $6\,^2S$ populations are under estimated by the model and the $5\,^2P$ density is overestimated.

The TDLAS diagnostic was used in real time; the alkali density was likely more accurate in this experiment. Additionally the alkali density required for the model to correctly predict the $4\,^2D$ density in Figure 50 is too large to be reasonable, so it is unlikely number density accuracy is causing the observed trends.

The diode bars used during this collection were not the same as used previously. They may exhibit different spectral intensities, especially in the far wings, drastically changing the wing absorption rate. If this increase were severe enough, the $4\,^2D$ and $6\,^2S$ could increase with pressure. However, this explanation can to be discounted as Figures 46-58 show only a marginal dependence of excited state population with pump intensity.

Cell contamination would result in an higher apparent helium quenching rate, molecular species, such as nitrogen and methane have larger quenching rates than helium. The excess contamination in the cell would manifest additional temperature rise across the pumped volume. Thermocouples measured the gas temperature a few cm before and after the pump region. The temperature rise across the gain length for different lasing conditions are shown in Table 11. The previous experiment saw temperature rises of $250 - 400$ K, while this test had increases < 100 K. This could explain the over estimation of the $5\,^2P$ density, as the $5\,^2P$ state is populated through

105

quenching of the other two intermediate levels. Figures 54 and 55 demonstrate a new prediction with quenching rates lessened to best match the $5\,^2P$ data, $k^q_{new} = 0.05 k^q_{old}$.

The quenching rate of n_2 and n_3 with molecular nitrogen is $k_{N_2} = 1.47 \times 10^{-10}$ $cm^3/(atom-s)$. If this value is used for the quenching of the intermediate states due to contaminants, 0.71% of the buffer gas must be contaminants in order to support this modification. It is likely that the quenching of the intermediates happens faster than that of n_2 and n_3, however gas kinetic rates are on the order of 10^{-10}, so it is unlikely that the intermediate quenching rate is elevated by that much. The additional temperature rise shown in Table 11 is commensurate with this additional quenching.

Table 11. Heat rise across the beam path

Experiment Date	Alkali Density, N, cm^{-3}	Buffer Gas Pressure, P, Torr	Pump Intensity, I, kW/cm^2	Percent Methane	Temperature Rise, K	Transmitted Power, W
March 2017	1.87×10^{14}	400	37.4	0	359.5	410
March 2017	1.87×10^{14}	850	37.4	0	359.5	425
March 2017	1.87×10^{14}	850	37.4	6.7	250.2	465
June 2018	1.70×10^{14}	450	34.2	0	53.5	775
June 2018	1.20×10^{14}	850	34.2	0	168.2	600
June 2018	0.48×10^{14}	850	34.2	6.7	47.7	280

This increased temperature rise may be due to other factors though. The absence of lasing, as in the March experiments, can create a increase in fluorescence heating, where the spontaneous emission is absorbed by the gas or the wall, and increases the temperature. However this difference is likely insignificant, as the total energy released in fluorescence is nearly the same as the spin orbit mixing rate, $Q \approx 67$ W. The rise in temperature increase can be due to different thermocouple locations in the cell. The thermocouple distance to the wall can create different dependency of the wall temperature on these measurements. However, Table 11 also shows the power transmitted through the cell during the data collection. More power was transmitted in these newer experiments, which is consistent with the picture presently described; an increase in quenching will allow for an increase in power absorbed.

Using new values for intermediate quenching, the density in the high P state is

now adequately described using the model. However, it is impossible to increase density with pressure simply by decreasing quenching; cell contamination still does not explain this unusual trend.

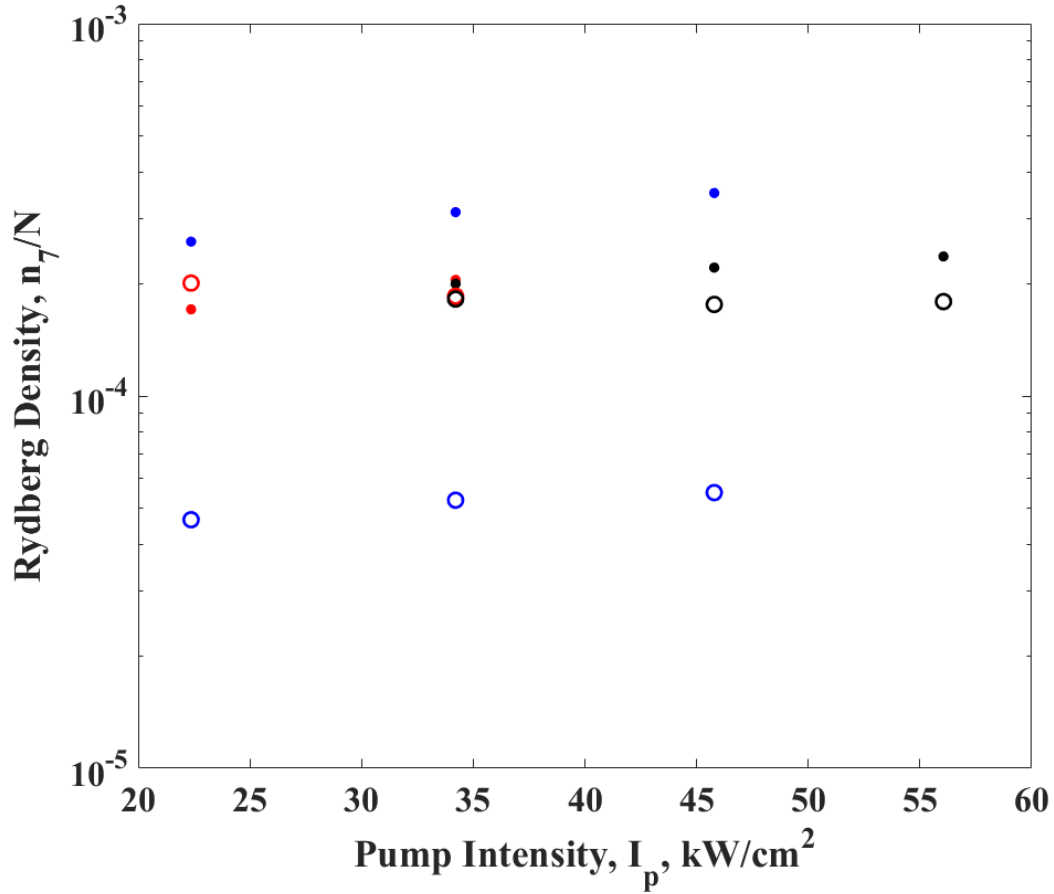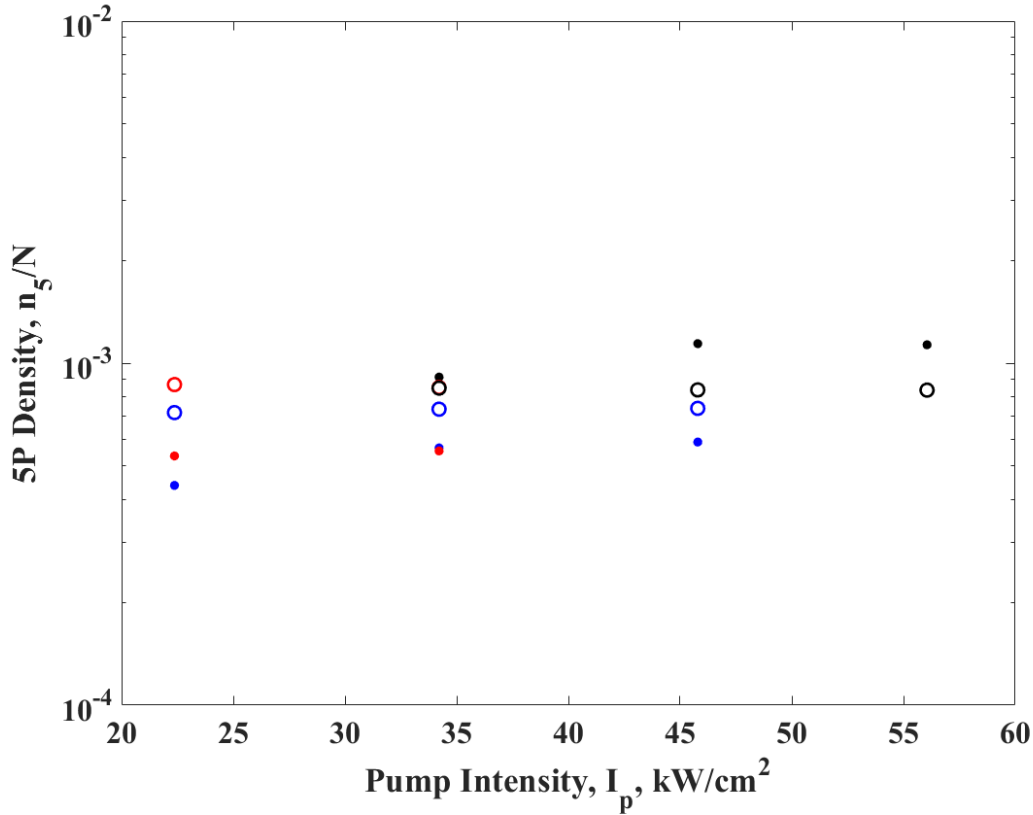**Figure 54. The observed (•) and predicted (○) density in the $5\,^2P$ state as a function of pump intensity at $N \sim 1 \times 10^{14}\,cm^{-3}$ with helium pressures of P= 850 (blue) without lasing, and P= 450 with (red) and without (black) lasing. All intermediate quenching rates have been updated commensurate with a cleaner cell.**

Detector response stability, number density diagnostic accuracy, diode spectral intensity, and cell contamination have systematically been eliminated as the source for the increase intermediate density with pressure. While the presented mechanism can largely express all of the data collected in both experiments, unfortunately, no universal kinetic rate package can allow for this single anomalous point, while still accurately predicting the rest of the observations.

Spectra was also collected with the addition of methane. Methane greatly reduces

107
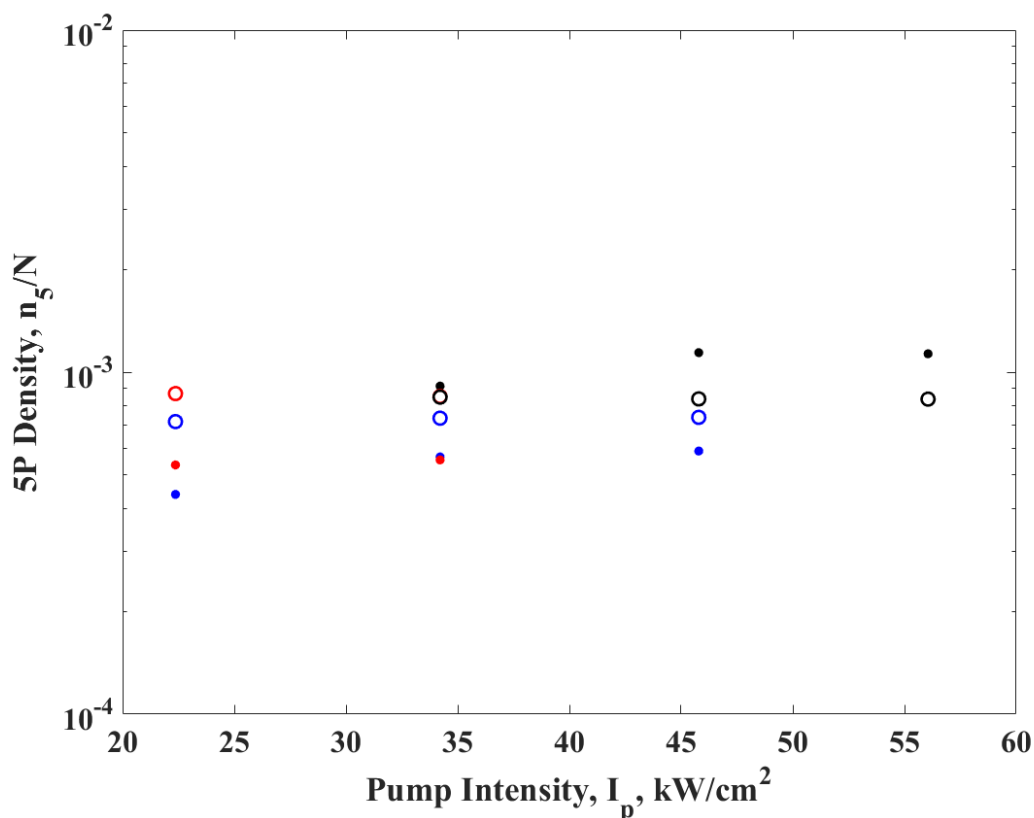
Figure 55. The observed (●) and predicted (○) density in the $4\,^2D$ state as a function of pump intensity at $N \sim 1 \times 10^{14}\,cm^{-3}$ with helium pressures of P= 850 (blue) without lasing, and P= 450 with (red) and without (black) lasing. All intermediate quenching rates have been updated commensurate with a cleaner cell.

the densities in all higher excited states, demonstrated in Figures 56-58. The density in the $5\,^2P$ and $4\,^2D$ is nearly cut by a factor of 100, and the fluorescence from the $6\,^2S$ state is not bright enough to be distinguished. The intermediate population grows at similarly with and without methane. The potential energy surfaces associated with the alkali-methane collision are different from those associated with alkali-helium. The absorption cross section, especially in the far wings, will be distinct for the two collision partners. However, even with the addition of methane, far wing absorption is not dominant over energy pooling, especially at high alkali densities.

Modifying the quenching rates is all that is required to match the methane observations to the model, as shown in Figures, 56 and 57. Here, the quenching rates are

108

8 times larger than the rates recommended in Chapter III, or 160 times larger than the pure helium quenching rates derived above.
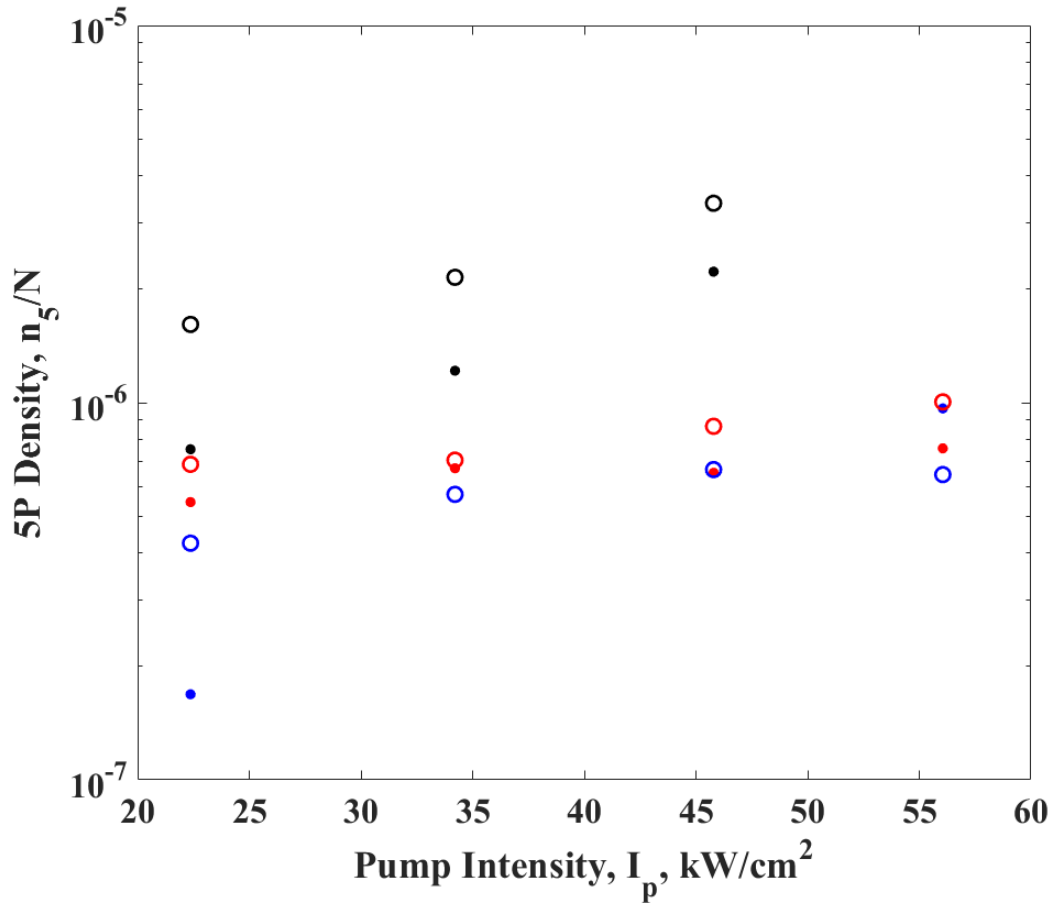
Figure 56. The observed (●) and predicted (○) density in the $5\,^2P$ state as a function of pump intensity in a 6.7% methane buffer gas, in the presence of very weak lasing, $I_l = 100\,W/cm^2$. The black dots represent $N \sim 1 \times 10^{13}\,cm^{-3}$, **P= 450 Torr, red is** $N \sim 5 \times 10^{13}\,cm^{-3}$, **P= 450 Torr, and blue has** $N \sim 6 \times 10^{13}\,cm^{-3}$, **P= 850 Torr.**
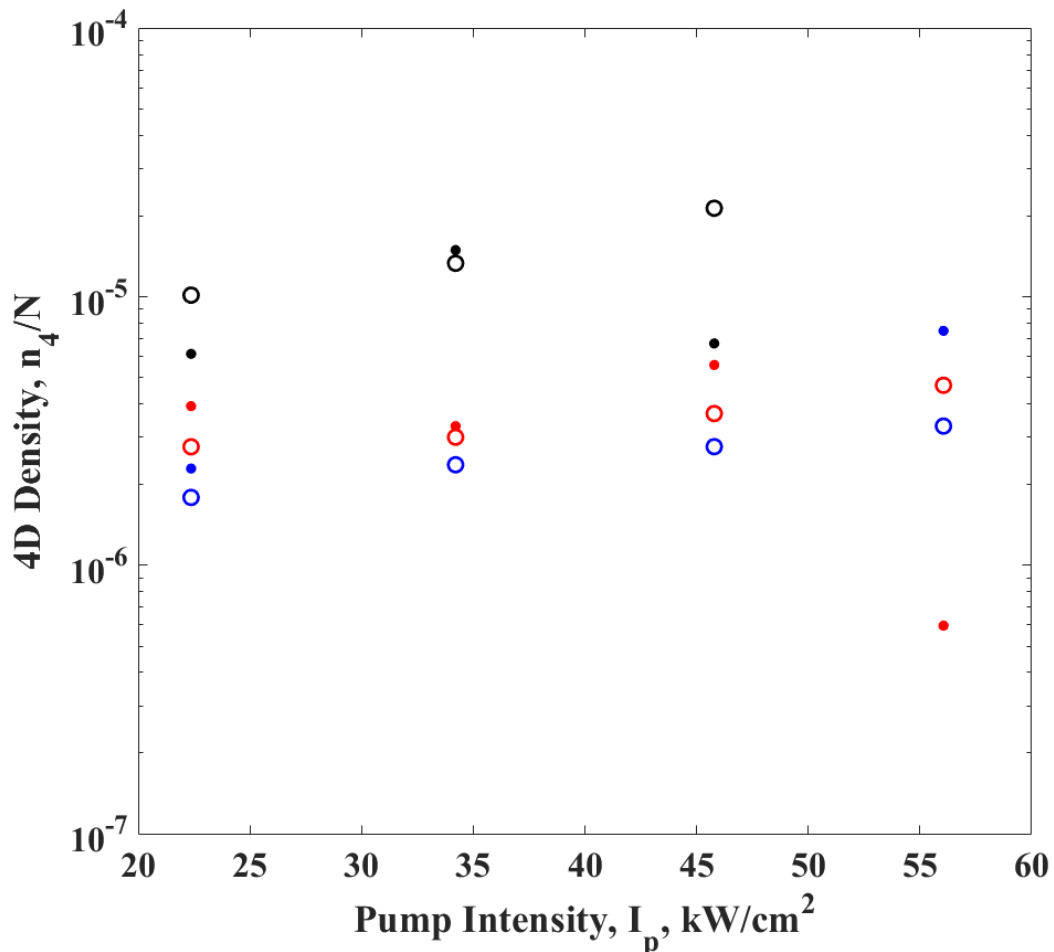
Figure 57. The observed (•) and predicted (∘) density in the $4\,^2D$ state as a function of pump intensity in a 6.7% methane buffer gas, in the presence of very weak lasing, $I_l = 100\,W/cm^2$. The black dots represent $N \sim 1 \times 10^{13}\,cm^{-3}$, **P= 450 Torr**, red is $N \sim 5 \times 10^{13} cm^{-3}$, **P= 450 Torr**, and blue has $N \sim 6 \times 10^{13} cm^{-3}$, **P= 850 Torr.**
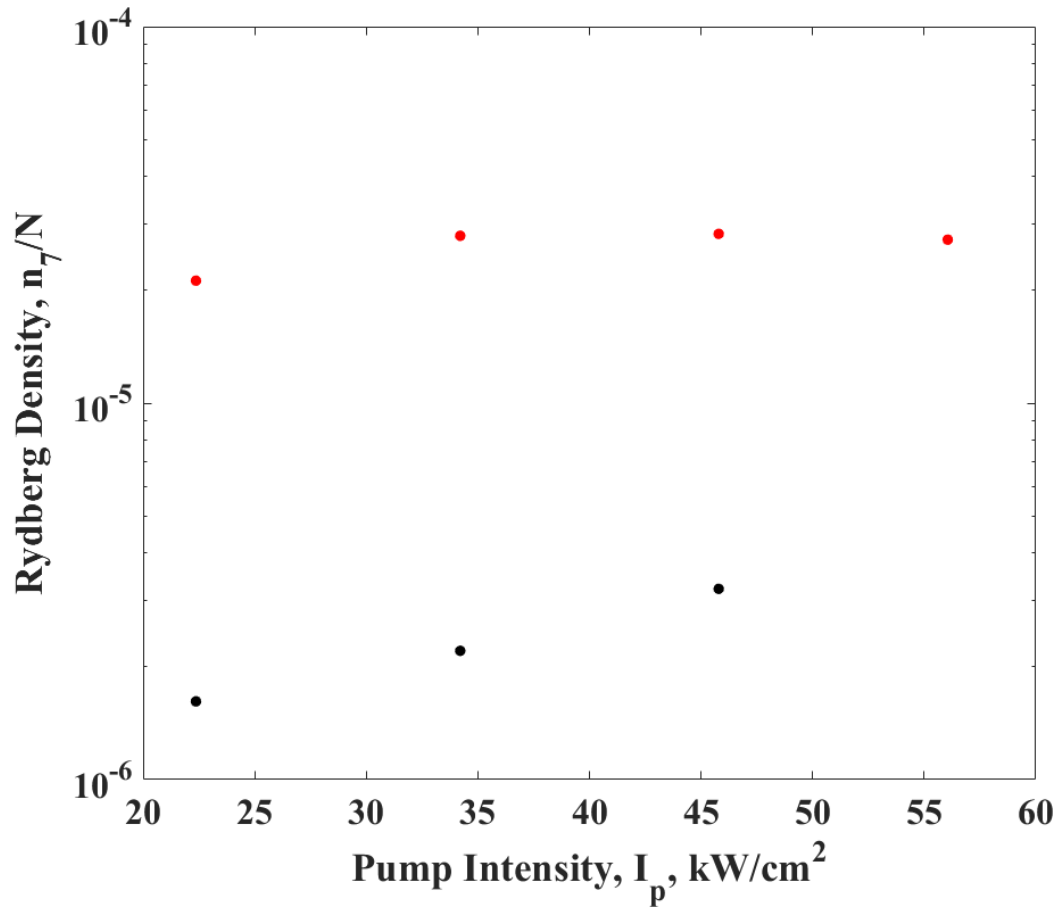
Figure 58. The observed (•) density in the Rydberg states as a function of pump intensity in a 6.7% methane buffer gas, in the presence of very weak lasing, $I_l = 100W/cm^2$. The black dots represent $N \sim 1 \times 10^{13} cm^{-3}$, **P**= 450 **Torr**, red is $N \sim 5 \times 10^{13} cm^{-3}$, **P**= 450 **Torr**.

4.4   Conclusion

Additional fluorescence data from a high power, transverse flow K laser is collected to further benchmark a recent multi-level kinetics DPAL model. With a single exception, the new data agrees with the model if a modification of quenching rates to account for different contamination is permitted. Weak scaling with pump intensity supports the wing absorption rate previously determined. The quenching rate of the higher states is increased by a factor of 160 when methane is added to the buffer gas, and the fluorescence is greatly decreased. Most of the data is adequately explained by the current mechanism, but an anomalous increase of intermediate density with pressure still remains unexplained. Free electrons are not considered, and their effects with pressure are unknown.

V. Effects of multi-level kinetics on beam quality and power efficiency in high power transverse flow Diode Pumped Alkali Lasers

The effects of higher energy levels on a high powered Diode Pumped Alkali Laser (DPAL) are demonstrated on a potasssiun-helium system with pump intensities larger than $I_p > 5\,kW/cm^2$ with moderate number densities $N = 0.1 - 10 \times 10^{13}\,cm^{-3}$. The additional heat loading due to the quenching of the higher states is minimal, $< 1\%$ of the spin orbit mixing heat load. This extra heat has a small effect on both Strehl and efficiency in the static system, but these can be recovered with flow velocities commensurate with transit times $< 0.15\,s$.

5.1 Introduction

The Diode Pumped Alkali Laser (DPAL) is a quasi-two level laser system that utilizes the lowest three energy states of the alkali vapor (14). The vapor is optically pumped along the D_2 transition, $n^2 S_{\frac{1}{2}} \to n^2 P_{\frac{3}{2}}$, then, in the presence of the buffer gas, is collisionally relaxed to the fine structure split $n^2 P_{\frac{1}{2}}$ state. From there the atom lases to the ground state in the near infrared (2). The DPAL is a relatively new gas laser system for high power applications (2; 17). The DPAL system has been scaled to $> 1\,kW$, with optical efficiency $> 50\%$, and promise for excellent beam quality (83). Ideal, quasi-two level performance is achieved when the cycle rate is limited only by diode pump intensity. A pulsed potassium laser has been demonstrated with the time scale for fine structure mixing of 70 ps (9).

Dramatic progress in power scaling of DPALs has been achieved with 1-2 kW systems developed in the potassium (18) and cesium (5) and recently a 30 kW Rb system (6). There is a controversy in the community over the influence of multi-level kinetics on the lasing media at these higher powers. These deleterious effects may

113

preclude from power scaling, and the additional heat load can adversely affect beam quality. Some modeling efforts indicate that the rate of photoionization is significant, on the order of $\frac{10^3}{sec}$ in situations with extremely high buffer gas pressures (10), and some effects have been shown experimentally (13). However, pulsed experiments have pumped 30 times higher than threshold with no significant loss in efficiency (69).

Three level kinetic models have been developed for the longitudinally pumped static DPAL (14; 15) and been bench marked by relevant experiments (24; 25). These models have been expanded upon to include additional kinetic levels, including ionization (70). The nine level model monitors the alkali density outside the lasing manifold and indicates that population lost is manageable in a relevant parameter space and should not hinder power scaling. Side fluorescence measurements from a high powered flowing DPAL show highly excited alkali densities much less than that in the lasing processes, which supports the assertion that multi-level kinetics will not seriously degrade laser performance (80).

The heat loading in a DPAL is primarily due to the spin orbit mixing. The quantum defects are very small, $95-99\%$ (3), but very rapid cycle rates, 1 ns (9) can cause temperatures of over 1,500 K in static 100 W lasers (84). Favorable temperatures can be recovered by introducing modest flows, and several models have been formulated for both longitudinal and transverse flow geometries (85; 86). Supersonic flows have been identified to further reduce laser temperatures and increase power scaling (87).

Modeling efforts of DPAL beam quality is rather limited. A wave optic simulations for static DPALS (88) and computational fluid dynamic models (89) are being developed. An analytic model was produced for high power DPAL, with a longitudinally pumped, transverse flow(90). For an 100 kW laser, modest flow rates are sufficient to control thermal gradients and achieve a Strehl ratio of > 0.9. All of these are constructed in the absence of multi-level kinetics. Due to the significantly larger

114

energy difference, even a small population in the higher atomic levels could seriously contribute to the heat loading of a DPAL. The energy released due to quenching of the intermediate atomic states is $19.6 - 251.8$ times that of the fine structure splitting of the lowest P state (3).

This study will extend the analytic model produced by Gavrielides et. al in Ref. (90) to include the intermediate states from the nine level kinetic model introduced in Ref. (70). This paper will begin with a summary of the nine level kinetic model and the 1-D flow model, then describing how the two are integrated. The effects of the additional mechanisms on performance, such as efficiency and Strehl, will be reported before ending with a discussion of when multi-level kinetics must be carefully considered.

5.2   Laser model

5.2.1   Three levels formulation.

Laser rate equations for a transverse flow DPAL were constructed using longitudinally averaged populations, also similar to Hager et. al in Ref. (14; 15). The complete model is presented in Ref. (90), the highlights are presented here. The populations in the two excited laser states ($n_{2,3}$) and the longitudinally averaged pump and laser intensities (Ω and Ψ) are calculated by solving a system of partial differential equations in the flow direction, η, and time, t. These equations in steady state are:

$$\frac{v}{w}\frac{\partial n_2}{\partial \eta} = -\mu_{21}\sigma_{21}(n_2 - n_1)\frac{\Psi}{h\nu_l} + k_{32}*(n_3 - 2*e^{-\theta}n_2) - n_2\Gamma_{21} \qquad (73)$$

$$\frac{v}{w}\frac{\partial n_3}{\partial \eta} = -\mu_{31}\sigma_{31}(n_3 - 2*n_1)\frac{\Omega}{h\nu_p} - k_{32}*(n_3 - 2*e^{-\theta}n_2) - n_3\Gamma_{31} \qquad (74)$$

115

$$\Omega = \frac{1}{\mu_{31}\sigma_{31}(n_3 - 2*n_1)l_g}$$
$$* [T_p I_{pin}(e^{\mu_{31}\sigma_{31}(n_3-2*n_1)l_g} - 1)(1 + R_p e^{\mu_{31}\sigma_{31}(n_3-2*n_1)l_g}) - 2\sigma_{31}n_3 * \frac{d\Omega_p}{4\pi}] \tag{75}$$

$$\Psi = -\frac{2I_{l,sat}\sigma_{21}n_2\frac{d\Omega_p}{4\pi}}{\mu_{21}\sigma_2 1(n_2 - n_1) - g_{th}} \tag{76}$$

In this, v is is the flow speed and w is the width of the flow channel. σ_i represents the optical cross section of transition i for temperature and pressure at the inlet (T_0, P_0); they are pressure and temperature dependent and are modulated for the exact position by $\mu_i = \sigma_i(T, P)/\sigma_i(T_0, P_0)$. $\theta = \Delta E/k_b T$ is the ratio of the P state energy splitting to the Boltzmann constant, k_b, times the temperature, T. k_{32} is the spin orbit mixing rate for the lowest P doublet. Γ_{ij} is the total decay rate from state i to state j; for the two excited states presented here, $\Gamma_{ij} = A_{ij} + k_{ij}^q$, the spontaneous emission rate (A_{ij}) and the first order quenching rate (k_{ij}^q). The quenching rate is small for this alkali-buffer gas pair and is negligible compared to A_{ij}. I_{pin} is the pump intensity incident on the laser cavity, T_p is the transmission loss of the pump beam at the windows, R_p is the reflectivity of the high reflective mirror, g_{th} is the threshold gain, and l_g is the gain length. $\frac{d\Omega_p}{4\pi}$ represents the solid angle subtended by the laser mirrors, acting to seed the laser from spontaneous emission. $I_{l,sat} = \frac{h\nu_l A_{21}}{\sigma_{21}}$ is the saturation intensity for the laser transition. Solving this system of equations also requires the assumption that the density in the higher energy levels is exceedingly small, that is to say that all of the density is in the lower three laser levels, $N = n_1 + n_2 + n_3$.

5.2.2 Nine level expansion.

A kinetic model describing the population of the higher energy states is presented in (70). A brief introduction will be presented here, but the entire derivation can be found there if interested. The model presented here is for potassium, but can be

116

easily converted to any of the other alkalies.

The energy levels associated with the different populations monitored are shown for potassium in Table 12. Hager's complete formulation of the three lasing states, n_1, n_2, and n_3 (14) serves as the foundation for this model as well. The population moved out of these states is considered small, so the population in those levels is unchanged. The intermediate states, $n^2 D(n_4)$, $(n+1)^2 P(n_5)$, and $(n+2)^2 S(n_6)$ are populated through photo-excitation into the far non-Lorenztian wings of the absorption feature and energy pooling. The primary mechanisms for population of the doubly

Table 12. Relevant potassium energy levels and term symbols

State	Term Symbol	Level, i	Energy, E_i (cm^{-1})	g_i
Ground State	$4^2S_{\frac{1}{2}}$	1	0	2
Upper Laser State	$4^2P_{\frac{3}{2}}$	2	12,985.186	2
Pumped State	$4^2P_{\frac{1}{2}}$	3	13,042.896	4
Intermediates	$4^2D_{\frac{3}{2},\frac{5}{2}}$	4	27,398.147	4
			27,397.077	6
	$5^2P_{\frac{1}{2},\frac{3}{2}}$	5	24,701.382	2
			24,720.139	4
	$6^2S_{\frac{1}{2}}$	6	27,450.710	2
Rydberg States	higher n	7	28,000-35,009	
Atomic Ion	$^1S_0$	8	35,009.814	1
Ionic Dimer	$X^2\Sigma_g$	9	28,880	2

excited, intermediate states are photo excitation into the far wings and energy pooling. Photo-excitation occurs simply when a pump or laser photon is absorbed by an atom in the nP states and is excited to either the nD or $(n+2)S$, $K(4P)+h\nu \rightarrow K(4D,6S)$. The rate of this excitation is unclear as incomplete potential surfaces for the upper states (76) make calculating the far wing absorption cross section difficult, and no experimental studies have been done on these higher states. Energy pooling occurs when two excited alkali collide resulting in the formation of a doubly excited atom and one in the ground state, $K(4P) + K(4P) \rightarrow K(4D,5P,6S) + K(4S)$. The rates

117

for these processes are well known in all alkali metals (42; 43; 44; 45).

Destruction of the intermediate states occurs through radiative processes, collisional de-excitation (quenching), and ionization. The quenching rates of the intermediates are unknown in the literature, but they are responsible for the most additional heat loading to alkali. An estimate of the quenching rate of potassium intermediate states in helium is given in Chapter III, and will be used here.

Ionization proceeds primarily through two processes, photo-ionization or Penning ionization. Penning ionization is the ionizing analogue of energy pooling (77). A collision with an excited alkali atom creates an ion and ground state atom. Both are included as the dominant ionization process depends on the parameter space of the laser design. The ion density is monitored as n^+.

The dominant recombination process passes through the ionic dimer, n_2^+, as the three body creation of the dimer is much faster than three body recombination (78). From there dissociative recombination creates a ground state alkali and a very excited alkali, above the intermediate states. All atomic levels above the intermediate states are combined into one model level, n_7, or the Rydberg states.

The single mechanism that adds the most additional heat loading is quenching of the intermediates states. The population in those states is given by:

$$n_4 = \frac{k_4^p * n_3^2 + \frac{\alpha^4 \sigma_L^4}{h\nu_p}(\Omega + \Psi)(n_2 + n_3)}{k_4^{PI} n_3 + \frac{\sigma_4^{ph}}{h\nu_p}(\Omega + \Psi) + \gamma_4} \tag{77}$$

$$n_6 = \frac{k_6^p * n_3^2 + \frac{\alpha^6 \sigma_L^6}{h\nu_p}(\Omega + \Psi)(n_2 + n_3)}{k_6^{PI} n_3 + \frac{\sigma_6^{ph}}{h\nu_p}(\Omega + \Psi) + \gamma_6} \tag{78}$$

$$n_5 = \frac{k_5^p * n_3^2 + \gamma_{45} n_4 + \gamma_{65} n_6}{k_6^{PI} n_3 + \frac{\sigma_6^{ph}}{h\nu_p}(\Omega + \Psi) + \gamma_6} \tag{79}$$

where Ω and Ψ are the intracavity averaged pump and laser intensity, respectively,

118

and $\nu_{p,l}$ are the pump and lasing frequencies. These states decay radiatively and collision with the rates $\gamma_i = A_i + k_{qi}M$, where A_i is the sum of the Einstein A-coefficients out of the given state, k_{qi} is the quenching rate, and M is the buffer gas density. $k^p_{4,5,6}$ represent the effective pooling rate out of $n_{2,3}$ to $n_{4,5,6}$ and $\sigma_L^{4,6}$ is the Lorenztian absorption cross section to $n_{4,6}$ by either a pump or lase photon and $\alpha_{4,6}$ serve as a modifier to correct for non-Lorenztian features in the far wings. The values for all of these rates for potassium are in Table 13.

<p align="center">**Table 13. Abbreviated kinetic model with associated rates**</p>

Parameter	Reaction	Recommended Value (80)	Units
A_{31}	$n_3 \rightarrow n_1 + h\nu$	3.80×10^7	s^{-1}
A_{21}	$n_2 \rightarrow n_1 + h\nu$	3.75×10^7	s^{-1}
A_4	$n_4 \rightarrow n_{i<4} + h\nu$	3.44×10^6	s^{-1}
A_5	$n_5 \rightarrow n_{i<5} + h\nu$	7.23×10^6	s^{-1}
A_6	$n_6 \rightarrow n_{i<6} + h\nu$	11.42×10^6	s^{-1}
A_7	$n_7 \rightarrow n_{i<7} + h\nu$	2.0×10^6	s^{-1}
A_{45}	$n_4 \rightarrow n_5 + h\nu$	3.43×10^6	s^{-1}
A_{65}	$n_6 \rightarrow n_5 + h\nu$	4.80×10^6	s^{-1}
σ_b^{D1}		4.87×10^{-15}	cm^2
σ_b^{D2}		3.39×10^{-15}	cm^2
k_{31}	$n_3 + M \rightarrow n_1 + M$	0	$cm^3/(atom-s)$
k_{21}	$n_2 + M \rightarrow n_1 + M$	0	$cm^3/(atom-s)$
k_{32}	$n_3 + M \rightarrow n_3 + M$	6.68×10^{-10}	$cm^3/(atom-s)$
k_{45}	$n_4 + M \rightarrow n_5 + M$	5.53×10^{-12}	$cm^3/(atom-s)$
k_{65}	$n_6 + M \rightarrow n_5 + M$	2.32×10^{-12}	$cm^3/(atom-s)$

k_4	$n_4+M \rightarrow n_{i<4}+M$	1.11×10^{-11}	$cm^3/(atom-s)$
k_5	$n_5+M \rightarrow n_{i<5}+M$	1.11×10^{-12}	$cm^3/(atom-s)$
k_6	$n_6+M \rightarrow n_{i<6}+M$	5.53×10^{-12}	$cm^3/(atom-s)$
k_4^p	$n^* + n^* \rightarrow n_4 + n_1$	7.31×10^{-11}	$cm^3/(atom-s)$
k_5^p	$n^* + n^* \rightarrow n_5 + n_1$	1.18×10^{-10}	$cm^3/(atom-s)$
k_6^p	$n^* + n^* \rightarrow n_6 + n_1$	1.21×10^{-11}	$cm^3/(atom-s)$
k_4^{PI}	$n_{2,3} + n_4 \rightarrow n_1 + n^+ + e^-$	5.95×10^{-8}	$cm^3/(atom-s)$
k_5^{PI}	$n_{2,3} + n_5 \rightarrow n_1 + n^+ + e^-$	8.07×10^{-8}	$cm^3/(atom-s)$
k_6^{PI}	$n_{2,3} + n_6 \rightarrow n_1 + n^+ + e^-$	1.11×10^{-7}	$cm^3/(atom-s)$
σ_L^4	$n_{2,3} + h\nu_{p,l} \rightarrow n_4$	3.62×10^{-14}	cm^2
σ_L^6	$n_{2,3} + h\nu_{p,l} \rightarrow n_6$	4.84×10^{-14}	cm^2
α^4		1.23×10^3	
α^6		0.62	
σ_4^{ph}	$n_4 + h\nu_{p,l} \rightarrow n^+ + e^-$	1.40×10^{-17}	cm^2
σ_5^{ph}	$n_5 + h\nu_{p,l} \rightarrow n^+ + e^-$	6.37×10^{-18}	cm^2
σ_6^{ph}	$n_6 + h\nu_{p,l} \rightarrow n^+ + e^-$	3.41×10^{-20}	cm^2

Figure 59 shows the heat load due to spin orbit mixing of the excited laser levels, in red, and the quenching of the intermediate levels, in blue, at 760 (solid) and 1,520 (dashed) Torr of buffer gas pressure, at $I_p = 10\,kW/cm^2$, and 760 Torr of

120

buffer gas at $I_p = 50 \, kW/cm^2$ (•). As alkali density increases the lasing threshold grows from $0.50 \, kW/cm^2$ at $N = 0.5 \times 10^{13} \, cm^{-3}$ to $10.54 \, kW/cm^2$ at $N = 10 \times 10^{13} \, cm^{-3}$, with 760 Torr of helium, which accounts for the slow increase of heat load from spin orbit mixing. The heating from the spin orbit mixing is much larger than the intermediate quenching for all number densities, for both helium pressures and both pump intensities. Adding additional helium increases the heat loading of both mechanisms at moderate number densities. Additional pump intensity increases both mechanisms at moderate helium pressures as well, but regresses to the previous value as no additional pump energy can be absorbed at higher alkali densities. Figure 59 also illustrates the intermediate density, n^{**} as compared to the total alkali density. It tends to grow at higher alkali densities, but is exceedingly low for all cases in the figure. The density in the intermediate states is less at higher pressures, but the additional helium causes an increase in the quenching rate, and the heat load increases.

The intermediate quenching is the largest additional heating added by the newer model, it may not be the largest additional heat loading currently being neglected. As discussed in Section 4.3, cell contaminants may play a large role on the quenching rate of excited states. This effect is not limited to the intermediate states, the pump and lasing states may too be rapidly quenched by contaminants. Due to the much larger population, the additional heat by the quenching of these lower states is quickly much larger than the heat loading of the intermediate quenching. This conclusion is shown in Figure 60. An exceedingly small quenching rate for n_2 and n_3 is required for the heat loading due to quenching of those two levels to be larger than that of all three intermediates; $k_{21,31} = 1.18 \times 10^{-15} \, cm^3/atom - s$ for a total alkali density of $N = 1.0 \times 10^{14} \, cm^{-3}$, 760 Torr of buffer gas, 10 kW/cm^2 pump intensity, or $k_{21,31} = 0.64 \times 10^{-15} \, cm^3/atom - s$ if the pressure is raised to 1,520 Torr. The
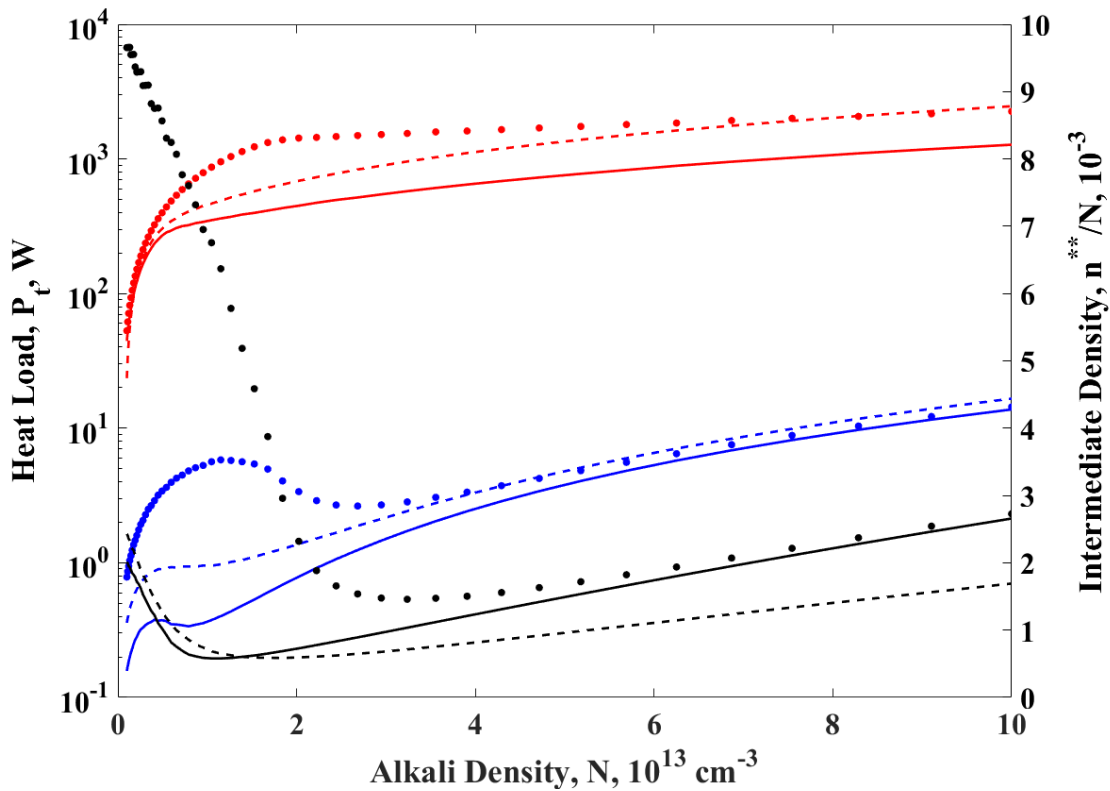
121

Figure 59. The heat loading due to the spin orbit mixing of the laser states (red) and the quenching of the intermediate states (blue) is shown as a function of number density at P=760 (solid) and $1,520$ (dashed) Torr, at $I_p = 10$ kW/cm^2, and 760 Torr of buffer gas at $I_p = 50\,kW/cm^2$ (•). The intermediate density fraction, n^{**}/N is also shown (black).

quenching rate of the $4\,^2P$ state with molecular nitrogen has been determined as $1.87 \times 10^{-10}\,cm^3/atom - s$ (91). Contamination of 6.3 ppm of nitrogen would be enough to drive additional heat loading due to quenching of laser levels higher than that of intermediate quenching. Additionally, the quenching rate of the $5\,^2P$ states in rubidium with helium is $4.92 \times 10^{-15}\,cm^{-3}$ (36). If this rate is consistent in potassium, the intermediate quenching would not be the next beam quality consideration.

There is additional heat loading caused by the creation of the dimer, as an energy difference of $\sim 6130\,cm^{-1}$ is associated with this reaction. However, due to the exceedingly small population of n^+ this heat load is negligible, under $1\,W$ is added for the conditions shown in Figure 60.

122
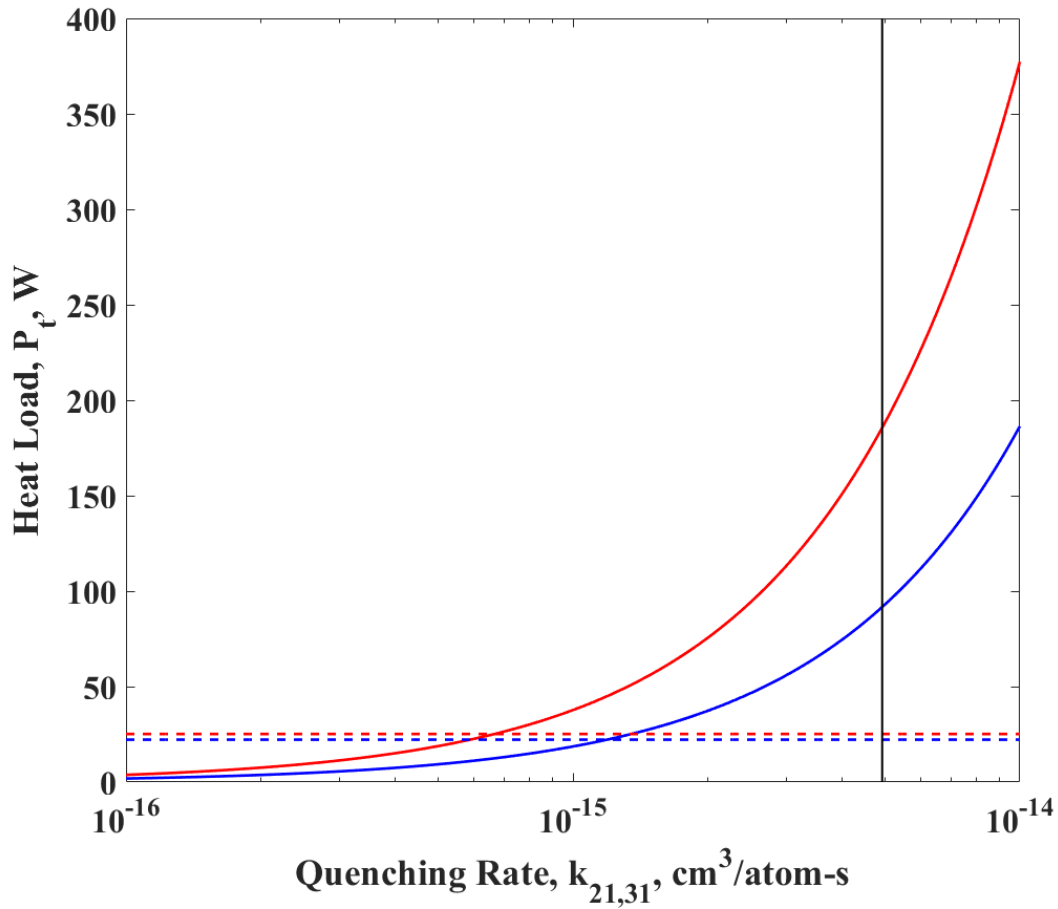
Figure 60. The heat loading due to quenching of n_2 and n_3 is shown as a function of quenching rate. The alkali density is $N = 1.0 \times 10^{14}\,cm^{-3}$, pump intensity of $I_p = 10\,kW/cm^2$, and buffer gas pressures of $P= 760$ (**blue**) and $1,520$ **Torr** (**red**). The dashed lines represent the heat loading due to intermediate quenching at the same conditions.

5.3   Analysis of results

5.3.1   Laser performance.

A simple design for a 100 kW K-He DPAL system is shown in Table 14. Diode bar technology is currently able to provide $I_p = 10 - 50\,kW/cm^2$ of intensity with spectrally narrowed bandwidths of $\Delta\nu_p = 10 - 100\,GHz$ (92; 93). At $I_p = 127.5\,kW/cm^2$ with a spot size of $5\,cm^2$, 73% optical-to-optical efficiency will produce over 100 kW of laser power. Aggressive diode narrowing, $\Delta\nu_p = 10\,GHz$ is selected to achieve a rea-

123

sonable spectral coupling at modest pressures. The alkali density, $N_0 = 4 \times 10^{13}\,cm^{-3}$, is chosen to balance threshold and required spin orbit recycle rate. The alkali density is limited by the melt pool temperature. For potassium, the alkali density associated with T= 460 K is $N = 8.33 \times 10^{14}\,cm^{-3}$ and N_0 represents 48% saturation of the gas flow. For a given buffer gas pressure, adding more alkali into the cell increases the power out, until bottle necking occurs when the buffer gas is not fast enough to cycle gain medium. At 760 Torr and 460 K, the spin orbit mixing rate is 298 times faster than the radiative rate. Additionally, the density in the cell must be such that the diode pump path is always optically thick, $A = \sigma_{13} N_0 l_g > 10$, and the corresponding DPAL gain is high $g_{21} > 3$. The optical cross section for absorption for the pump transition, σ_{13} depends on both buffer gas pressure and cell temperature. For potassium, at 760 Torr, the absorption cross section spectral width is 15.1 GHz. A higher pressure DPAL system will provide greater pressure broadening of the pump transition and lessen the demand for diode bar narrowing, however additional pressure decreases absorption, which can limit power out.

Table 14. Baseline laser parameters

Laser Parameter	Design Value
Inlet Gas Temperature, T_0	460 K
K Density, N_0	$4 \times 10^{13}\,cm^{-3}$
Helium Pressure, P_0	760 Torr
Pump Power, P_{in}	$137.5\,kW/cm^2$
Pump Area, A_p	$5\,cm^2$
Gain Length, l_g	14.7 cm
Output Mirror Reflectivity, R_s	0.20
Transverse Flow Velocity, v_0	$5\,m/s$
Diode spectral bandwidth	100 GHz

Figure 61 demonstrates laser performance as a function of input intensity, at different alkali densities and flow rates. The blue curves in the figure represent an

absorbance of $A = 130$, and the number density is doubled for the red curves, for $A = 260$. The dashed lines represent the laser intensity with an infinite flow rate, that is no thermal effects taken into account. The solid lines brings the flow speed to $v_0 = 1\,m/s$ and is the results of the model using only the three lasing states. The output intensity initially rises linearly, but levels off as no more pump can be absorbed. Doubling alkali density increases the magnitude of this plateau but the slope of the initial rise is unchanged. This slope is dependent on helium pressure. The open circles are calculated using full nine level multi-level kinetics model, with flow $v_0 = 1\,m/s$. A full description of the influence of multi level kinetics on the DPAL is discussed in a later section.
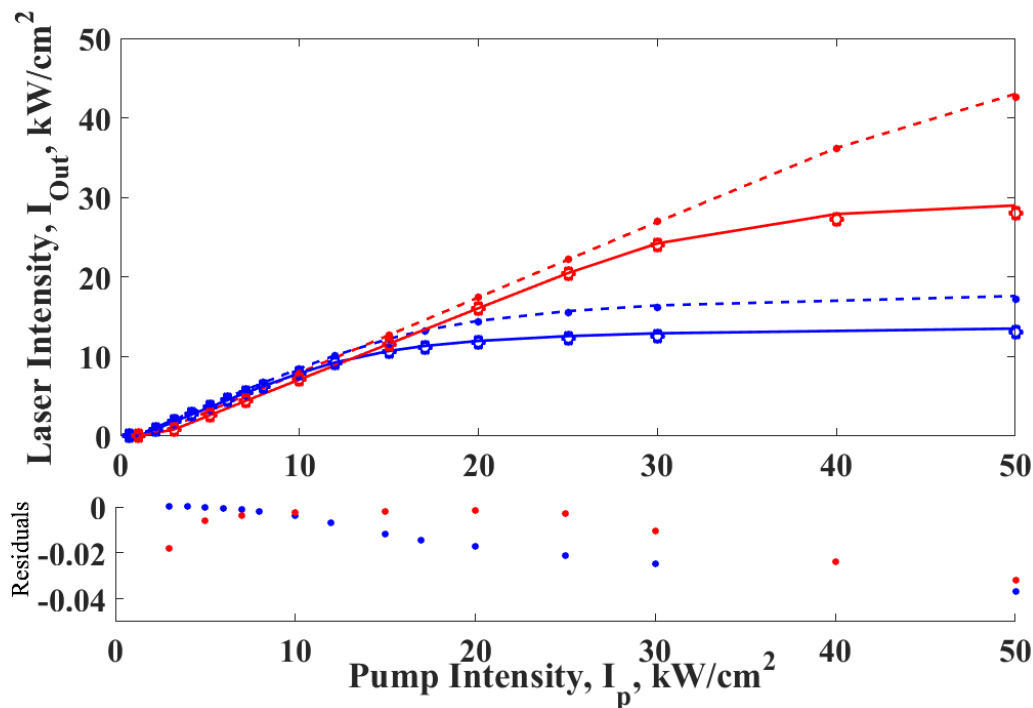
Figure 61. The laser intensity is shown here as a function of pump intensity at different densities to show laser performance at $N_0 = 2 \times 10^{13}\,cm^{-3}$ (red) and $N_0 = 1 \times 10^{13}\,cm^{-3}$ (blue), with an infinite flow velocity (dashed) and a finite speed, $v_0 = 1\,m/s$ (solid) using the three level model. The open circles ($\circ$) utilize the full nine level model for the finite speed and the filled circles ($\bullet$) are the infinite velocity. The helium pressure is set to 760 Torr. The lower plot represents the normalized difference of the values for the three level evaluation and the nine level kinetics at $v_0 = 1\,m/s$.

125

The effects of the heating on optical-to-optical efficiency, or output laser intensity compared to the diode pump intensity, $\epsilon = I_{out}/I_{pin}$, is shown in Fig. 62. It is possible for the slope efficiency to be near the quantum limit, $_{qe} = 0.99$, with optimal alkali density and helium pressures, even when considering the multi-level kinetics. The optical-to-optical efficiency is reduced by threshold. In Figure 62, the maximum efficiency is 85%, for a pump intensity of $10\,kW/cm^2$ with 760 Torr of buffer gas, occurs when the alkali density is consisted with $A \sim 150$, with no heat load. This is higher than the best experimentally observed efficiency of 81%, in a surrogate Ti:S pumped cesium system (82). Typical optical efficiencies of existing high powered systems are even less, $50 - 75\%$ (92).

At high alkali densities, the efficiency shown in Figure 62 trends downward. This is due to the higher number of photons needed to fully bleach through the entire cell, an effective increase in the threshold. The efficiency is poor at lower density because there are less atoms available to cycle and the output power is limited. As demonstrated in Ref. (90), as the flow rate is decreased, the efficiency is as well. Temperature gradients in the gain media force alkali out of the beam path and less diode power is absorbed.

Multi-level kinetics effect the efficiency here in two ways, decreasing the available density to lase and increasing the heat loading. As the alkali density is increased including the higher energy levels in the model actually increases the theoretical efficiency. The removal of population into the intermediate states moves the available alkali closer to the optimal density and the efficiency increases. The effects of added heat loading is observed as the flow velocity is lessened. As the flow is decreased from $10\,m/s$ to $1\,m/s$, the difference in the two model's expected efficiency increases by a factor of ~ 3. However, this effect is rather small, causing less than 1% decrease in efficiency with flows greater than $1\,m/s$.
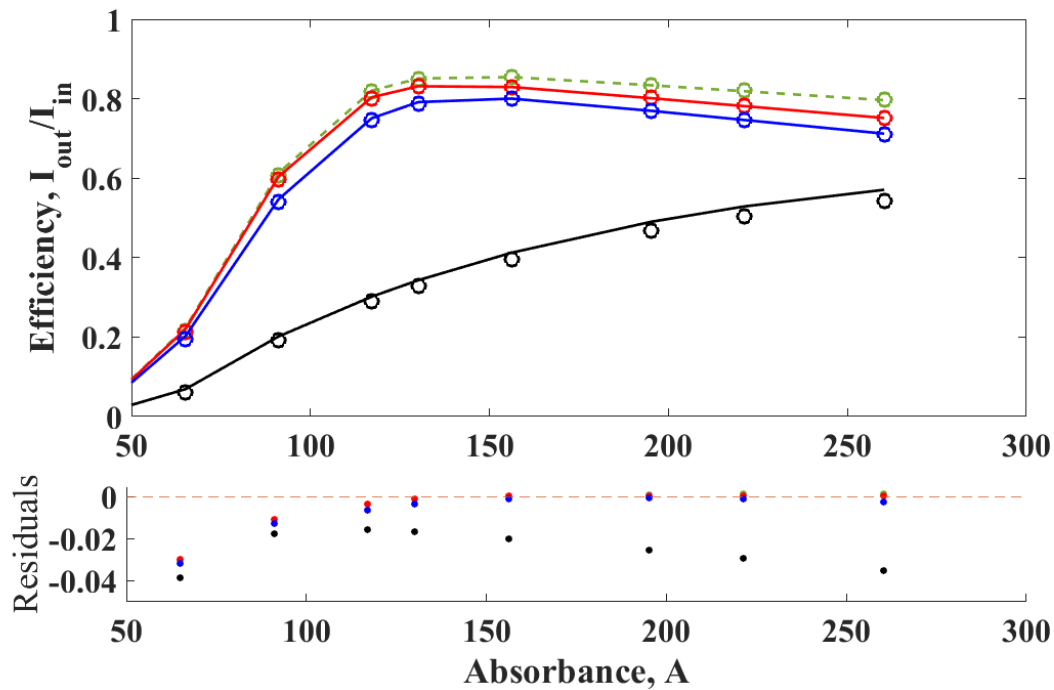
126

Figure 62. Laser efficiency is presented as a function of absorbance, $A = \sigma_{13} N_0 l_g$ at flow velocites of 0.05 m/s (black), 1 m/s (blue), 10 m/s (red) and infinite flow speed (green). The solid curve represents the calculations using only the three level laser model, while the open circles ($\circ$) include the nine level kinetics. The helium pressure is set to **760 Torr.** The lower plot represents the normalized difference of the values for the 3 level evaluation and the nine level kinetics.

In Figure 61, the effects of the additional levels is also inconsequential. When implemented, the multi-level model caused a maximum decrease of $< 3\%$ in output intensity and at moderate pump powers, $I_p > 5\,kW/cm^2$ the difference shrinks even smaller, $< 1.5\%$.

5.3.2 Beam quality considerations.

Aberrations in beam quality are caused by the phase variation in the flow direction. This phase variation is created by changes in the index of refraction due to heating. The fractional temperature rise in along the flow is shown in Figure 63 as a function of flow velocity at different helium pressures. Temperature rise is dramatic at near static conditions but when moderate flow velocities are introduced, the temperature

127

rise drops dramatically, less that 5% across a 14.7 cm gain length for flows faster than 5 m/s. Increasing buffer gas pressure in the cell lowers the temperature rise at all flow velocities, due to an increase of heat capacity.

Figure 63 also shows the effects of intermediate quenching on the temperature rise. Additional heat loading is added to the gaseous alkali from intermediate quenching causing a slight increase in the temperature rise, however, that increase is extremely small. Even with near 0 flow speeds, this increase is less than 5% for pressures P$\geq$ 760 Torr.
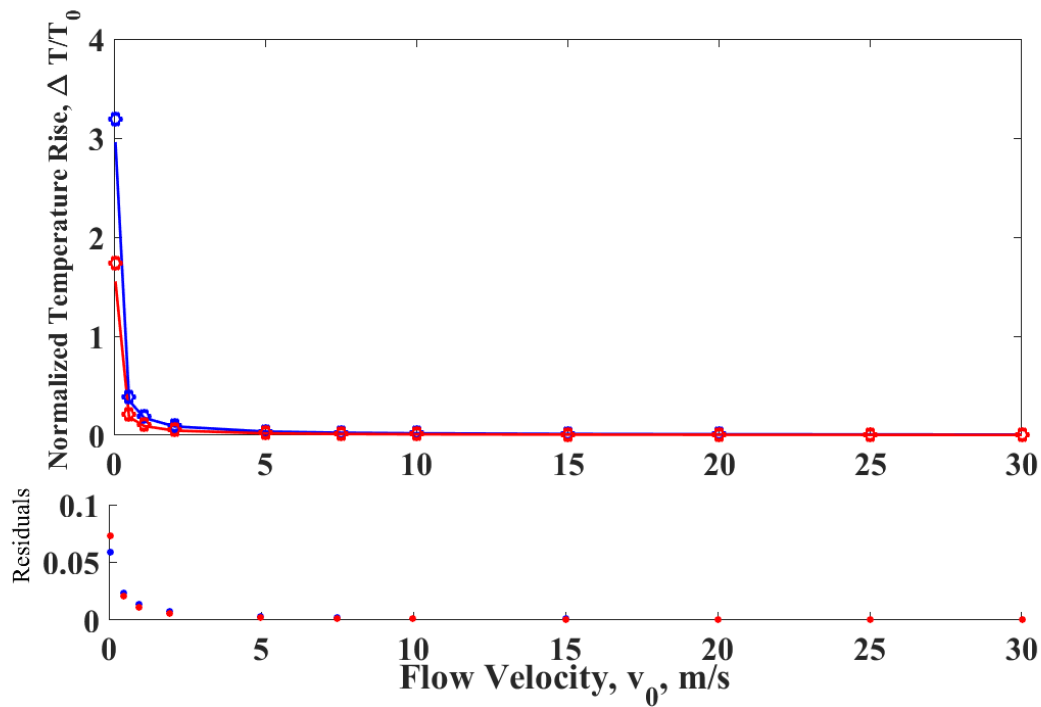
Figure 63. Normalized temperature rise in the flow direction is plotted as a function of flow velocity for helium pressures of P= 760 (blue) and 1,520 (red) Torr. The alkali density is set to $N_0 = 2 \times 10^{13}\, cm^{-3}$ and pump intensity to $I_p = 10\, kW/cm^2$. The solid curve represents the calculations using only the three level laser model, while the open circles (∘) include the nine level kinetics. The lower plot represents the normalize difference of the values for the three level evaluation and the nine level kinetics.

A scalar value to characterize beam quality is Strehl, S; it is the ratio of far field, on axis intensity relative to the diffraction limited performance (94). Laser weapon engagement models use system Strehl to assess many important performance metrics,

128

like effective range and required dwell time (83). The Strehl is calculated from the complex phase error across beam, but can be estimated using the integrated phase variation:

$$S = e^{-\sigma^2} \tag{80}$$

where $\sigma^2 = <\phi - \bar{\phi}>^2$ is the phase variance. This approximation is best for large Strehl, exhibting less than 10% error for Strehl > 0.3 (94).

Figure 64 demonstrates the effect of multi-level kinetics on the Strehl ratio at different flow velocities as a function of alkali density. In low flow velocity cases, increasing alkali density rapidly decreases the Strehl. This is caused by an increased number of alkali atoms cycling in the spin orbit mixing process and releasing more heat. If the flow is fast enough to disperse this heat load, then the effect is mitigated. The heat loading added by intermediates is still minimal. The difference in expected Strehl between the models is $< 0.5\%$ and this value decreases as alkali density grows.

The phase error is often expanded in a complete basis set, known as the Zerinke polynomials, in which each term represents a optical aberration (95). The often largest Zernike polynomials represent tilt and defocus. Tilt is the average slope across the wavefront and defocus is the apparent changing of the focal length, both due to inconsistencies in refractive index. Tilt and defocus can be removed with careful construction of the optic path, without the need for deformable mirrors. This corrected Strehl is plotted as a function of flow velocity in Fig. 65. As demonstrated, with even moderate flow velocities, $v_0 \geq 0.5\,m/s$ the corrected Strehl becomes excellent, $S_{cor} > 0.99$ for both the three and nine level implementation. While it appears that inclusion of the multi-level kinetics does increase the optical aberrations, most of them are in the first order and are easily removed, allowing recovery of the beam quality.

Figure 65 also demonstrates the effects of flow velocity on efficiency. Efficiency also grows with flow velocity, but not as fast as Strehl does. At flow speeds larger than
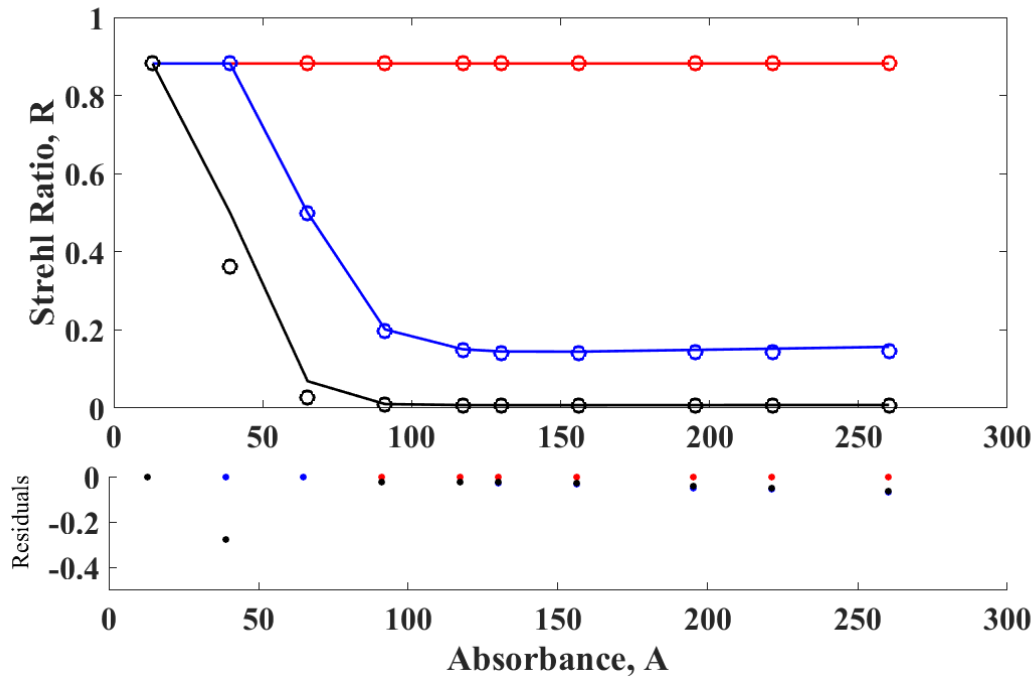
129

Figure 64. The full Strehl ratio is plotted as a function of absorbance at flow velocities of 10 m/s (red), 1 m/s (blue), and 0.05 m/s (black). The solid curve represents the calculations using only the three level laser model, while the open circles ($\circ$) include the nine level kinetics. The helium pressure is set to 760 Torr. The lower plot represents the normalized difference of the values for the three level evaluation and the nine level kinetics.

$v_0 \geq 1\,m/s$, the efficiency is over 92% of the infinite flow efficiency. For all speeds, the efficiency of the the three level model is closer to its theoretical maximum than that of the nine level, but as flow increases the that difference narrows drastically; at $v_0 = 20\,m/s$ the difference between the three level and nine level is less than 0.01%.

5.4 Conclusion

As the Diode Pumped Alkali Laser continues to scale to higher power effects of multi-level kinetics are a point of contention in the community. Removal of population from the lasing process and additional heat loading from other collisional process both can occur through these deletrious mechanisms. The beam quality implications of intermediate quenching in a longitudinal pumping and transverse flow DPAL have
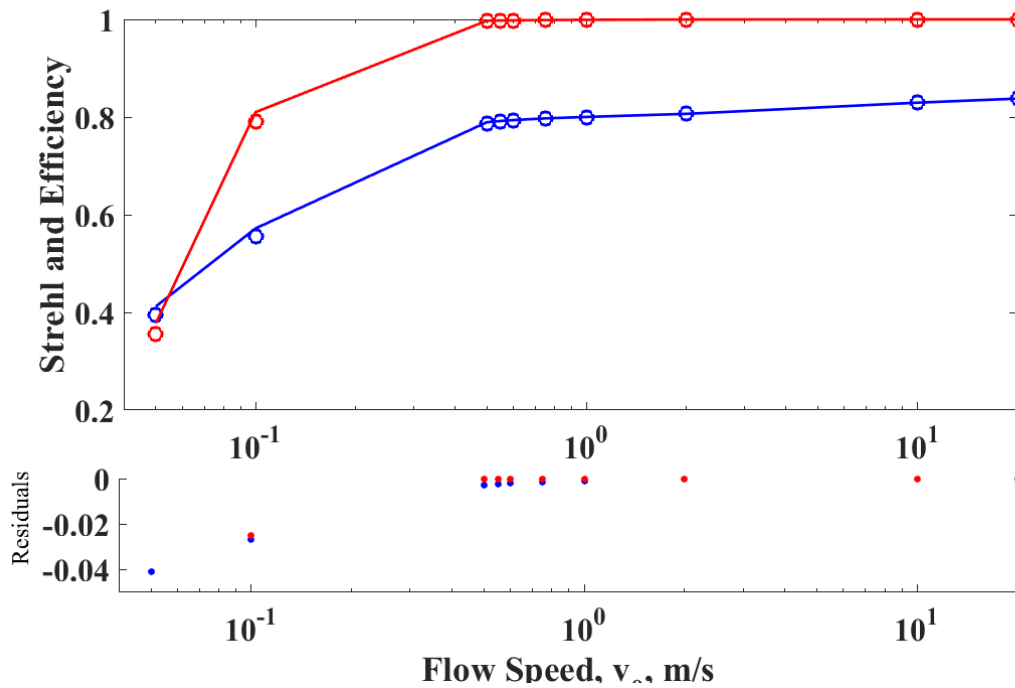
130

Figure 65. Corrected Strehl ratio (red) and laser efficiency (blue) is plotted versus flow speeds. The plot is made using a pump intensity of $10\,kW/cm^2$ and an absorbance of $A = 156$. The solid curve is calculated using just the three lasing levels, while the open circles (○) utilize the entire nine level model. The lower plot represents the normalized difference of the values for the three level evaluation and the nine level kinetics.

been analyzed, with little detriment to overall laser performance. Modest flow rates with residence times below 0.15 s is enough to recover any additional thermal lensing that intermediate quenching has introduced, coming within 5% of both the Strehl and laser efficiency when compared to the three level model. The decrease in Strehl, though, is almost all first order aberrations, which are easily removed with proper beam control; corrected Strehl is even closer in the two different models. The decrease in laser efficiency can easily be recovered by injecting more alkali at the inlet. The error in alkali density propagated by the exclusion of the nine levels is likely smaller than the accuracy in the number density diagnostic, so it can be optimized around just the same.

This model is limited in both the implementation of the flow and the multi-level

131

kinetics. The flow only considers one dimension and excludes turbulence, both of which will effect the final answer. Additionally, the only heat loading included in the mutli-level kinetics is the intermediate quenching. Quenching of the Rydberg states and collisional processes that create and destroy the ionic dimer will too add heat loading, however the exact rates of these processes and energy released in each event make the heat loading uncertain. The intermediate quenching is likely dominant mechanism, though, and will have the largest effect on laser performance.

VI. Conclusions

Prior to this research, no kinetic model reported populations in higher lying states as a method to characterize multi-level kinetics on laser performance. This allows for the characterization of the parameter space in which the higher order kinetics will have a noticeable effect on DPAL performance. Only one article considered a similar set of mechanisms, but that focused mainly on reactions between the alkali vapor and hydrocarbon buffer gas. Given the interest in power scaling in the DPAL community, a better understanding of the effects of multi-level kinetics is required and shown in this work.

Fluorescence spectroscopy has never been utilized to calculate the populations of the higher lying states in a DPAL system. This research has collected fluorescence spectrum of a flowing potassium DPAL for alkali densities of $N = 0.1 - 2.0 \times 10^{14}\,cm^{-3}$, pump intensities of $I_p = 20 - 60\,kW/cm^2$, and buffer gas pressures of $P = 250 - 1200$ Torr, with and without the addition of methane. The associated densities observed provide insight into the influence of the mechanisms to the production of the higher lying states.

The beam quality consequences of the density in the higher lying states was also numerically evaluated. An existing 1-D model for rubidium was updated to describe potassium and expanded to include the new multi-level mechanisms. This analysis has been done for the simple three level model, but while previous multi-level models attempt to determine the adverse effects on efficiency and output power, none have commented on the effects of additional heat loading.

6.1 Nine-level kinetic mode

Using the best rates available in the literature, a nine level expansion to Hager et. al's three level DPAL model (14; 15) indicates that the population outside the three laser levels is less than 6% of the total alkali density for all relevant alkali densities, buffer gas pressures, and pump intensities. This corresponds to a loss of less than 10% output intensity at pump intensities over 100 kW. This power can largely be recovered by simply increasing the temperature of the alkali bed to recuperate the small population lost to the higher levels. In fact, alkali diagnostics are often unable to determine the true alkali density in the gain length to this accuracy.

6.2 Fluorescence in a flowing DPAL

This work has observed densities of atomic potassium states as a function of alkali density, buffer gas pressure and pump intensity to offer a possible update to the kinetic rate package previously suggested. While the wing absorption rate is significantly larger in the far wings than a pure Lorenztian would predict, it likely does not dominate over energy pooling. The new rate package still indicates that the total alkali density loss to the higher states is not large enough to significantly degrade laser performance. Estimates of quenching rates for the intermediate states with helium are derived, however, it seems that these rates may not be the true value with pure helium as contaminants may play a larger role than previously expected. Cell construction plays a major role in laser performance and contaminants will greatly change the higher state population. An anomalous data point indicates growth with pressure that cannot be explained with current model may suggest that some other mechanism is crucial but missing from the current model.

6.3 Heat loading due to higher level quenching

This work has shown that the addition of the quenching of the intermediate states results in only a slight decrease for both Strehl ratio and laser efficiency, less than 5%, with modest flow velocities. Increasing flow velocities can recover much of this difference and the maximum Strehl and efficiency both approach the same value with infinite flow velocities. The added thermal aberrations can be corrected for without use of deformable mirrors; flow velocities with residence times near 0.1 s can achieve a theoretical Strehl of 1 with only corrections for tilt and defocus.

6.4 Proposed future work

There is a great deal of work needed to enhance the recommended rate package. The absorption line shapes of the higher $P - D$ and $P - S$, especially in the far wings, as a function of buffer gas pressure need to be determined, possibly through absorption spectroscopy. The quenching rates of the intermediate states with both helium and methane should also be directly measured; likely determined with time resolved fluorescence measurements. These are the most influential rates on the alkali population not part of the lasing process, and remain unexamined in the literature. Additionally, both the rates for the creation and destruction of the dimer have only been determined in cesium at gas temperatures much higher than naturally occurring in a DPAL.

Fluorescence spectroscopy is only able to evaluate density in atomic states, so it offers no information on the population of the ionic species, as no ionic transitions are observed in the current experiment. The current mechanism indicates that the ionic dimer makes up most of the highly excited population. An absorption spectroscopy experiments may be done to evaluate the ion population, both molecular and ionic, and find a true estimate of the total population in the higher excited states.

135

All of these observations have been with potassium. The different energy level locations of rubidium and cesium may lead to different kinetic pictures for the other alkali vapors. Fluorescence measurements should be collected for rubidium and cesium to benchmark this model for the other metals. However, this would require access to high powered CW devices. Alternatively, high powered pulsed devices can be used as a surrogate. The kinetics would need to be modified however to account for the pulsed dynamics. A brief explanation of this is demonstrated in Appendix A.

This model is noticeably missing mechanisms involving free electrons. A new thorough literature search is needed to understand the dominant mechanisms that involve free electrons. While the density is not overly large, excess laser energy can couple to the free electron population and possibly change the expected dynamics.

Appendix A. Pulsed application

The dynamics in a pulsed regime are different than in CW as the densities in excited states are decreased during the time between pulses. Collisional processes will have a more prominent role as they can still occur when the pump laser is off. Additionally, a pulsed system will never reach an equilibrium, exciting to the densities for Equations 64-72 when the pump is on, and decaying down between pulses. Instead we discuss the average densities:

$$\bar{n}_i = \lim_{T \to \infty} \int_0^T n_i dt \tag{81}$$

In this, we do not require the parameter T to actually tend toward infinity, instead only that it be a time scale on the order of the decay rate of the excited states. It can be shown that, for large values of κ, n_3 decays in $1/\gamma_3 \, sec$ between pulses, so we will assign that value to T. In general, the average values will be less than the steady state solutions derived above, and will depend on the ratio of pulse duration to the decay rate.

A similar approach to finding the steady state solutions is employed to find the averages, integrating the rate equations from Section 2.3 and setting them to zero. Assuming that the pump's intensity is such that the alkali medium is instantaneously bleached and lasing starts immediately with the pump, the average value for the intermediate states can be expressed as

$$\bar{n^{**}} = \frac{t_p}{T} \frac{K^p n_3^{02} f(N, t_p, \gamma_3...) + \frac{\sigma_w}{h\nu_p}(\Omega + \Psi)(n_2^0 + n_3^0) - \frac{\sigma^{ph}}{h\nu_p}(\Omega + \Psi)n_0^{**}}{K^{PI} n_3^0 g(N, t_p, \gamma_3, ...) + \gamma_{**}} \tag{82}$$

$\bar{n^{**}}$ is the average population in the intermediate states, n_3^0, n_2^0, and n_0^{**} is the steady state populations from equations 51, 50, and 57-59, respectively. The functions $f(N, t_p, \gamma_3...)$ and $g(N, t_p, \gamma_3...)$ are enhancement functions for the collisional mecha-

137

nisms. The exact form these functions take is difficult to predict as they rely heavily on the full time dependence of the levels involved with lasing. They are likely a function of alkali density, pulse duration, and decay rates, but may also include other kinetics rates, such as spin-orbit mixing.

Averages for the highest lying states are

$$\bar{n^+} = \frac{\bar{n^{**}}K^{PI}n_3^0 g(N, t_p, \gamma_3, ...) + \frac{t_p}{T}\frac{\sigma^{ph}}{h\nu_p}(\Omega + \Psi)n_0^{**}}{k_a M N} \tag{83}$$

$$\bar{n_2^+} = \frac{k_a M N \bar{n^+}}{k_{DR} n_{20}^+} \tag{84}$$

$$\bar{n_7} = \frac{k_{DR} n_{20}^+ (\bar{n_2^+} + \bar{n^+})}{\gamma_7} \tag{85}$$

where n_{20}^+ is the steady state solution of the ionic dimer when the laser is on, from Equation 61.

Appendix B. Spectral response calibration

Callibration of the Acton Spectrometer was completed using both a broad spectrum quartz halogen lamp, Oriel Instruments model number 5-123. A spectral irradiance is quoted by the manufacturer for a distance of 50 cm from the lamp. The equation is given as:

$$I = \lambda^{-5} * e^{42.98953 - \frac{4583.98173}{\lambda} + \frac{211819}{\lambda^2} - \frac{1.4232551E8}{\lambda^3} + \frac{3.847842E10}{\lambda^4} - \frac{3.8965903E12}{\lambda^5}},$$

where I is irradiance in $W/m^2 nm$, λ is the wavelength in nm, h is Plank's constant, and c is the speed of light. Taking this number and multiplying by the detector area and exposure time, and the the energy of a photon, $\frac{\lambda}{hc}$, gives the number of photons at each wavelength incident onto the detector. The detectivity of the spectrometer is found by dividing this photon density by the counts recorded by the spectrometer.

The detector spectral response for the spectrometers used in Chapters III and IV are shown in Figures 66-69. Each disjoint curve represents a single grating position on the spectrometer. Additionally, a different grating is used between 525 nm and 550 nm, so the larger jump is expected. To ensure minimal error, every collection was taken using identical grating positions. Between the two collections, the spectrometers were disassembled for transport, so it the differences between Figure 66 and 68 are understandable.

Figure 66. The detector response of the Acton spectrometer as a function of wavelength for the first data collection, March 2017.

Figure 67. The detector response of the McPherson 0.3m spectrometer as a function of wavelength for the first data collection, March 2017.
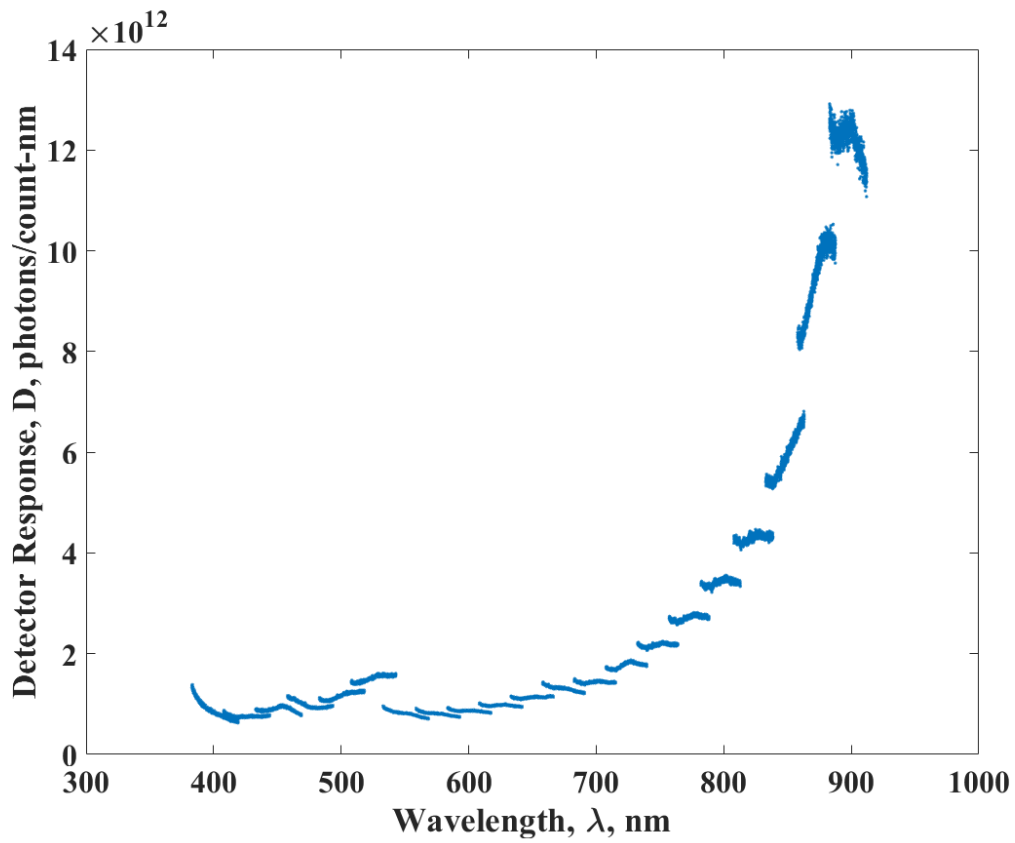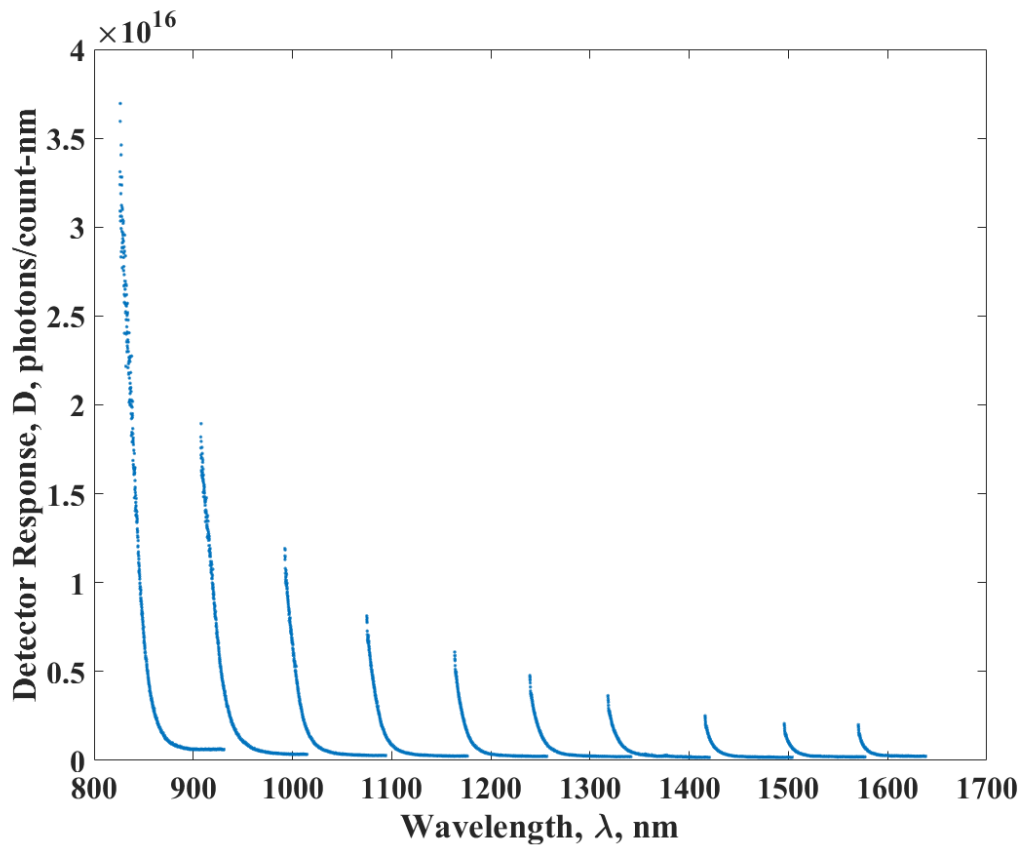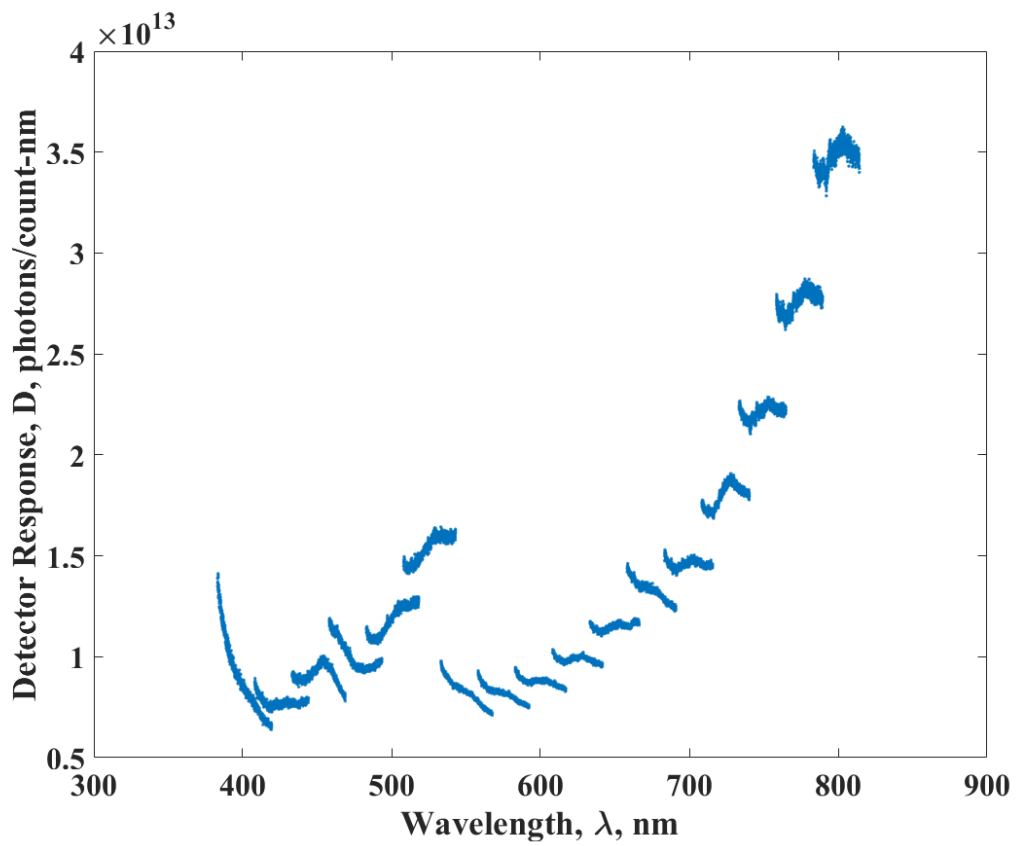
Figure 68. The detector response of the Acton spectrometer as a function of wavelength for the second data collection, June 2018.
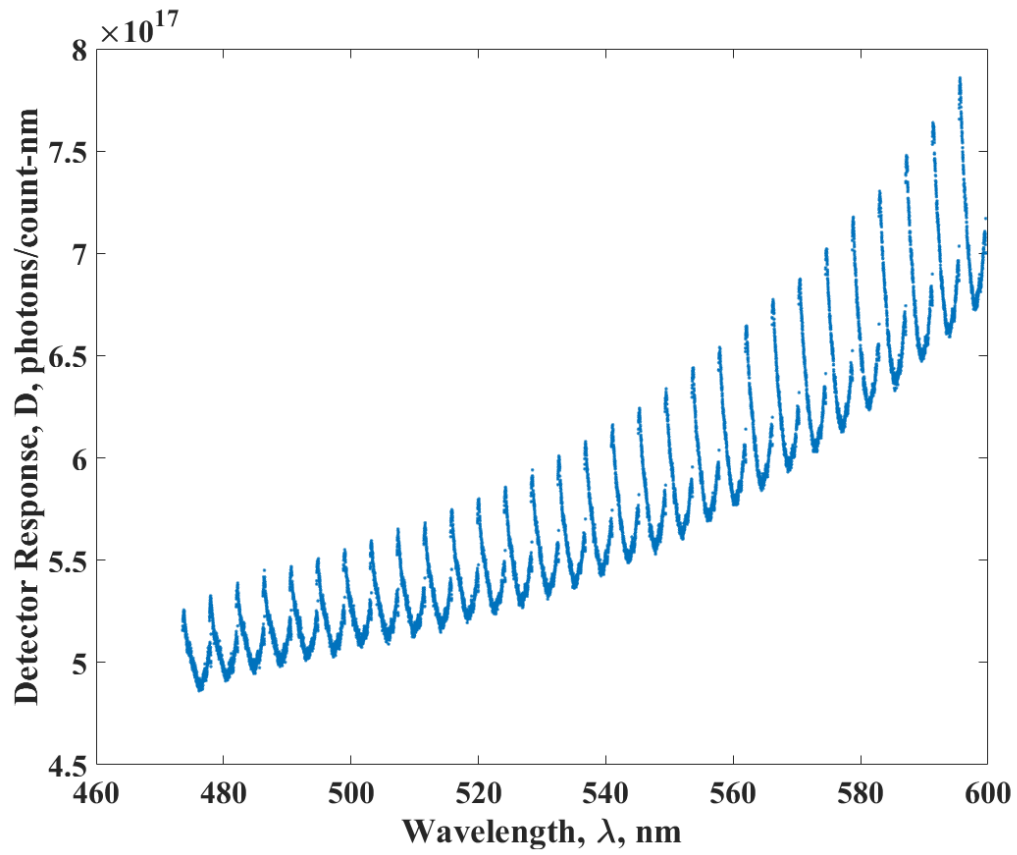
Figure 69. The detector response of the McPherson 1.3m spectrometer as a function of wavelength for the second data collection, June 2018.

143

Appendix C. Other spectral features

Spectral features were observed in the fluorescent data that do not correspond to any known atomic lines. First observed in the March 2017 experiment, these unknown features prompted additional study with better spectral resolution. Fluorescence collected in the $475 - 550$ nm range not corresponding to any alkali atomic lines first observed is shown in Figure 70. These emissions grow as buffer gas is added, especially when that gas includes methane. These spectral features may correspond to ro-vibrational bands of potassium hydride, specifically 8-0, 7-0, 6-0, 8-1, 7-1, 5-1 $(v' - v'')$ vibration transitions in the hydride (96).

Figure 70. Rise of spectral features not associated with atomic transitions, taken at $N = 1.87 \times 10^{14}\, cm^{-3}$ in a helium-methane buffer gas of 7.6% methane, at $P = 500$ Torr (black), 850 Torr (red), and 1,200 Torr (blue).

Similar, yet distinct, features were also observed in the second study, shown in Figure 71. The magnitude of the features grows as methane is added, from no methane (blue) to 6.7% with 450 Torr (red) to 6.7% with 850 Torr (black). The spectral assignment of these lines is incomplete at this time. Each spectral window seems to have an inherent structure unobserved in the pure helium sample, clouding the truth. Additionally, there are two new spectral features that were not present in the

144

previous study, near 573 nm and 599 nm. Additional study is required to identify these unknown features.

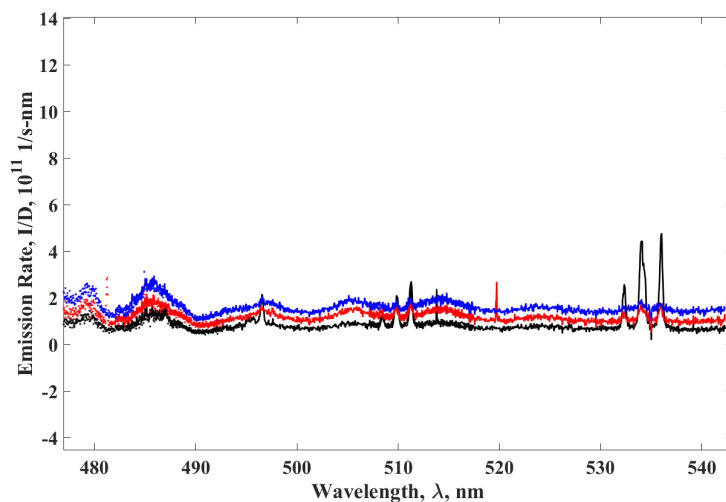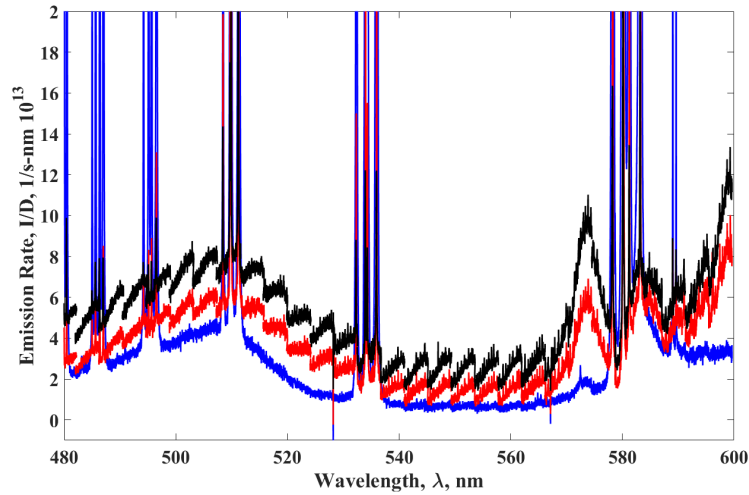**Figure 71. Rise of spectral features not associated with atomic transitions, taken at $N = 5.0 \times 10^{13}\, cm^{-3}$ in a helium-methane buffer gas of 7.6% methane at $P = 450$ Torr (red) and 850 Torr (black), and in a pure helium buffer gas with $P = 450$ Torr (blue).**

Appendix D. Additional experimental setup information

Some information, including cell dimensions and flow speeds, must be removed from the official dissertation document due to proprietary rights, and to allow for public release. Figure 72 shows the simulated irradiance profile across the pumped volume at the focus, and Figure 73 displays the size of the beam radius through the cell, from two different perspectives. The beam waist occurs about halfway through the gaseous alkali in the flow axis. In the lasing axis, it is as wide as the alkali flow until it is past the cell, where it diverges. Figure 73 also shows the length of the cavity and the location of lasing mirrors; the cavity is much longer than the alkali flow. The alkali flow has a volume of $2.54 \times 1.27 \times 1.22 \, cm$. Lastly, the flow speeds through the cell were a function of the buffer gas pressure and were measured between $0.98 - 4.72 \, m/s$ for pressures of $P = 250 - 1200$ Torr.
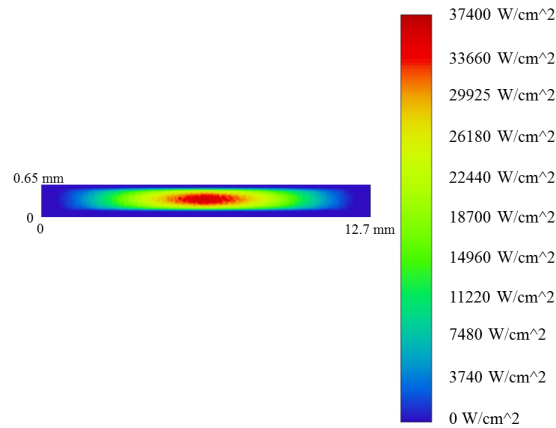
Figure 72. The irradiance profile at the focus of the pump beam. The peak irradiance is $37.4 \, kW/cm^2$**.**

[Cell geometry as seen along the pump axis.]

46.91 cm

1.22 cm
1.27 cm

Flow, z

1.27-5.08 cm

Lase, x

Pump, y

11.43 cm

1.27-5.08 cm
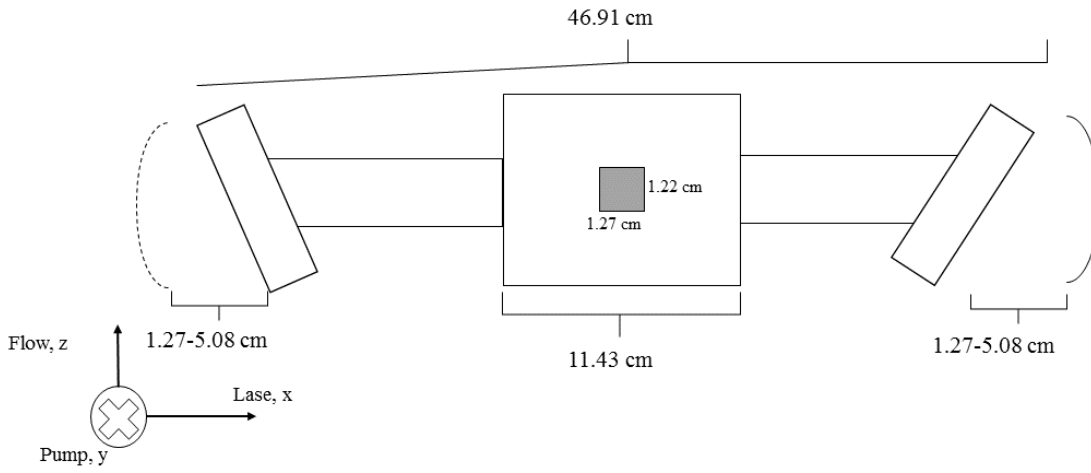
[As seen along the lasing axis.]

11.43 cm
1.22 cm
2.54 cm
8.89 cm

Flow, z

Pump, y

Lase, x
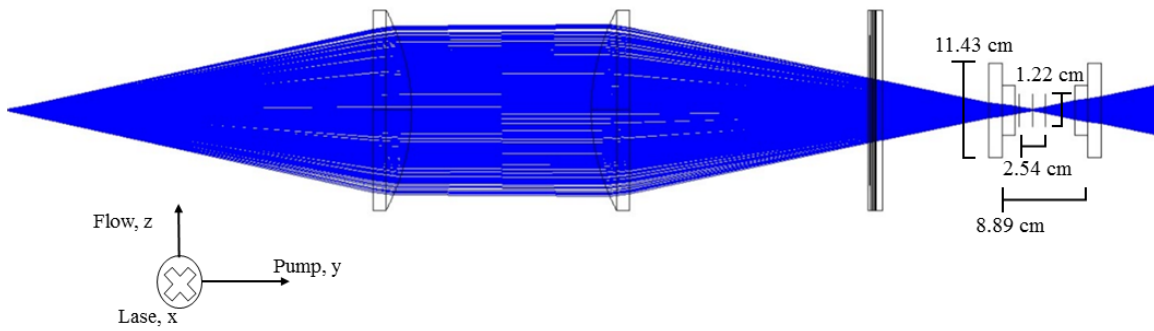
[As seen along the flow axis.]

1.25 cm
2.54 cm

Lase, x

Pump, y

Flow, z

147

Figure 73. Beam path
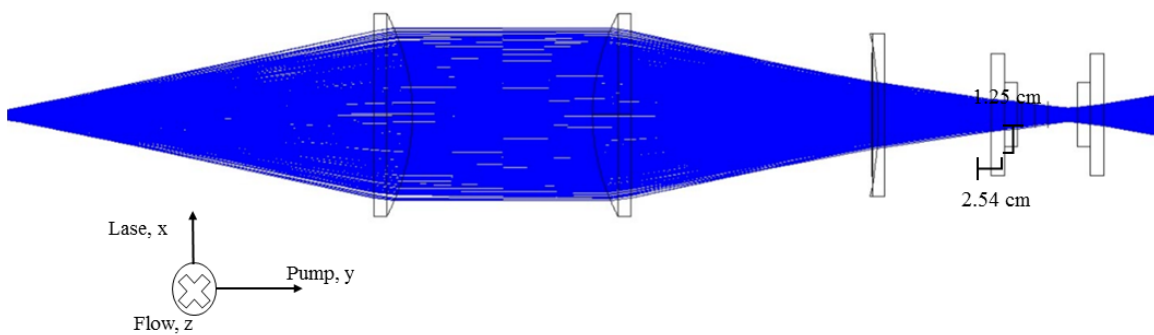
Bibliography

1. W. F. Krupke, R. J. Beach, V. K. Kanz, and S. A. Payne, "Resonance transition 795-nm rubidium laser," *Optics letters*, vol. 28, no. 23, pp. 2336–2338, 2003.

2. W. F. Krupke, "Diode-pumped alkali laser," Nov. 4 2003. US Patent 6,643,311.

3. A. Kramida, Yu. Ralchenko, J. Reader, and and NIST ASD Team. NIST Atomic Spectra Database (ver. 5.3), [Online]. Available: `http://physics.nist.gov/asd` [2017, October 12]. National Institute of Standards and Technology, Gaithersburg, MD., 2015.

4. G. A. Pitz, A. J. Sandoval, T. B. Tafoya, W. L. Klennert, and D. A. Hostutler, "Pressure broadening and shift of the rubidium D_1 transition and potassium D_2 transitions by various gases with comparison to other alkali rates," *Journal of Quantitative Spectroscopy and Radiative Transfer*, vol. 140, pp. 18–29, 2014.

5. A. V. Bogachev, S. G. Garanin, A. Dudov, V. Eroshenko, S. M. Kulikov, G. Mikaelian, V. A. Panarin, V. Pautov, A. Rus, and S. A. Sukharev, "Diode-pumped caesium vapour laser with closed-cycle laser-active medium circulation," *Quantum Electronics*, vol. 42, no. 2, pp. 95–98, 2012.

6. J. Syring Unclassified Statement of USN Director, Missile Defense A Senate Armed Services Committee Subcommittee on Strategic Forces, 4 2016.

7. B. Zhdanov, J. Sell, and R. Knize, "Multiple laser diode array pumped Cs laser with 48w output power," *Electronics Letters*, vol. 44, no. 9, pp. 582–583, 2008.

8. C. D. Fox and G. P. Perram, "Investigation of radial temperature gradients in diode pumped alkali lasers using tunable diode laser absorption spectroscopy," in *High Energy/Average Power Lasers and Intense Beam Applications VI; Atmospheric and Oceanic Propagation of Electromagnetic Waves VI*, vol. 8238, p. 823806, International Society for Optics and Photonics, 2012.

9. E. J. Hurd, J. C. Holtgrave, and G. P. Perram, "Intensity scaling of an optically pumped potassium laser," *Optics Communications*, vol. 357, pp. 63–66, 2015.

10. R. Knize, B. Zhdanov, and M. Shaffer, "Photoionization in alkali lasers," *Optics Express*, vol. 19, no. 8, pp. 7894–7902, 2011.

11. B. Q. Oliker, J. D. Haiducek, D. A. Hostutler, G. A. Pitz, W. Rudolph, and T. J. Madden, "Simulation of deleterious processes in a static-cell diode pumped alkali laser," in *Proc. SPIE*, vol. 8962, p. 89620B, 2014.

12. B. D. Barmashenko and S. Rosenwaks, "Detailed analysis of kinetic and fluid dynamic processes in diode-pumped alkali lasers," *Journal of the Optical Society of America B*, vol. 30, no. 5, pp. 1118–1126, 2013.

13. Z. Yang, L. Zuo, W. Hua, H. Wang, and X. Xu, "Experimental measurement of ionization degree in diode-pumped rubidium laser gain medium," *Optics letters*, vol. 39, no. 22, pp. 6501–6504, 2014.

14. G. D. Hager and G. P. Perram, "A three-level analytic model for alkali metal vapor lasers: part I. narrowband optical pumping," *Applied Physics B: Lasers and Optics*, vol. 101, no. 1, pp. 45–56, 2010.

15. G. D. Hager and G. P. Perram, "A three-level model for alkali metal vapor lasers. part II: broadband optical pumping," *Applied Physics B*, vol. 112, no. 4, pp. 507–520, 2013.

16. B. V. Zhdanov, M. D. Rotondaro, M. K. Shaffer, and R. J. Knize, "Time resolved efficiency degradation in potassium diode pumped alkali laser," tech. rep., United States Air Force Academy Air Force Academy United States, 2014.

17. G. P. Perram, M. A. Marciniak, M. Goda, *et al.*, "High energy laser weapons: technology overview," in *Proc. SPIE*, vol. 5414, pp. 1–25, 2004.

18. G. A. Pitz, D. M. Stalnaker, E. M. Guild, B. Q. Oliker, P. J. Moran, S. W. Townsend, and D. A. Hostutler, "Advancements in flowing diode pumped alkali lasers," in *High Energy/Average Power Lasers and Intense Beam Applications IX*, vol. 9729, p. 972902, International Society for Optics and Photonics, 2016.

19. A. H. Markosyan and M. J. Kushner, "Plasma formation in diode pumped alkali lasers sustained in Cs," *Journal of Applied Physics*, vol. 120, no. 19, p. 193105, 2016.

20. F. Gao, F. Chen, J. Xie, D. Li, J. Xie, G. Yang, C. Zheng, Y. Xu, and J. Guo, "Comparative study of diode-pumped hydrocarbon free Rb and K vapor lasers," *Optics & Laser Technology*, vol. 58, pp. 166–171, 2014.

21. N. Y. Babaevaa, O. Zatsarinnyb, K. Bartschatb, and M. J. Kushnera, "Mechanisms for plasma formation during high power pumping of xpal," in *Proc. of SPIE Vol*, vol. 8962, pp. 89620D–1, 2014.

22. A. Valance, "Adiabatic potential energies for NaK^+, $NaRb^+$, $NaCs^+$, KRb^+, KCs^+, $RbCs^+$, Na_2^+, K_2^+, Rb_2^+, and Cs_2^+ molecular ions," *The Journal of Chemical Physics*, vol. 69, no. 1, pp. 355–366, 1978.

23. M. Lapp and L. Harris, "Absorption cross sections of alkali-vapor molecules: I. Cs2 in the visible II. K2 in the red," *Journal of Quantitative Spectroscopy and Radiative Transfer*, vol. 6, no. 2, pp. 169–179, 1966.

24. W. Miller, C. Sulham, J. Holtgrave, and G. Perram, "Limitations of an optically pumped rubidium laser imposed by atom recycle rate," *Applied Physics B: Lasers and Optics*, vol. 103, no. 4, pp. 819–824, 2011.

149

25. N. D. Zameroski, G. D. Hager, W. Rudolph, and D. A. Hostutler, "Experimental and numerical modeling studies of a pulsed rubidium optically pumped alkali metal vapor laser," *Journal of the Optical Society of America B*, vol. 28, no. 5, pp. 1088–1099, 2011.

26. R. J. Beach, W. F. Krupke, V. K. Kanz, S. A. Payne, M. A. Dubinskii, and L. D. Merkle, "End-pumped continuous-wave alkali vapor lasers: experiment, model, and power scaling," *Journal of the Optical Society of America B*, vol. 21, no. 12, pp. 2151–2163, 2004.

27. I. Auslender, B. Barmashenko, S. Rosenwaks, B. Zhdanov, M. Rotondaro, and R. J. Knize, "Modeling of pulsed K diode pumped alkali laser: Analysis of the experimental results," *Optics express*, vol. 23, no. 16, pp. 20986–20996, 2015.

28. K. Waichman, B. D. Barmashenko, and S. Rosenwaks, "Laser power, cell temperature, and beam quality dependence on cell length of static Cs DPAL," *Journal of the Optical Society of America B*, vol. 34, no. 2, pp. 279–286, 2017.

29. W. Huang, R. Tan, Z. Li, and X. Lu, "Theoretical model and simulations for a cw exciplex pumped alkali laser," *Optics express*, vol. 23, no. 25, pp. 31698–31715, 2015.

30. W. S. Miller, C. A. Rice, G. D. Hager, M. D. Rotondaro, H. Berriche, and G. P. Perram, "High pressure line shapes of the Rb D_1 and D_2 lines for 4 He and 3 He collisions," *Journal of Quantitative Spectroscopy and Radiative Transfer*, vol. 184, pp. 118–134, 2016.

31. J. Ciuryƚ and L. Krause, "$4^2P_{1/2} \rightarrow 4^2P_{3/2}$ mixing in potassium induced in collisions with noble gas atoms," *Journal of Quantitative Spectroscopy and Radiative Transfer*, vol. 28, no. 6, pp. 457–461, 1982.

32. L. Krause, "Collisional excitation transfer between the $P2_{1/2}$ and $P2_{3/2}$ levels in alkali atoms," *Applied Optics*, vol. 5, no. 9, pp. 1375–1382, 1966.

33. P. Lijnse and J. Hornman, "Electronic-excitation transfer collisions in flamesv. cross sections for quenching and doublet-mixing of K (4^2P)-doublet by N_2, O_2, H_2 and H_2O," *Journal of Quantitative Spectroscopy and Radiative Transfer*, vol. 14, no. 10, pp. 1079–1083, 1974.

34. R. Anderson, T. Goddard, C. Parravano, and J. Warner, "Crossed molecular beam-tunable laser determination of velocity dependence of intramultiplet mixing: $K(4p\,^2P_{1/2}) + He \rightarrow$ K ($4p\,^2P_{3/2}$) + He," *The Journal of Chemical Physics*, vol. 64, no. 10, pp. 4037–4045, 1976.

35. R. E. Olson, "Fine structure transition cross sections for several alkali+ rare gas systems," *Chemical Physics Letters*, vol. 33, no. 2, pp. 250–253, 1975.

36. J. F. Sell, M. Gearba, B. Patterson, D. Byrne, G. Jemo, T. Lilly, R. Meeter, and R. Knize, "Collisional excitation transfer between Rb (5P) states in 50–3000 Torr of 4He," *Journal of Physics B: Atomic, Molecular and Optical Physics*, vol. 45, no. 5, p. 055202, 2012.

37. J. Dodd, E. Enemark, and A. Gallagher, "Quenching of cesium resonance radiation by helium," *The Journal of Chemical Physics*, vol. 50, no. 11, pp. 4838–4842, 1969.

38. G. A. Pitz, A. J. Sandoval, N. D. Zameroski, W. L. Klennert, and D. A. Hostutler, "Pressure broadening and shift of the potassium D_1 transition by the noble gases and N_2, H_2, HD, D_2, CH_4, C_2H_6, C_3H_8, and $n - C_4H_{10}$ with comparison to other alkali rates," *Journal of Quantitative Spectroscopy and Radiative Transfer*, vol. 113, no. 5, pp. 387–395, 2012.

39. G. A. Pitz and G. P. Perram, "Pressure broadening of the D1 and D2 lines in diode pumped alkali lasers," in *Proc. SPIE*, vol. 7005, pp. 700526–1, 2008.

40. A. Gallagher, "Rubidium and cesium excitation transfer in nearly adiabatic collisions with inert gases," *Physical Review*, vol. 172, no. 1, p. 88, 1968.

41. B. Eshel, J. A. Cardoza, D. E. Weeks, and G. P. Perram, "Role of adiabaticity in controlling alkali-metal fine-structure mixing induced by rare gases," *Physical Review A*, vol. 95, no. 4, p. 042708, 2017.

42. R. Namiotka, J. Huennekens, and M. Allegrini, "Energy-pooling collisions in potassium: $4P_J + 4P_J \rightarrow 4S + (nl = 5P, 6S, 4D)$," *Physical Review A*, vol. 56, no. 1, p. 514, 1997.

43. V. Horvatic, M. Movre, and C. Vadla, "The temperature dependence of the cross section for the energy pooling process Na (3P)+ Na (3P)→Na (4D)+ Na (3S)," *Journal of Physics B: Atomic, Molecular and Optical Physics*, vol. 32, no. 20, p. 4957, 1999.

44. S. Yi-Fan, D. Kang, M. Bao-Xia, W. Shu-Ying, and C. Xiu-Hua, "Energy-pooling collisions in rubidium: $5P_{3/2} + 5P_{3/2} \rightarrow 5S + (nl = 5D, 7S)$," *Chinese Physics Letters*, vol. 22, no. 11, p. 2805, 2005.

45. Z. Jabbour, R. Namiotka, J. Huennekens, M. Allegrini, S. Milošević, and F. De Tomasi, "Energy-pooling collisions in cesium: $6P_J + 6P_J \rightarrow 6S + (nl = 7P, 6D, 8S, 4F)$," *Physical Review A*, vol. 54, no. 2, p. 1372, 1996.

46. S. Gozzini, S. Abdullah, M. Allegrini, A. Cremoncini, and L. Moi, "Heteronuclear energy pooling collisions: the Na (3P)+ K (4P) reaction," *Optics communications*, vol. 63, no. 2, pp. 97–102, 1987.

47. C. Gabbanini, S. Gozzini, G. Squadrito, M. Allegrini, and L. Moi, "Energy-pooling collisions for K (4P)+ Rb (5P) and Na (3P)+ Rb (5P) heteronuclear systems," *Physical Review A*, vol. 39, no. 12, p. 6148, 1989.

48. G. D. Hager, G. E. Lott, A. J. Archibald, L. Blank, D. E. Weeks, and G. P. Perram, "High pressure line shapes for Cs D_1 and D_2 lines and empirically informed interaction potentials," *Journal of Quantitative Spectroscopy and Radiative Transfer*, vol. 147, pp. 261–273, 2014.

49. J. Pascale, "Use of l-dependent pseudopotentials in the study of alkali-metal-atomhe systems. the adiabatic molecular potentials," *Physical Review A*, vol. 28, no. 2, p. 632, 1983.

50. N. Allard, "Absorption profiles of the potassium 4s-4p and 4p-5s lines perturbed by helium," in *SF2A-2011: Proceedings of the Annual meeting of the French Society of Astronomy and Astrophysics*, pp. 439–442, 2011.

51. C. Zhu, J. F. Babb, and A. Dalgarno, "Theoretical study of sodium and potassium resonance lines pressure broadened by helium atoms," *Physical Review A*, vol. 73, no. 1, p. 012506, 2006.

52. C. Zhu, J. F. Babb, and A. Dalgarno, "Theoretical study of pressure broadening of lithium resonance lines by helium atoms," *Physical Review A*, vol. 71, no. 5, p. 052710, 2005.

53. G. A. Pitz, C. Sulham, E. Acosta, and G. P. Perram, "Two red photon absorption in alkalis producing infrared and blue beams," *AIAA Paper*, vol. 4876, 2010.

54. N. D. Haluska, *Cascade and two-photon lasing from two-photon excitation of cesium 62D*. PhD thesis, Air Force Institute of Technology, 2017.

55. A. Flusberg, R. Kachru, T. Mossberg, and S. Hartmann, "Foreign-gas-induced relaxation of Rydberg S and D states in atomic sodium," *Physical Review A*, vol. 19, no. 4, p. 1607, 1979.

56. M. Hugon, P. Fournier, and E. de Prunelé, "Quenching collisions of rubidium in the nS ($32 \geq n \geq 45$) Rydberg levels with helium," *Journal of Physics B: Atomic and Molecular Physics*, vol. 14, no. 21, p. 4041, 1981.

57. M. Hugon, B. Sayer, P. Fournier, and F. Gounand, "Collisional depopulation of rubidium rydberg levels by rare gases," *Journal of Physics B: Atomic and Molecular Physics*, vol. 15, no. 15, p. 2391, 1982.

58. R. C. Davila, G. P. Perram, and B. Eshel, "Time-resolved fine structure mixing of cesium induced by helium and argon," *Journal of Physics B: Atomic, Molecular and Optical Physics*, vol. 50, no. 22, p. 225204, 2017.

59. F. Gounand, J. Cuvellier, P. Fournier, and J. Berlande, "Collisional depopulation of a high-lying P state of potassium," *Journal de Physique Lettres*, vol. 37, no. 7-8, pp. 169–172, 1976.

60. J. Bellisio, P. Davidovits, and P. Kindlmann, "Quenching of rubidium resonance radiation by nitrogen and the noble gases," *The Journal of Chemical Physics*, vol. 48, no. 5, pp. 2376–2377, 1968.

61. K. Mogensen, J. Day, T. Ehrenreich, E. H. Pedersen, and K. Taulbjerg, "Coherent elliptic states in lithium," *Physical Review A*, vol. 51, no. 5, p. 4038, 1995.

62. O. Zatsarinny and S. Tayal, "Photoionization of potassium atoms from the ground and excited states," *Physical Review A*, vol. 81, no. 4, p. 043423, 2010.

63. I. I. Sobelman, *Atomic spectra and radiative transitions*, vol. 12. Springer Science & Business Media, 2012.

64. L. Barbier and M. Cheret, "Experimental study of penning and hornbeck-molnar ionisation of rubidium atoms excited in a high s or d level $(5d \geq nl \geq 11s)$," *Journal of Physics B: Atomic and Molecular Physics*, vol. 20, no. 6, p. 1229, 1987.

65. S. Wane and M. Aymar, "Excited-state photoionisation and radiative recombination for ions of the potassium isoelectronic sequence," *Journal of Physics B: Atomic and Molecular Physics*, vol. 20, no. 12, p. 2657, 1987.

66. G. Gousset, B. Sayer, and J. Berlande, "Electron-Cs+-ion recombination in the presence of neutral helium atoms," *Physical Review A*, vol. 16, no. 3, p. 1070, 1977.

67. Y. Momozaki and M. S. El-Genk, "Dissociative recombination coefficient for low temperature equilibrium cesium plasma," *Journal of applied physics*, vol. 92, no. 2, pp. 690–697, 2002.

68. E. Arimondo, F. Giammanco, A. Sasso, and M. Schisano, "Laser ionization and time-resolved ion collection in cesium vapor," *Optics communications*, vol. 55, no. 5, pp. 329–334, 1985.

69. C. V. Sulham, G. P. Perram, M. P. Wilkinson, and D. A. Hostutler, "A pulsed, optically-pumped rubidium laser at high pump intensity," *Optics Communications*, vol. 283, no. 21, pp. 4328–4332, 2010.

70. A. Wallerstein, G. Perram, and C. Rice, "Excitation of higher lying states in a potassium diode pumped alkali laser," 2018.

71. B. Gai, S. Hu, H. Li, Z. Shi, X. Cai, J. Guo, Y. Tan, W. Liu, Y. Jin, and F. Sang, "Multi-photon processes in alkali metal vapors," in *XX International Symposium*

153

on *High-Power Laser Systems and Applications 2014*, vol. 9255, p. 92552O, International Society for Optics and Photonics, 2015.

72. C. V. Sulham, G. A. Pitz, and G. P. Perram, "Blue and infrared stimulated emission from alkali vapors pumped through two-photon absorption," *Applied Physics B: Lasers and Optics*, vol. 101, no. 1, pp. 57–63, 2010.

73. T. Koenning, K. Alegria, Z. Wang, A. Segref, D. Stapleton, W. Faßbender, M. Flament, K. Rotter, A. Noeske, and J. Biesenbach, "Macro-channel cooled high power fiber coupled diode lasers exceeding 1.2 kw of output power," in *High-Power Diode Laser Technology and Applications IX*, vol. 7918, p. 79180E, International Society for Optics and Photonics, 2011.

74. L. Blank, D. E. Weeks, and G. S. Kedziora, "M+ Ng potential energy curves including spin-orbit coupling for M= K, Rb, Cs and Ng= He, Ne, Ar," *The Journal of chemical physics*, vol. 136, no. 12, p. 124315, 2012.

75. C. Alcock, V. Itkin, and M. Horrigan, "Vapour pressure equations for the metallic elements: 298–2500k," *Canadian Metallurgical Quarterly*, vol. 23, no. 3, pp. 309–313, 1984.

76. J. Pascale, "Use of l-dependent pseudopotentials in the study of alkali-metal-atom?e systems. the adiabatic molecular potentials," *Physical Review A*, vol. 28, no. 2, p. 632, 1983.

77. W. H. Miller, "Theory of penning ionization. i. atoms," *The Journal of Chemical Physics*, vol. 52, no. 7, pp. 3563–3572, 1970.

78. L. Harris, "Ionization and recombination in cesium-seeded plasmas near thermal equilibrium," *Journal of Applied Physics*, vol. 36, no. 5, pp. 1543–1553, 1965.

79. A. Wallerstein, G. Perram, and C. A. Rice, "Excitation of higher lying energy states in a rubidium DPAL," in *Solid State Lasers XXVII: Technology and Devices*, vol. 10511, p. 105112J, International Society for Optics and Photonics, 2018.

80. A. Wallerstein, G. Perram, C. Rice, G. Pitz, E. Guild, and D. Stalnaker, "Kinetics of higher lying states in a high power, transverse flow diode pumped potassium vapor laser," 2018.

81. G. A. Pitz, C. D. Fox, and G. P. Perram, "Transfer between the cesium 6 2 p 1/2 and 6 2 p 3/2 levels induced by collisions with h 2, hd, d 2, ch 4, c 2 h 6, cf 4, and c 2 f 6," *Physical Review A*, vol. 84, no. 3, p. 032708, 2011.

82. B. Zhdanov, T. Ehrenreich, and R. Knize, "Highly efficient optically pumped cesium vapor laser," *Optics Communications*, vol. 260, no. 2, pp. 696–698, 2006.

154

83. G. P. Perram, M. A. Marciniak, and M. Goda, "High-energy laser weapons: technology overview," in *Laser Technologies for Defense and Security*, vol. 5414, pp. 1–26, International Society for Optics and Photonics, 2004.

84. W. Zhang, Y. Wang, H. Cai, L. Xue, J. Han, H. Wang, and Z. Liao, "Theoretical study on temperature features of a sealed cesium vapor cell pumped by laser diodes," *Applied optics*, vol. 53, no. 19, pp. 4180–4186, 2014.

85. Z. Yang, H. Wang, Q. Lu, L. Liu, Y. Li, W. Hua, X. Xu, and J. Chen, "Theoretical model and novel numerical approach of a broadband optically pumped three-level alkali vapour laser," *Journal of Physics B: Atomic, Molecular and Optical Physics*, vol. 44, no. 8, p. 085401, 2011.

86. B. Shen, B. Pan, J. Jiao, and C. Xia, "Kinetic and fluid dynamic modeling, numerical approaches of flowing-gas diode-pumped alkali vapor amplifiers," *Optics Express*, vol. 23, no. 15, pp. 19500–19511, 2015.

87. B. Barmashenko and S. Rosenwaks, "Feasibility of supersonic diode pumped alkali lasers: model calculations," *Applied Physics Letters*, vol. 102, no. 14, p. 141108, 2013.

88. M. Endo, R. Nagaoka, H. Nagaoka, T. Nagai, and F. Wani, "Wave optics simulation of diode pumped alkali laser (DPAL)," in *High Energy/Average Power Lasers and Intense Beam Applications IX*, vol. 9729, p. 972907, International Society for Optics and Photonics, 2016.

89. K. Waichman, B. D. Barmashenko, and S. Rosenwaks, "Computational fluid dynamics modeling of subsonic flowing-gas diode-pumped alkali lasers: comparison with semi-analytical model calculations and with experimental results," *JOSA B*, vol. 31, no. 11, pp. 2628–2637, 2014.

90. A. Gavrielides, L. Schlie, R. D. Loper, M. R. Hawks, and G. P. Perram, "Analytic treatment of beam quality and power efficiency in high power transverse flow diode pumped alkali laser," *JOSA B*, 2018.

91. P. Lijnse and J. Hornman, "Electronic-excitation transfer collisions in flames—V. cross sections for quenching and doublet-mixing of K($4\,^2P$)-doublet by N_2, O_2, H_2 and H_2O," *Journal of Quantitative Spectroscopy and Radiative Transfer*, vol. 14, no. 10, pp. 1079–1083, 1974.

92. W. F. Krupke, "Diode pumped alkali lasers (dpals)—a review (rev1)," *Progress in Quantum Electronics*, vol. 36, no. 1, pp. 4–28, 2012.

93. A. Gourevitch, G. Venus, V. Smirnov, D. Hostutler, and L. Glebov, "Continuous wave, 30 W laser-diode bar with 10 GHz linewidth for Rb laser pumping," *Optics letters*, vol. 33, no. 7, pp. 702–704, 2008.

155

94. V. N. Mahajan, "Strehl ratio for primary aberrations in terms of their aberration variance," *JOSA*, vol. 73, no. 6, pp. 860–861, 1983.

95. V. N. Mahajan, "Strehl ratio for primary aberrations: some analytical results for circular and annular pupils," *JOSA*, vol. 72, no. 9, pp. 1258–1266, 1982.

96. A. Pardo, J. Poyato, M. Guijarro, and J. Fernandez-Alonso, "Laser-induced fluorescence and inelastic collisions of kh molecule," *Journal of Molecular Spectroscopy*, vol. 97, no. 2, pp. 248–252, 1983.

REPORT DOCUMENTATION PAGE

Form Approved
OMB No. 0704–0188

The public reporting burden for this collection of information is estimated to average 1 hour per response, including the time for reviewing instructions, searching existing data sources, gathering and maintaining the data needed, and completing and reviewing the collection of information. Send comments regarding this burden estimate or any other aspect of this collection of information, including suggestions for reducing this burden to Department of Defense, Washington Headquarters Services, Directorate for Information Operations and Reports (0704–0188), 1215 Jefferson Davis Highway, Suite 1204, Arlington, VA 22202–4302. Respondents should be aware that notwithstanding any other provision of law, no person shall be subject to any penalty for failing to comply with a collection of information if it does not display a currently valid OMB control number. **PLEASE DO NOT RETURN YOUR FORM TO THE ABOVE ADDRESS.**

1. REPORT DATE *(DD–MM–YYYY)*	2. REPORT TYPE	3. DATES COVERED *(From — To)*
10–09–2018	Doctoral Dissertation	Sept 2014 — Sept 2018

4. TITLE AND SUBTITLE

Kinetics of higher lying potassium states after excitation of the D_2 transition in the Presence of Helium

5a. CONTRACT NUMBER

5b. GRANT NUMBER

5c. PROGRAM ELEMENT NUMBER

6. AUTHOR(S)

Wallerstein, Austin J Capt, USAF

5d. PROJECT NUMBER

5e. TASK NUMBER

5f. WORK UNIT NUMBER

7. PERFORMING ORGANIZATION NAME(S) AND ADDRESS(ES)

Air Force Institute of Technology
Graduate School of Engineering and Management (AFIT/EN)
2950 Hobson Way
WPAFB OH 45433-7765

8. PERFORMING ORGANIZATION REPORT NUMBER

AFIT-ENP-DS-18-D-009

9. SPONSORING / MONITORING AGENCY NAME(S) AND ADDRESS(ES)

High Energy Laser Joint Technology Office
901 University Blvd. SE, Suite 100
Albuquerque, NM 87106
505-248-8208, harro.ackermann@jto.hpc.mil
ATTN: Dr. Harro Ackermann

10. SPONSOR/MONITOR'S ACRONYM(S)

HEL-JTO

11. SPONSOR/MONITOR'S REPORT NUMBER(S)

12. DISTRIBUTION / AVAILABILITY STATEMENT

DISTRIBUTION STATEMENT A:
APPROVED FOR PUBLIC RELEASE; DISTRIBUTION UNLIMITED.

13. SUPPLEMENTARY NOTES

This material is declared a work of the U.S. Government and is not subject to copyright protection in the United States.

14. ABSTRACT

A kinetic model for the performance of a potassium Diode Pumped Alkali Laser (DPAL), including the role of higher lying states is developed to assess the impact on device efficiency and performance. A rate package for a nine level kinetic model including recommended rate parameters is solved under steady-state conditions. The fraction of the population removed from the basic three levels associated with the standard model is less than 10% for all reasonable laser conditions, including pump intensities up to 100 kW/cm^2 and K densities as high as $10^{16}\,cm^{-3}$. To benchmark this new model, fluorescence emitted by a high power, transverse flow potassium DPAL was collected to characterize the highly excited state population. The population in these states was found to be less than 5% for all cases. The additional heat loading due to the quenching of the higher states is minimal, $< 1\%$ of the spin-orbit mixing heat load. This extra heat has a small effect on both Strehl and efficiency in the static system, but these can be recovered with flow velocities commensurate with transit times across the pump volume $< 0.1\,s$.

15. SUBJECT TERMS

Diode Pumped Alkali Laser, Alkali, Ionization, Potassium

16. SECURITY CLASSIFICATION OF:

a. REPORT	b. ABSTRACT	c. THIS PAGE
U	U	U

17. LIMITATION OF ABSTRACT

U

18. NUMBER OF PAGES

156

19a. NAME OF RESPONSIBLE PERSON

Dr. Glen P. Perram, AFIT/ENP

19b. TELEPHONE NUMBER *(include area code)*

(937) 255-3636, x4504; glen.perram@afit.edu

Standard Form 298 (Rev. 8–98)
Prescribed by ANSI Std. Z39.18

www.manaraa.com